Development of Field Scenario Ray Tracing Software for the Analysis of Bifacial Photovoltaic Solar Panel Performance

Chu Tu Li

Thesis submitted to the
Faculty of Graduate and Postdoctoral Studies
in partial fulfillment of the requirements for the
M.A.Sc. Degree in Electrical and Computer Engineering

August 2016

School of Electrical Engineering and Computer Science

University of Ottawa

Abstract

This thesis is based on a project "Bifacial Photovoltaic Energy Production Analysis" to build a detailed simulation model system accurately simulate bifacial panel performance under real field radiation conditions and deployment configuration, and to predict its corresponding energy yield. To the author's up-to-date knowledge, the model system is unprecedented among same type simulation software in complexity, details in consideration, ranges of deployment and parameters.

The model system can also be used as a platform for more components and variables to be added on, such as adding on more rows of panel arrays to simulate bifacial solar farm scenario; and adding spectral information for more accurate analysis.

The system components' sub-models were carefully chosen based on a broad literature review in related aspects; especially in sky diffuse radiance, ground reflection, and bifacial solar cells.

Built in MATLAB© based on mathematical expressions from above said models, the system consists of 5 bifacial panels and their racking as shading objects and the central panel performance is under investigation and has taken consideration of all possible panel azimuth and elevation combinations.

Model simplification and resolution are carefully considered so to achieve a good balance in complexity, computation load and output accuracy. Output reliability is confirmed with other people's work. Furthermore, the model has been fully checked and peer tested.

Outputs under different parameter settings are analysed and discussed. Conclusions and recommended future work are provided at the end of the thesis.

Statement of originality

Except where stated otherwise, the results presented in this thesis were obtained by the author during the period of his MA.Sc. research under the supervision of Dr. Henry Schriemer and Dr. Karin Hinzer, which are to the best of his knowledge original.

The IQE curve used to calculate photonic power to short circuit current conversion ratio is provided by Ahmed Gabr, SUNLAB, University of Ottawa.

The simulation running and data processing of model quality checks in section 5.1 was partly executed by Annie Russell, SUNLAB, University of Ottawa.

The following contribution(s) cover results presented in this thesis:

1. H. Schriemer, Robert Chutu Li, and J. E. Haysom, D. Lekx , Rui Li, M. Mahmoudysepehr, and D. Henes, "Accurate Modeling of the Solar Resource for Bifacial Photovoltaics", Photonics North 2016, Quebec City, Canada, 24-26 May 2016.

In addition, the following contributions are not directly related to the topic of this thesis, but are results of research during the program:

PRESENTATIONS

1. Robert Chutu Li*, Mark Yandt, Matthew Wilkins, Karin Hinzer, Joan Haysom, Henry Schriemer. Design of a 35% high concentrating photovoltaic system that operates in both direct and diffuse illumination. Photonics North 2015, Ottawa, Canada, 2015-06-11.
2. Michael Kelly, Normand Amyotte, Patrick M. White, Robert Chutu Li. Multi-Junction Solar Cell Characterization Instrument. PEO Student Paper Night, Ottawa (2014).

CONFERENCE PUBLICATIONS

1. J.P.D. Cook, Robert Chutu Li, J. Haysom, K. Hinzer, and H. Schriemer, "TETRA—Thermal Environment by Transient Response Analysis: Auto-Calorimetry Toward

Material and Structure Evolution Studies in Concentrator Photovoltaic Cells" Proc. NREL Photovoltaic Modules Reliability Workshop, Denver, 2015 downloaded July 17, 2015 from:
http://www.nrel.gov/pv/performance_reliability/pdfs/2015_pvmrw_36_cook.pdf (Poster)

2. Patrick M. White, Michael Kelly, Normand Amyotte, Robert Chutu Li, Anna H. Trojnar, Mark Yandt, Karin Hinzer. (2014). Multi-Junction Solar Cell Characterization Instrument Using the Fill-Factor Bias Measurement Technique. TEXPO Competition. TEXPO Competition, CMC Microsystems, Gatineau, Canada, 2014-10-06 (Poster)
3. P. M. White, Michael Kelly, Normand Amyotte, Robert Chutu Li, M. Yandt, and K. Hinzer. (2014). Multi-Junction Solar Cell Characterization Instrument Using the Fill-Factor Bias Measurement Technique. Next Generation Solar 2014. Next Generation Solar 2014 - Photovoltaics Canada - Fifth National Science Conference, Montreal, Canada, 2014-05-13 (Poster)
4. Arbez G, Walker A, Wilkins M, Wheeldon J, Li R, Hinzer K, Schriemer H. (2013). 4 Junction Dilute Nitride Solar Cell Optimization: Comparing Current Matching Approaches in Detailed Balance Algorithms. 39th IEEE Photovoltaic Specialists Conference. 39th IEEE Photovoltaic Specialists Conference, 2013-06-16 (2073 - 2077)

Acknowledgments

Firstly, I would like to thank my supervisor, Dr. Henry Schriemer, for his patient guidance and lots of discussions and help, without which the thesis is not possible to be accomplished as it is. Also, many thanks to my co-supervisor, Dr. Karin Hinzer, for her patience and kindness, the environment in SUNLAB she created in which I received help on many aspects, and her encouragement when I was to present on conference.

I am thankful to Dr. Joan Haysom for lots of help, discussions and advice on this project. Also thankful to Dr. John Cook's instruction and help on other project's work during the graduate program.

Thanks to Matt Wilkins, for his patience on my technical questions and discussions. Thanks to Ross Cheriton, specifically the server computer, the output analysis won't be able to accomplish in such time scale without your work on it. Thanks to Annie Russell, for her great work relating to this project during this summer, including but not limited to, adjusting functions to speed up computation, careful code checking and working closely in debugging, detailed code commenting, as well as output analysis.

Thanks also to all the SUNLAB colleagues for all the help throughout the two years.

Thanks to all the Celestica people involved in this project, especially to Rui Li and Mohsen Mahmoudysepehr for the data, information, explanation on my questions regarding to the project.

Lastly, many thanks to my wife, Shujie Wang, and daughter, Erin. It will not be possible without their understanding and support.

This research was performed at the SUNLAB, Center for Research in Photonics, University of Ottawa. My sincere gratitude to the financial supports provided by NSERC, and University of Ottawa.

List of parameters

** Due to the large number of parameters involved in this project, this list only contains those used in the mathematical modeling but not those appearing in literature review unless necessary. However, the symbols appear in literature review are identical to those in this project mathematical model if they are of the same concept or variable.*

symbol in thesis	***parameter meaning***
A	Area (m^2)
A_P	Panel total area (m^2)
A_{Pp}	panel patch area (m^2)
A_{sp}, (Ω_{Sp}) or $A_{Sp.i}$	Normalized sky patch area (equivalent to sky patch solid angles seen from ground)
c_{CT}	Short circuit current thermal coefficient (1/k)
$C_{ErBGPf.i}$, $C_{ErBGPr.i}$	Sun beam to ground reflecting to panel front and rear side error reduction factor
c_{VT}	Open circuit voltage thermal coefficient (1/k)
d_1, d_2	Horizontal distance between a panel patch center and the mid-point of a ground patch outer ring or inner ring (m)
D_{GpPp}	Space (3-D) distance between a ground patch and a panel patch (m)
DHI	Diffuse horizontal irradiance (W/m^2)
$DHI_{Measured}$	Measured DHI value at each time stamp provided from external source (W/m^2)
DHI_{Prep}	Sum up of sky patch contributions based on Perez model distribution formula as a preparatory parameter
DNI	Direct normal irradiance (W/m^2)
E	Averaged irradiance on the panel front and rear in total (W/m^2)
$E(\lambda)$	Photon energy (in Joule) at wavelength λ
EQE	External quantum efficiency
$f(Z_{Sp}, \chi)$	Preparatory value for radiance at sky patch center in Perez's 1993 model
f_{ab}	Backward anisotropic coefficient in Gueymard's model
f_{af}	Forward anisotropic coefficient in Gueymard's model

symbol in thesis	***parameter meaning***
f_{GeoGPf}	Factor containing all geometric information on ground patches toward panel patches, including viewing factor, solid angle and cosine of incidence angle on panel front and rear patches
$f_{GpPpComp}$, $f_{GpPpfComp}$, $f_{GpPprComp}$	Compensating information on ground patches' Lambertian reflection toward panel front and rear
$f_{NormDHI}$	Ratio of measured DHI over the sum-up DHI (DHI_{Prep}), used as a normalization factor
f_{PT}	Filtering ratio of panel transparent area
GHI	Global horizontal irradianc (W/m^2)
H	Hour angle (°)
I	Solar cell generated current (Ampere)
I_0	Regressed dark current per cell at STC (Ampere/cell)
$I_0(t)$	Simplified average solar cell diode dark current at real working condition radiance and field working temperature (Ampere/cell)
IAM	Incidence angle modifiers for panel front and rear side, same for any incidence, either sun beam, sky diffuse or ground reflection
I_{BG} *(W/m2)*	Sun beam irradiance on ground, i.e. $DNI*cos(\varphi_S)$ on every ground patch (W/m^2)
I_{BGPfNS} & I_{BGPrNS} *(W/m2)*	Reflected irradiance of sun beam by ground onto panel front and rear side without shading (W/m^2)
I_{BPf}, I_{BPr}	Irradiance on panel front and rear patches by sun beam with information of rear side post blocking (W/m^2)
I_{DT}	Sky diffuse irradiance on panel front and rear patches with blocking information on rear side (W/m^2)
I_O	Daily based extraterrestrial solar radiance (W/m^2)
IQE	Internal quantum efficiency
I_{SC}	Solar cell (panel) short circuit current from company provided I-V curve (Ampere /cell)
$I_{SC.STC}$	Solar cell short circuit current from photonic to electrical conversion at each solar cell if at 25°C (Ampere/cell)
$I_{SC.STC.AVE}$	Average of short circuit currents of all solar cells if at 25°C (Ampere/cell)
$I_{SC}(t)$	Short circuit current at field working temperature (Ampere /cell)

symbol in thesis	***parameter meaning***
$I_{SC.AVE}$	Average of real short circuit currents at field working temperature (Ampere/cell)
I_{Sp}	Actual irradiance from a sky patch (W/m^2)
$I_{SpPfNormalized}$	Normalized irradiance from isotropic conditioned sky patches toward panel front side
$I_{SpPrNormalized}$	Normalized irradiance from isotropic conditioned sky patches toward panel rear side w/o post blocking
k	Boltzmann constant (Joule/k)
L	Local latitude (°)
L_{Sp}	Relative value of diffuse radiance at any point on sky dome based on the Perez model diffuse distribution
$L_{SpActual.j}$	Sky patch center radiance values based on Perez 1993 sky model's distribution and summing up to measured DHI (W/*sr.*/m^2)
m	Regressed ideality factor of solar cell
M	Air mass
N_{GpAzD}	Ground patching azimuthal division number
n_{ARC}	Average refractive index of ARC layer
n_{EVA}	Average refractive index of EVA
n_g	Average refractive index of glass
n_{ITO}	Average refractive index of ITO
$NOCT$	Nominal Operation Cell Temperature (°C)
n_{SC}	Number of solar cells on panel
n_{Si}	Average refractive index of silicon
$P(\lambda)$	Photonic influx power at a given wavelength (Joule/m)
q	Electrical charge (Coulumb)
r	Radius (m)
$R(\theta)$	Reflectance at each interface of panel structure
R_{Gp} & r_{Gp}	Ground patch inner and outer edges' radii (m)
r_{PI}	Solar cell received photonic power to short circuit current conversion ratio under STC (Ampere/W)
R_S	Regressed series resistance per cell (Ω/cell)
R_P	Regressed parallel (shunt) resistance per cell (Ω/cell)
t	Standard test condition temperature in Kelvin (k)

symbol in thesis	*parameter meaning*
$T(\theta)$, $T_{Pf}(\theta)$, $T_{Pr}(\theta)$,	Transmittance of panel when at incidence angle θ, a ratio of photonic flux power right above the solar cell (should be above anti-reflection coating if there is such layer) and right after entering the solar cell exciton generation region
$T(\lambda)$	Transmittance at a wavelength at normal incidence, a ratio of photonic flux power right above the solar cell (should be above anti-reflection coating if there is such layer) and right after entering the solar cell exciton generation region
$t_{AmbientAir}$	Ambient temperature at test site (°C)
t_{Module} (also as *t*, solar cell working temperature in general formula)	Average temperature of all cells as identical at a time by simplification (*k*)
$T_P(\theta)$	The fraction of radiance power passing through panel towards ground, from the product of $f_{PT}*T(\theta)$
T_{PfN}	Front side normal incidence transmittances, concept same as $T(\lambda)$
T_{PrN}	Rear side normal incidence transmittances, concept same as $T(\lambda)$
V	Voltage (V)
$V_{OC}(t)$	Solar cell open circuit voltage under real field temperature (V/cell)
$V_{OC.STC}$	Solar cell open circuit voltage under working irradiance, but if at 25°C (V/cell)
$V_{OC}(t, I_{SC})$	Solar cell open circuit voltage at working condition radiance and field temperature (V/cell)
x_{Gp}, y_{Gp}	Ground patch central point Cartesian coordinates (m)
x_{Pp}, y_{Pp}, z_{Pp}	Coordinates of panel patch center (m)
Z_r	symbol representing a reflecting ray at a certain 3-D angle
Z_S	Solar zenith angle (°)
Z_{Sp}	Sky patch center zenith angle (°)
$\beta_{Gfp.in}$	Elevation angles from "far-field" ground patch inner edge centers toward a panel patch (°)
β_r	Ground reflecting rays' elevation angle toward a panel patch (°)
β_S	Solar elevation angle (°)
β_{Sp}	Sky patch center elevation angle (°)
γ	Horizontal angle between incidence and reflection (°)
δ	Solar declination (daily based) (°)

symbol in thesis	***parameter meaning***
Δ	Perez sky model parameter: sky brightness; and its adjusted value =0.2 when calculated value < 0.2
δ_γ	Selecting coefficient for backward and forward factors, δ_γ=1 when $cos(\gamma)>0$; otherwise δ_γ=0
ε	Perez sky model parameter: sky clearness
θ_{BPf} (Also as θ_S), θ_{BPr}	Incidence angle of sun beam toward panel front and rear sides (°)
θ_{GfpPp}	On-panel incidence angle of reflection from ground far field patch toward a panel patch (°)
θ_{GpPf} (& $\theta_{GpPr}=180° - \theta_{GpPf}$)	Ground reflecting rays' incidence angle information onto panel front and rear patches (°)
$\theta_{GpPpf.i}$ (& $\theta_{GpPpr.i}=180°- \theta_{GpPpf.i}$)	Any one of the ground reflecting rays' incidence angles information onto panel front and rear patches (°)
θ_{Pf}, θ_{Pr}	Incidence angle of any irradiance toward panel front and rear sides (°)
θ_{SpPf}, θ_{SpPr}	Incidence angles of sky patches toward panel front and rear side (°)
κ	Perez sky model parameter *kappa* (= 1.041 when solar zenith angle is in radians)
λ	Wavelength (m)
ρ	Mean daily diffuse reflectance
ρ_b	Gueymard's directional reflection from ground patches toward panel patches
ρ_d (ρ_d is almost equal to ρ)	Diffuse reflectance
ρ_n	Reflectance to a normal incidence beam, assumed isotropic
Σ_P	Panel tilting angle (°)
Φ	Photonic flux (W)
φ_{Pf}	Panel azimuth angle (°)
φ_S	Solar azimuth angel (°)
φ_{Sp}, β_{Sp} i.e. ($90°-Z_{Sp}$)	Sky patch central point azimuth and zenith angles (°)
χ	Angular distance between sky patch center and the position of the sun (°)
Ω_{GpPp}	Solid angle of ground patches viewed from panel patches (*sr*.)
$\Omega_{GpPpf.i}$, $\Omega_{GpPpr.i}$	Any of the solid angles of ground patch seen from panel patch, front or rear (*sr*.)
ω_{GpPpH}	Ground reflecting rays' azimuth angle toward panel patch (°)

Table of Contents

List of figures

List of tables

Chapter 1 Introduction and project background

1.1 Today's global energy issues and the solutions

Nowadays, there is energy requirement behind almost all human activities and about 90% of the energy is sourced from non-renewable fossil fuels [1, 2]. However, such consumption of non-renewable energy resources brings about problems of sustainability. Firstly, burning of these fossil fuels destructively impacts the environment by pollution and greenhouse effect. The impacts may even further aggravate with the global economic development, increase of population and living standards. Secondly, there is a limit on any of the fossil fuel reserves which will be exhausted eventually. For human being to have a more sustainable and responsible long-term development, there is a need to change the way(s) of energy use as well as specifically shifting the types of energy source. Here, renewable energy sources such as wind, hydro, geothermal, biomass, and photovoltaics (PV) may play the most important role as they are clean, sustainable, and never exhaust.

Of all energy sources, the sun is the principal and primary offeror. The sun is estimated to continuously emit at 3.8×10^{20} MW of radiation [3]. Even the tiny fraction of such a tremendous amount reaching the earth surface is so abundant that one hour of such received radiation energy is greater than the global annual energy consumption [4]. The ways to harvest from such abundancy may include:

1. Solar thermal collectors use heat-absorbing panels to heat water or warm up buildings. To make the best possible use, usually, mirrors are used to focus the sun's reflected rays on heat-collecting elements;
2. Passive solar design is usually relating to building designs of windows, walls, and floors, in such a way that they are made to collect, store, and distribute solar energy in the form of heat in the winter and reject solar heat in the summer;

3. The photovoltaic (PV) cells convert solar radiation directly into electricity by using photovoltaic semiconductor materials. PV cells operate without pollution, neither moving parts hence no noise.

1.2 Photovoltaics, Problems Solar cells facing nowadays and the solutions

Solar cells were invented and then developed in 1960's as power provider in space use. It received focus in 1970's oil crisis in seeking alternative energy sources. Rapidly, the solar cells' advantage of remote use was highly recognized, and in turn, it promoted the development of the whole photovoltaic industry. The solar cell record efficiency increased, and a silicon cell reached up to 20% efficiency milestone in 1985. In the next decade, a 15% to 20% steady growth rate was seen of the photovoltaic industry, and reached a 38% in 1997 [5]. Meanwhile an exponential increase of annual solar power installation has been experienced [6].

Currently, the semiconductor materials mostly used are monocrystalline silicon, polycrystalline silicon, amorphous silicon and cadmium telluride, where crystalline silicon PV systems together have more than 85% of today's market share and thin film technologies (such as CdTe and amorphous silicon) takes most of the rest [7].

The major problem hinders solar cells electricity market share is that solar cell generated electricity lacks economic grid parity with market price. The problem is temporarily addressed by government subsidy and tariff programs [8, 9], but, the thesis author expects it must eventually be resolved by the technology itself. The Levelized Cost of Electricity (LCOE) is the net present value of total life cycle costs of the project divided by the quantity of energy produced over the system life [10]. Ways to reduce LCOE may be increasing efficiency including good maintenance, reducing cost and lengthening solar cell working lives. One of the ways to increase efficiency is the application of bi-facial solar cells which collect irradiance from both front and rear sides, thus boosts power output.

1.3 History of bi-facial solar cells development

Comparing to mono-facial solar cell, a bifacial solar cell can receive irradiance from both front and rear side so is capable to output more energy when using the same area of land [11]. Moreover, because of the absence of aluminum back metallization, hence the reduced infrared absorption, bifacial solar cells have a lower working temperature given the same irradiance. This may provide extra power output [12].

Bifacial solar cells can be categorized into three types of structural designs: a) two PN junctions, b) one PN junction and one high-low junction, and c) one PN junction only. Among the three types, bifacial solar cell with one PN junction and one high-low junction is the prevalent design. A bifacial solar cell of such structure design consists of bulk (P or N-type semiconductor), emitter , back surface field (BSF), anti-reflective coatings (ARC) as well as bus bars and fingers on both front and rear sides for collecting charges and contact to external circuit. The two junctions may consist of N+PP+ [13], NPP+ [14] [15] (Figure 1), and also may be structured as P^+NN^+, P^+PN^+, or N^+NP^+.

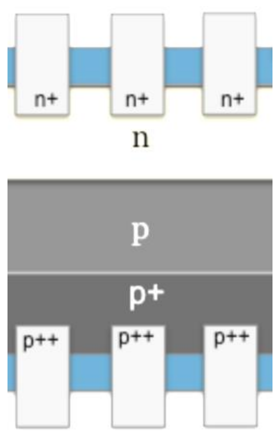

Figure 1 An NPP+ bifacial solar cell cross-sectional structure [15]

1.3.1 Bifacial solar cell development history

In 1960s, Mori patented a device with two p-n junctions back-to-back on each surface of a silicon wafer. With the extra p-n junction, it was purposed to increase the long-wavelength photons collection efficiency (Figure 2)[16]. This in fact becomes the first design of semiconductor device possible to receive irradiance/illumination from both sides. Later in 1980s, Luque et al. [17] used the idea in photovoltaic (PV) solar cell to improve energy output.

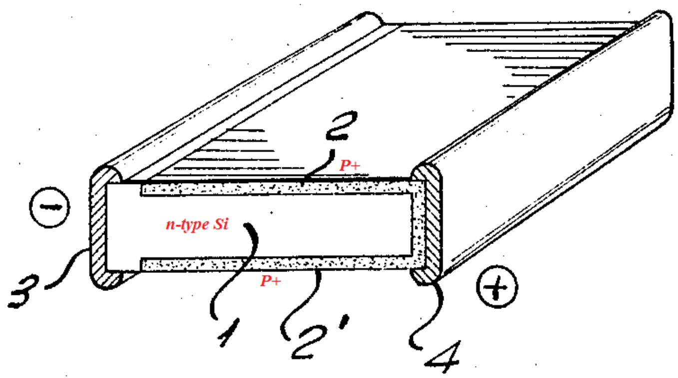

Figure 2 Mori's patent for receiving irradiance from both sides [16]

On the other hand, in 1970s, Bordina et al. devised and illuminated a silicon solar cell simultaneously from front and rear sides [18, 19], here, the two junctions are in series (Figure 3). In 1981, with help of a concentrator collecting more albedo, Cuevas et al. showed a 50% high boost in electrical output by using bifacial solar cell (Figure 4) [20].

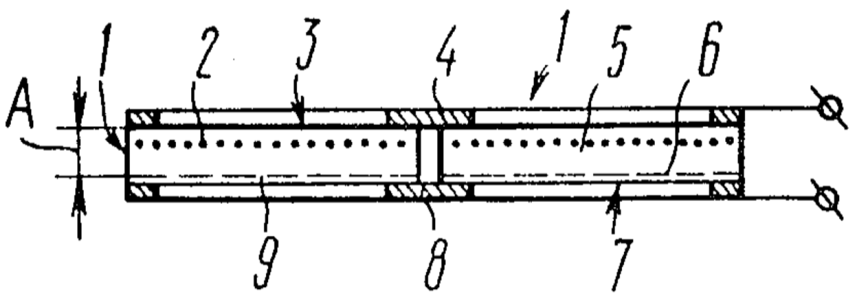

Figure 3 the first actual bifacial Back Surface Field solar cell design where in the figure, "2" indicates a P+P junction and "6" indicates a PN junction [18]

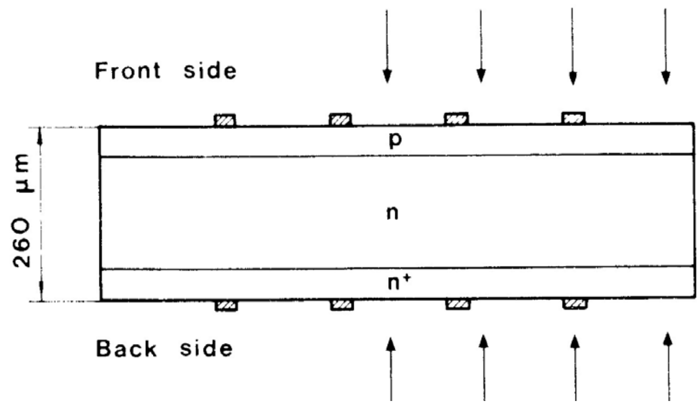

Figure 4 P+NN+ structured solar cell receiving illumination from both sides [20]

In early 1990s, Moehlecke et al. at the University of Madrid incorporated pyramidal texturing and used an optimised phosphorus emitter for their bifacial solar cell and 19.1% and 18.1% conversion efficiencies respectively [21].

1.3.2 Recent development

The recent bifacial researches focus on a few aspects [22]:

- Bifacial solar cells (especially silicon substrate) technology, including substrate and its thickness, thermal processes, passivation, texturing and contacts, converters, as well as conversion efficiencies;
- Bifacial module/panel design, encapsulation, module efficiency, reflectors, and spectral albedo effects;
- Concentrators and tackers for bifacial solar cells or panels;
- Bifacial cell and panel testing and corresponding standards;
- Bifacial solar farm deployment and optimization.

It is suggested that the research efforts should continue on improving bifacial cell efficiency and conversion efficiency, module reliability, farm deployment configuration, certification procedure standardization [22].

1.3.3 Specific researches relating to bifacial in field performance experiment and simulation

1.3.3.1 Tilt angle:

Ota et al. experimentally explained that bifacial panel should be tilting at the latitude angle to receive the most irradiance from front, and since the higher the tilting angle the more irradiance can be received by the rear side, henc they inferred that bifaicial can achieve a higher percentage of boost in higher latitude places [23]. This may be that, with a higher tilting angle, the rear side, especially its bottom part can see more of the sky, and more of ground outside of the panel self-shaded near ground. Moreover, tilting angle also controls seasonal gain variations [24].

1.3.3.2 Clearance:

Clearance dramatically affects back irradiation [24]. Ota et al. concluded from their experiment that a bifaical panel should be at least 80 cm above ground (Figure 5) [23].

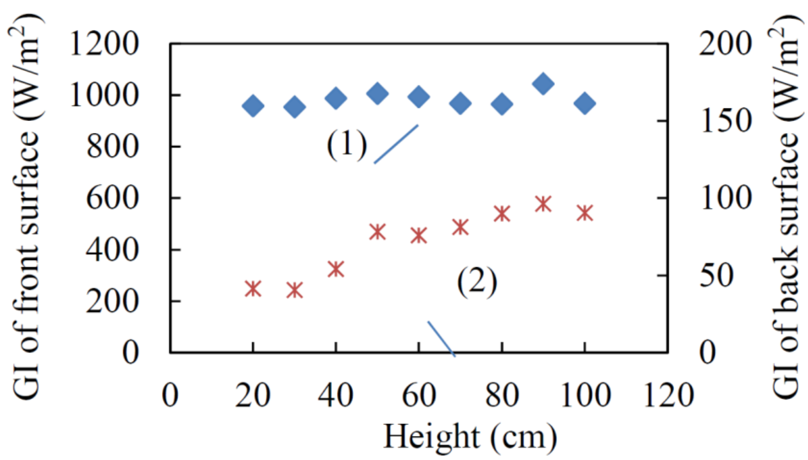

Figure 5 global irradiance on front side (1) and rear side (2) vs. panel clearance [23]

Kreinin et al. also observed that non-umiformity of rear side irradiance is the limiting factor of rear side energy contribution; clearance is the most important factor influencing rear side irradiance uniformity, and a higher clearance increases the total output (Figure 6) [24].

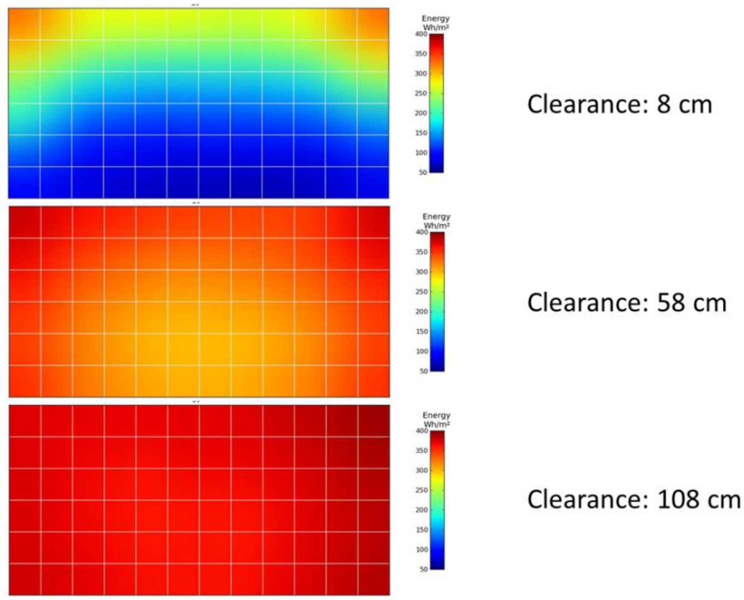

Figure 6 Rear side irradiance on 30° tilted module on May 30, 2010 in Jerusalem, Israel (31°47'N), GHI=1006 W/m^2, diffused to global radiation ratio of 0.11, underlying surface reflectance 50%; the brighter panel central part is due to a reflecting clothing with a much higher albedo than turf grass further away [24].

Kreinin et al. showed that when panel clearance increases from 8 cm to 108 cm, the difference between the solar cells' maximum and minimum power narrows significantly (Figure 7) [24].

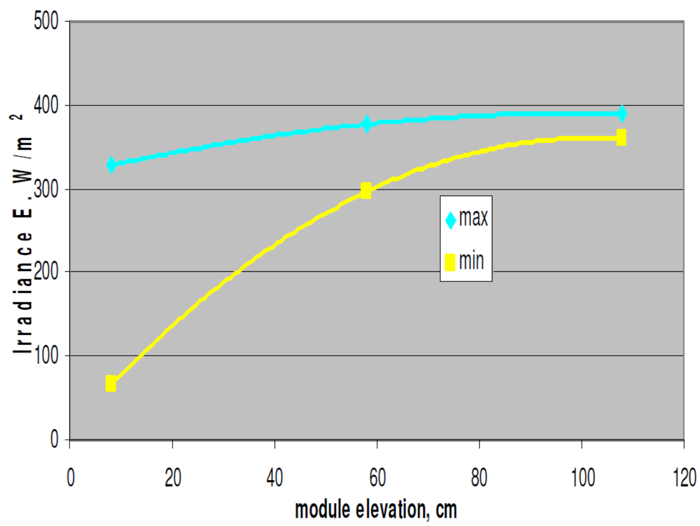

Figure 7 Changes of panel rear solar cells' maximum and minimum irradiances vs panel clearance; minimum and maximum back irradiance on solar cells, south orientation, and tilt at 30° [24]

1.3.3.3 Albedo

Yusufoglu et al. did simulation of "bifacial modules with revision of ground reflection" [25]. They concluded that albedo almost proportionally increases the bifacial gain, which has been supported by Ota's and Kreinin observations [23, 24]. However, Yusufoglu's model simplifies many of the factors, and neither considered the issue of racking blocking panel corners (Figure 8).

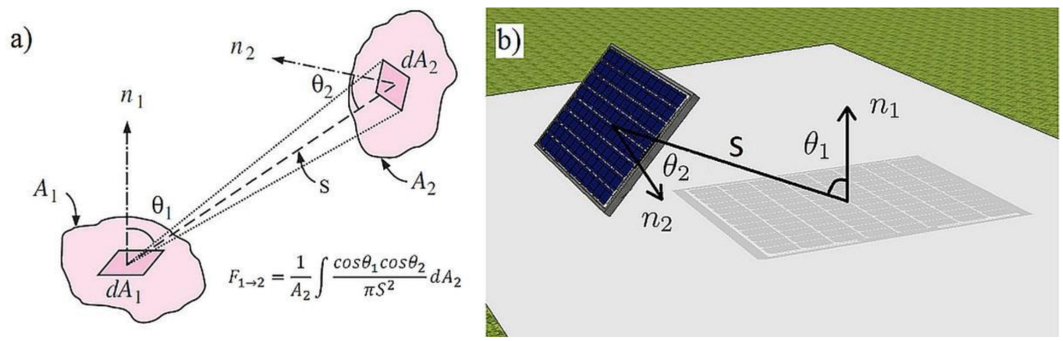

Figure 8 Simulation of panel shading by Yusufoglu et al. [25]

1.3.3.4 Sky diffuse and cloudiness

Both Kreinin and Ota observed that bifacial gain is greater in cloudy days [23, 24]. Ota et al. further concluded that bifacial should have more advantage over mono-facial in regions having higher humidity, more scattered or diffuse light, and more cloudy days [23].

1.3.3.5 Front and rear side power

Setting the bifacial panels vertically facing east and west, Johnson et al. used the same one diode model for front and rear side, and applied a simple summation of power from both sides, gives a good match with measured power output [26]. Castillo-Aguilella also simply added energy from front and rear in their model, and their results match well with third party bifacial data within a 3-4% error [27].

1.3.3.6 Front and rear side current

Matsukuma observed in 1994, that increasing of additional rear irradiation proportionally increases the total short circuit current and slightly increases the total open circuit voltage [28]. Ohtsuka in 2001, more clearly stated that, for those bifacial solar cells with their two junction in series, the total short circuit current is simply the sum from front and rear sides, and dark current under bifacial illumination is also almost equal to that under either front or rear illumination [29].

A recent investigation by Deline et al. showed that the power outputs from indoor front and rear side illumination tests have a very good linear relationship with the outdoor bi-sided illumination test result, this also proved that the front and rear side power can be linearly summed up [30]. Again, their experimental setup and simulation of panel shading did not take the panel racking blocking into consideration as should be in real farm practice (Figure 9).

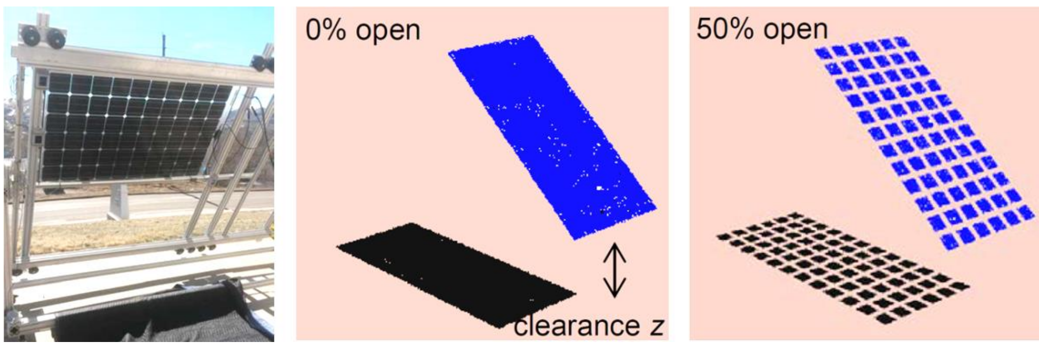

Figure 9 experimental setup and simulation of panel shading by Deline et al. [30]

1.3.3.7 Panel setup details in existing experiments and corresponding simulations

From the above mentioned simulations, the models usually simplified the situations, neglected a few factors, and none of them have taken into consideration of the shading or ray blocking by panel racking. Such simplifications may be acceptable in investigating certain parameters, but may bring about noticeable amount of error in calculating energy yield for real systems.

Based on research up to date, there is no specific simulation software existing which can simulate bifacial modules/panels on racking, nor any software with all the geometric parameters adjustable to deal with all the possible scenarios.

Besides, experiments in such field are costly, and especially take up very long time. Moreover, to obtain quantitative impacts by certain generic conditions or influential factors, it may require controlled surrounding conditions of which are unlikely satisfied most of the time. Therefore, there is need of bifacial solar cell and panel modeling simulation for real scenario with details and with output at high accuracy.

1.4 A project is shaped between Celestica and SUNLab, University of Ottawa

Celestica is a main bifacial solar panel manufacturer in Ontario and provides products in Canadian as well as international markets [31]. As above recounted, the bifacial solar cell output is related to a few more factors than mono-facial. Also, how much of power output boost vs. cost increase is also the concerns of customers in the market. Hence, as a manufacturer, Celestica has a sincere interest in the factors and correlations around bifacial solar panels, their deployment environment and output.

SUNLAB at University of Ottawa is a research center focusing on researches in photovoltaics (PV) with strong modeling and computing capabilities in these fields [32].

A project of "Bifacial Photovoltaic Energy Yield Analysis" is agreed by the two parties on a detailed model to create an accurate simulation of the irradiance on the bifacial cells over a range of irradiance conditions and deployment configurations, and to predict the corresponding energy yield.

1.5 Objectives of this project

Considering ground shading by panels and racking, and racking shading on panel rear side, to develop a ray-tracing model, for the solar beam, sky diffuse radiance, ground, as well as panels and racking.

A complex model with deployment parameters: surface albedo, panel tilt over 0° to 90°, i.e. horizontal to vertical; and panel azimuth angle from 90° through 0° to -90°, i.e. E-S-W; irradiance conditions, and temperature. The model should include the following:

- Solar beam, and the anisotropic, weather dependent distribution of diffuse radiance over the sky dome;
- The above said irradiances received by the panel front and rear side with consideration of racking shading on the rear side;

- With a simplified horizontal ground extending to infinite, calculating the above said irradiances received on the ground after shadowing by the solar panels and racking (but leave an easy-to-add possibility to add other near-field reflecting surfaces such as buildings, trees, uneven surfaces in future projects);
- Ground of commonly seen surface coverings with a wide range of albedos, angular distribution of ground reflections for such surfaces, considering directional and/or Lambertian characteristics where appropriate;
- Reflection from shaded ground surfaces to calculate ground reflection and the non-uniform 2D distribution on the panel rear as well as the front surface (more complicated on rear side as there is racking blocking the ground reflection);
- the resulted angular information for all the impinging on the panel front side and rear side (the angular information is used in irradiance calculation as well as panel optical transmittance calculation);
- The effect of incidence angle modifiers on the irradiance at the cell junction;
- Conversion of the 2D distribution of front and back side light into net module current;
- Effect of cell temperature;
- Panel electrical performance simulation and eventually electrical power output.

Output parameters that must be specified include:

- Different angles of incidence (incidence angle modifiers) so to quantify the effect of a shadings of all kind of the irradiances;
- Detailed description of the cell semiconductor structure, including the appropriate equivalent solar cell diode circuit model, panel series and shunt resistance, as well as panel materials and anti-reflection coating properties relating to the energy yield simulation;
- Comparison of the yields between the bifacial and a mono-facial of the same quality, and quantify the boost;
- The completed model will need to be run for hourly time stamps over an entire year to evaluate net energy yield, and under a range of surface environments. Simplification is inevitable for simulation modeling with such complexity. The modeling strategy must

determine optimum balance between complexity and computational efficiency while maintaining good accuracy. Therefore, an evaluation of simplifications vs. loss of accuracy is also an objective of the model.

Innovation:

To the author's best knowledge up-to-date, there are no commercial packages that are presently able to accomplish simulation model containing such details and complexity, ranges of deployment and parameters as listed above. This way, it is expected to be capable in more multi-factorial analysis, with higher accuracy, and closer-to-reality outputs.

1.6 Thesis Overview

This thesis comprises six chapters of which this is **Chapter 1**. It starts with the broad global energy issues as background, and point out that photovoltaic solar cell is one of the solutions, and specifically, bifacial solar cell technology is one to achieve higher energy output without much increase in cost. Then, it continues on a general literature review on bifacial development. Based on the general research, the chapter ends with the description of the project's objectives.

Chapter 2 is for further detailed literature review on the defined project. There are three main parts for the research. The first part is the radiance from sky, including the beam and the diffuse radiance from the sky dome; the ground reflection or albedo; and the bifacial solar cell. They are formed into three sections in this chapter. Each section ends with the choice of what model to be used for simulation.

Chapter 3 is about mathematical model build-up based on the chosen models. The chosen models are described in details. The sun is modeled as a point source, and the beam radiance is relatively simple. The sky dome diffuse radiance distribution is modeled based on Perez's 1993 model [33]. The ground reflection of sky diffuse irradiance is simplified as Lambertian (isotropic) reflection, while the reflection of direct solar beam is modeled as directional reflection using Gueymard's model [34]. The shading of panels and their racking on ground, as well as the racking posts shading on panel rear side are also discussed and taken into the model. Possible simulation errors are analysed, pin-pointed as mainly in ground reflection calculation due to patching, and dealt with compensation. Panel optical transmission models are built separately for rays captured by solar cells, and rays passing through gaps between solar cells reaching ground beneath the panel. Chapter three ends with the solar cell and panel model including the consideration of panel working temperature, photonic power conversion to short circuit current at each cell, and the total panel power output based on the combination of each cells I-V curves the maximum power point on the total panel I-V curve.

Chapter 4 describes how the whole system and its components are modeled, namely, the sky dome, ground, and panel geometries, solar cells and panels optical path, solar cells photonic to electrical power conversion. Then further describes how to convert the mathematical model into simulation algorithm, and specifically gives detailed explanations to those functions with high complexity.

Chapter 5 is about analysis and discussions. Two parts are included. The first part is to check the simulation model's quality, the second part is to analyse the bifacial related phenomena with discussions on corresponding reasons.

Chapter 6 is a short chapter gives summarize the obtained results, and provides suggestions to further studies on this topic.

Chapter 2 Literature review on project simulation components modeling

The model should consist of three parts: the sources, solar irradiance collection, and the photoelectric conversion. A bi-facial solar panel receives irradiance directly from the sun (DNI), from the sky light (diffuse light), as well as ground albedo. This chapter is to research on these topics to help choosing and/or design the most proper corresponding sub-models for each of the model components.

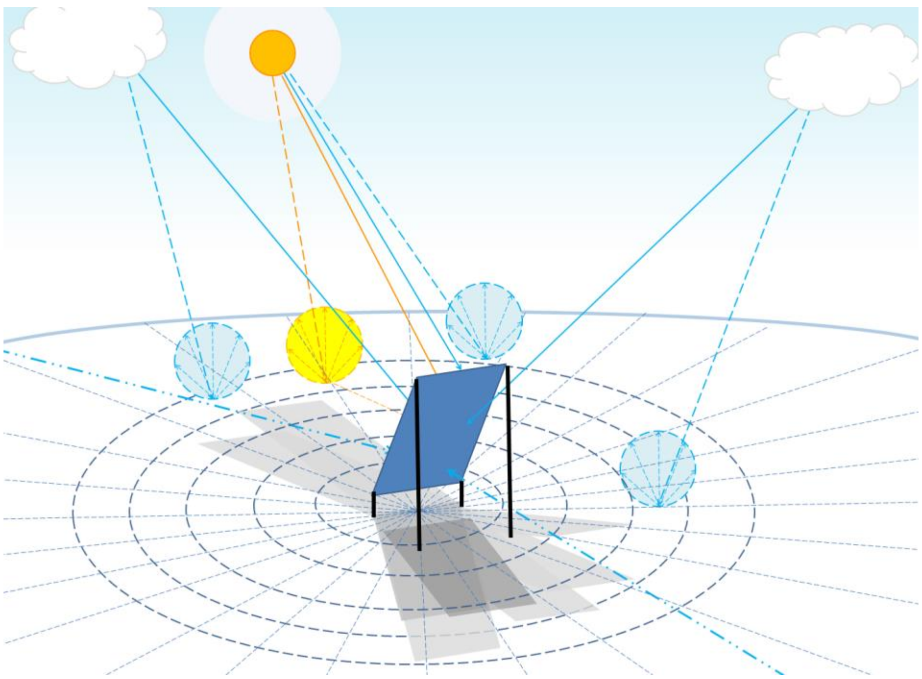

Figure 10 Schematic diagram of bi-facial panel under radiation

2.1 Sky modeling, Sky diffuse radiance models and the choice

The sources in the sky include the sun, and diffuse radiance from all over the sky. The sun may be modeled as a point source radiates onto ground and panel. The model also takes consideration of shading and blocking based on geometry.

The sky diffuse model is the most complicated component in sky radiance modeling. A brief review of mostly used models are categorized in two groups, and a choice is made at the end based on a balance of the output quality and model complexity.

2.1.1 Direct sun beam radiance on ground

The ground irradiance from sun beam may be calculated as [3]:

$$I_{BG} = DNI\cos(Z_S) \tag{2.1}$$

Where I_{BG} means sun-beam-to-ground irradiance, DNI is a measured value of direct normal irradiance, and Z_S is the zenith angle of the sun. The sun's zenith angle, elevation angle and azimuth angle may be correspondingly obtained from formulas below [3]:

$$Z_S = \arccos[\cos(\mathrm{L})\cos(\delta)\cos(\mathrm{H}) + \sin(\mathrm{L})\sin(\delta)] \tag{2.2}$$

$$\beta_{\mathrm{S}} = 90° - Z_S \tag{2.3}$$

$$\varphi_S = \arcsin\left[\frac{\cos(\delta)\bullet\sin(\mathrm{H})}{\cos(\beta_{\mathrm{S}})}\right] \tag{2.4}$$

Where L is the local latitude, δ is solar declination of the day, and H is the hour angle. The calculations for δ and H are detailed in Masters's book "Renewable and Efficient Electric Power Systems" [3].

The panels and racking posts shade and block sun beam on ground. These are discussed in sections 3.4.1 . For solar azimuth angle, in spring and summer, in early mornings and late afternoons, the sun can be seen north of observer's position in day time, i.e. the sun azimuth angle may be more than 90°. Since $\sin\varphi_S = \sin(180° - \varphi_S)$, therefore, there is a checking condition:

If $\cos(H) \geq \frac{\tan(\delta)}{\tan(L)}$, then $|\varphi_S| \leq 90°$, otherwise, $|\varphi_S| > 90°$.

The air mass value at any time when the sun is above horizon is calculated using revised formula provided by Kasten et al. [35].

$$M = \frac{1}{\cos(Z_S) + 0.50572 \bullet (96.07995 - Z_S)^{-1.6364}} \tag{2.5}$$

2.1.2 Direct sun beam radiance on panel

The irradiance from sun beam onto a panel of any azimuth and tilting angles requires a checking condition for which side is facing the sun at the time being, this may be done by calculating the incidence angle of the radiation [3]:

$$\theta_{BPf} = \arccos[\cos(\beta_S)\cos(\varphi_S - \varphi_{Pf})\sin(\Sigma_P) + \sin(\beta_S)\cos(\Sigma_P)] \tag{2.6}$$

Where β_S and φ_S are solar elevation and azimuth angles respectively, Σ_P and φ_{Pf} are panel front side tilting and azimuth angles respectively. Since the sun is simplified as a point source, which side of the panel is facing the sun at any given time becomes mutually exclusive. If $\theta_{BPf} < 90°$, the panel front side is facing the sun. The irradiance on panel front side may be calculated as:

$$I_{BPf} = DNI\cos(\theta_{BPf}) \tag{2.7}$$

If $\theta_{BPf} > 90°$, the panel rear side is facing the sun, and the incidence angle on the rear side θ_{BPr} is the supplementary of θ_{BPf} . i.e. $\theta_{BPr} = 180° - \theta_{BPf}$, and the irradiance onto the rear side is $I_{BPr} = DNI\cos(\theta_{BPr})$.

The panel posts block sun beam on the panel rear side. Checking of such blocking will be discussed and modeled in sub-section 3.4.2 .

2.1.3 Models with sky dome divided into radiance-based sections

The simplest sky diffuse model is the isotropic sky model which assumes the luminance everywhere to be the same [3] and the diffuse radiation received on a collector (in our case, the front side of solar panel facing upward) may be expressed as:

$$I_{DT} = DHI\left(\frac{1+\cos\Sigma_P}{2}\right) \quad (2.8)$$

where I_{DT} is the diffuse irradiance received on the front side of the (usually tilted) panel, and Σ_P is the panel tilting angle regarding the side upward-facing.

Such a simple model may give a good result when simulating overcast sky but not for other sky conditions. There are other models take the anisotropy into consideration. It is needed to point out that, even for these anisotropic models, it is still unable to deal with the unpredictably ever-changing cloud distribution. Hence the sky is simplified as clouds being evenly covering over the whole sky dome but varying in thickness. Among these models, Hay-Davies model took the brighter circumsolar region into consideration by introducing an anisotropic index defined as below and gives the whole expression as [36]:

$$I_{Total} = (\mathrm{I_{BG}} + DHI \bullet \mathrm{A})\,\mathrm{R_b} + DHI(1-\mathrm{A})\left(\frac{1+\cos\Sigma_P}{2}\right) \quad (2.9)$$

Where *DHI* is the global diffuse horizontal solar irradiance; *GHI* is the global horizontal solar irradiance (this may be deleted if they are defined previously); R_b is variable geometric factor which is a ratio of tilted and horizontal solar beam irradiance; i.e. $R_b = \frac{DNI\cos(\mathrm{Z_S})}{DNI\cos(\theta_{BPf})} = \frac{\cos(\mathrm{Z_S})}{\cos(\theta_{BPf})}$; $A = \frac{DNI}{I_O}$ is the anisotropy index, in which I_O is the direct extraterrestrial normal irradiance. When A=0, the sky is considered as overcast by the model, and this expression collapses to the isotropic model.

Klucher added two terms in his model to cope with the brighter circumsolar and horizontal band [37]:

$$I_{Total} = \mathrm{I_{BG}}\mathrm{R_b} + DHI\left(\frac{1+\cos\Sigma_P}{2}\right)\left[1+F'\left(\sin\frac{\Sigma_P}{2}\right)^3\right]\left[1+F'(\cos\theta_{BPf})^2(\sin Z_S)^3\right] \quad (2.10)$$

where the clearness index $F' = 1 - \left(\frac{DHI}{GHI} \right)^2$ which becomes zero when it is overcast leads the model back to isotropic; and $\left[1 + F' \bullet \sin^3 (\Sigma_P / 2) \right]$ deals with horizontal band brightening; and $\left[1 + F'(\cos \theta_{BPf})^2 (\sin Z_S)^3 \right]$ for the effect of circumsolar radiation. When it is overcast, the clearness index *F'* becomes zero and the model reduces to the isotropic model.

Reindl et al. further added a term to take the horizontal bright band into their model. Since this extra term is always greater than unit, their model gives a higher output than Hay-Davies model [38, 39].

$$I_{Total} = (\mathrm{I_{BG}} + DHI \bullet \mathrm{A})\, \mathrm{R_b} + DHI(1 - \mathrm{A}) \left(\frac{1 + \cos \Sigma_P}{2} \right) \left[1 + \sqrt{\frac{I_{BG}}{GHI}} \left(\sin \frac{\Sigma_P}{2} \right)^3 \right] \quad (2.11)$$

From 1986 to 1990, Perez published a series of papers on his sky diffuse model. They also modeled the diffuse light as three parts: the sky dome as an isotropic background, the circumsolar brighter region and the horizon band brighter region. And further they created a way to determine the shares of radiance for the three parts under different types of sky conditions [40-42]. This model is comparatively more computationally intense and more analytically detailed.

They categorized sky conditions using sky clearness ε which is defined as:

$$\varepsilon = \frac{\frac{(DHI + DNI)}{DHI} + \kappa Z_S{}^3}{1 + \kappa Z_S{}^3} \quad (2.12)$$

where κ (kappa) is a zenith angle constant equals to 1.041for Z_S in radians [40].

Another parameter is sky brightness Δ:

$$\Delta = \frac{DHI \bullet M}{Io} \quad (2.13)$$

where M is relative air mass determined by solar elevation angle [35], and I_O is extra-terrestrial irradiance.

From Perez's 1990 radians [40], the diffuse irradiance incident on a tilted plane can be calculated as:

$$I_{DT} = DHI[(\frac{1+\cos\Sigma_P}{2})(1-F_1') + F_1'\frac{\cos\theta_{BPf}}{\cos Z_S} + F_2'\sin\Sigma_P] \tag{2.14}$$

where F_1' and F_2' are circumsolar anisotropy coefficient, and horizon band anisotropy coefficient respectively. The value set for F_1', F_2' are further determined under various sky conditions.

Although above models take either one or both of the circumsolar regions and horizontal band into consideration provide results closer to reality than isotropic sky model. However, the sky diffuse radiance distribution is continuous and changing constantly.

2.1.4 Models with continuously changing sky diffuse radiance

A set of more sophisticated and closer-to-real sky models is suggested by Commission Internationale de l'Eclairage (CIE) (also International Commission on Illumination in English) produce a set of spatial distributions of daylight [43]. The sky conditions are classified as 15 types from overcast to "White-blue turbid sky with broad solar corona". The distribution strongly replies on the position of the sun. The position of any sky element is defined by its zenith angle, Z_{Sp}, (subscript *Sp* for sky element or patch position) and by the azimuth difference between the element and the sun $|\varphi_{Sp} - \varphi_S|$. The angular distance between the element and the sun may be calculated as:

$$\chi = \arccos[\cos Z_S \bullet \cos Z_{Sp} + \sin Z_S \sin Z_{Sp} \cos|\varphi_{Sp} - \varphi_S|] \tag{2.15}$$

The distribution is obtained through the luminance ratio of a sky element anywhere on the sky dome to that at the zenith:

$$\frac{L_{Sp}}{L_{Zenith}} = \frac{f(\chi)\varphi(Z_{Sp})}{f(Z_S)\varphi(0)} \tag{2.16}$$

where $f(\chi)$ relates the relative luminance of a sky element to its angular distance from the sun:

$f(\chi) = 1 + c[\exp(\mathrm{d} \bullet \chi) - \exp(\frac{\mathrm{d} \bullet \pi}{2})] + e\cos^2 \chi$, and the luminance function:

$\varphi(Z_{Sp}) = 1 + a \bullet \exp(b / \cos Z_{Sp})$ for $0 \le Z_{Sp} \le \frac{\pi}{2}$, where *a*, *b*, *c*, *d*, and *e* are empirical parameters taking different values for different types of sky.

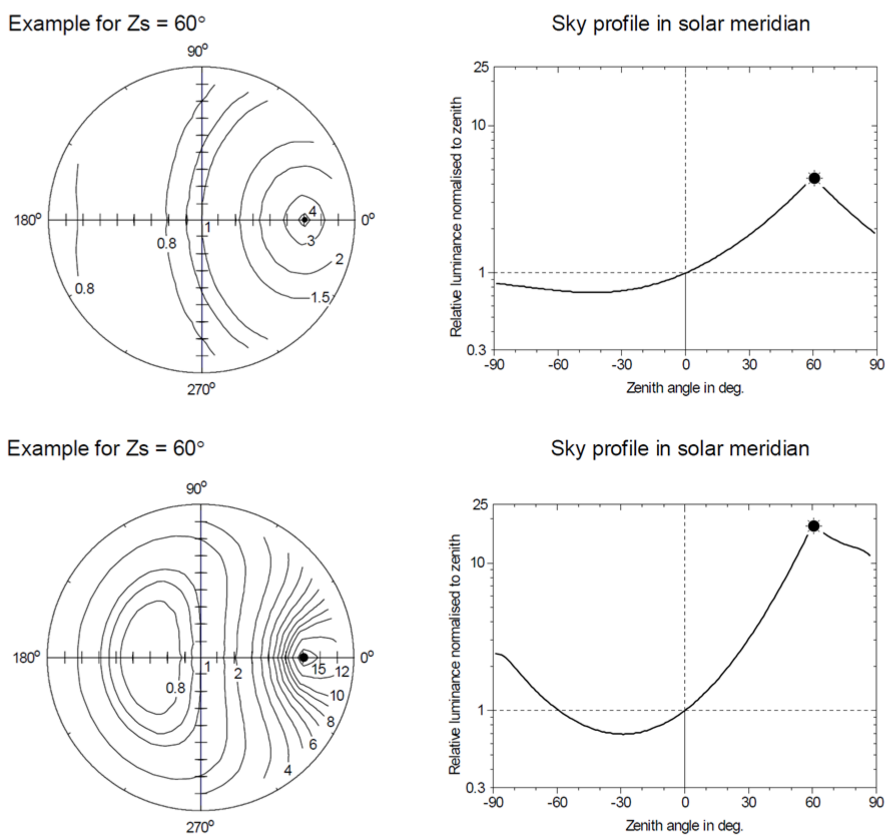

Figure 11 Sky continuous distributions from CIE models. upper: intermediate sky condition, lower: sunny sky condition [44]

Similar to CIE models, in 1993, Perez et al. also developed a set of sky models with simpler parameterization and classified sky into 8 types [33], and provided results with high fidelity comparable to CIE models [45] and even better results in certain circumstances [46]. Their model uses the same sky clearness ε as in their earlier 3-section sky model to categorize sky conditions as well as the sky brightness Δ [33]. Then the relative luminance is introduced using a set of parameters *a, b, c, d,* and *e,* and further these parameters are calculated from formulas with coefficients whose values determined by sky conditions.

2.1.5 Determining model selection

The distribution of diffuse irradiance over the sky dome is continuous and gradually varying, and is expected to be the closest to the reality, thus gives the best simulation results. On the other hand, comparing CIE model and Perez's 1993 continuous distributive model, we choose Perez model in this project as it is simpler in calculation and gives a very good result and even better than CIE model [46]. The Perez's model will be described in details in section 3.2 .

2.2 Ground reflection modeling

Albedo is defined as the ratio of energy reflected by an object to the corresponding radiation [47].

In this section, Bidirectional Reflectance Distribution Function (BRDF), as well as a few reflection models are reviewed.

After the review and comparison, a conclusion is drawn that Gueymard's model deals with directional reflection, and gives a set of numerical data for typical ground types, most suitable to our needs.

Furthermore, the reflection of sky diffuse radiance is simplified to be Lambertian only since such radiance comes from all directions and the anisotropic component in the reflection washes out, while the reflection of beam radiance is kept as Lambertian plus directional to maintain a more real outcome.

2.2.1 A brief review on reflection models

First conceptually introduced by Fred Nicodemus in 1965 [48], the Bidirectional Reflectance Distribution Function (BRDF) describes how much of an incoming light (irradiance) is reflected towards a certain direction:

$$f(\mathrm{x},\theta_i,\varphi_i,\theta_o,\varphi_o)=\frac{dL_o(\mathrm{x},\theta_o,\varphi_o)}{dE(\mathrm{x},\theta_i,\varphi_i)} \tag{2.17}$$

where θ and φ are respectively ray incidence and azimuth angles regarding to the reflecting surface at the incidence position, subscripts *i* for ray coming into and *o* for ray reflecting out from the position x on reflecting surface. The performance of reflection varies not only along with the angles, but also with the surface material properties, especially roughness.

There have been a number of BRDF models developed for such varieties since then. For those theoretically based models, they try to accurately simulate light scattered by using physics laws, but they usually lead to complex expression and high computational effort. While for those experimental models, the BRDF can be acquired from measurement and data processing, it may require a vast amount of measured data bank. Furthermore, some of the models are specifically for manmade materials and/or low roughness surfaces which are not applicable in ground reflection.

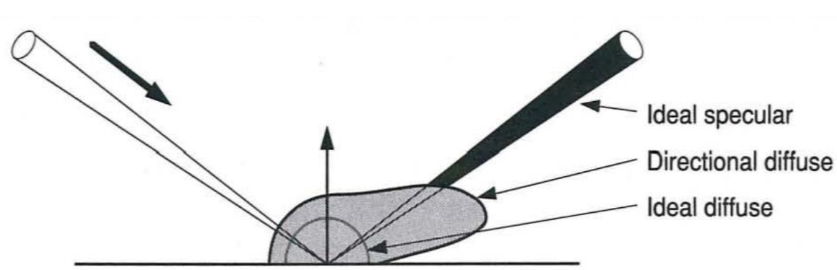

Figure 12 composition of reflection [49]

The general reflection in terms of modeling can be considered as a combination of specular reflection (also called surface reflection) and diffuse reflection (also called body reflection), and diffuse reflection can be further considered as a composition of directional and uniform (Lambertian) diffuse reflections (see Figure 12). The ideal diffuse, taken as uniform diffuse, is attributed to multiple surface and/or subsurface reflections. The ideal specular reflection and directional diffuse result from the first-surface reflection process (see Figure 13) and are respectively due to specular reflection by the mean surface and diffraction scattering by the surface roughness [49].

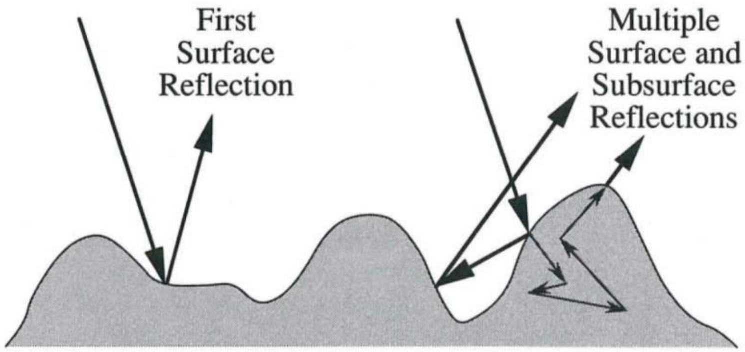

Figure 13 Reflection processes at a surface [49]

It can be seen that all these models are either complicated, or require quantitative inputs mainly from vast large amount of measured data bank less to mention the burden of huge amounts of computation workload [50].

2.2.1.1 Papers for isotropic modeling

On the other hand, the simplest reflection model is the Lambertian reflection model [51].

Ineichen et al. concluded that a constant averaged measured albedo gives the best results for transposition to tilted surfaces when assuming the ground-reflected radiation to be isotropic. They stated: "the isotropic model with an albedo known for the site under consideration is the model to be used and that the other complications which we could introduce are not justified in most cases" [52].

Domain et al. found out that, in area where it is very often cloudy, isotropic albedo models actually give lower error than anisotropic models [53].

Another paper concludes that the advantage obtainable from the use of an anisotropic ground radiation reflection model seems very small [54].

It is also worthy to have a look at snow as it has a very high albedo and it covers ground for a long period of time in Canada. K. Stamnes stated that snow doesn't give specular reflection neither [55]. The paper also proved a Lambertian reflectivity for naturally formed snow surface. They also measured shoveled snow, and observed that the reflection is flat over all observation angles [56] , [57]. Veverka et al. also confirmed that snow albedo is quasi-Lambertian [58].

2.2.1.2 Papers for anisotropic modeling

There are also a few papers stated that the anisotropy of reflection is important to the outputs.

Eaton pointed out that for those ordinary ground/land surface features in general, the reflection anisotropy is high when incident angle is less than 30°. Predominant forward scattering was observed at mostly level surfaces (e.g. snow alkali and salt flats), while back scatter mainly occurred at surfaces with vertical structuring (plowed fields and vegetated surfaces) [59].

Taylor et al. concluded from their measurements that the land surface exhibits higher backward reflection for Solar Zenith Angles (SZA) less than about 50°; all of the surfaces in this study become more specular as SZA increases [60].

Dickenson gave a formula for overall albedo value vs incident angle as below [61]: $\rho_2 = \rho_0 \frac{1+\Phi}{1+2\Phi\cos(\beta_S)}$, where $\rho_0 = 0.23$ is the albedo value at a solar elevation of 60°; β_S is solar elevation angle, complementary to its zenith angle. Φ is the site dependent factor and equals 0.1 for urban site.

Kimes and Sellers stated that, in some cases, it may give up to 45% error when using Lambertian reflection to replace real reflection patterns [62].

For the total overall albedo, Gueymard et al. gave a detailed discussion, and suggested the average albedo to be 27% instead of 20% where winter snow playing a significant role in such higher value of albedo. They confirmed the importance of correct measurement and estimation of the ground-reflected irradiance [63].

As for snow, it is also observed by Choudhury et al. that glittering of snow increases albedo, and albedo increases further when snow grains become faceted [64]. Painter et al. also observed in remote sensing that snow anisotropy can introduce up to 20% overestimation of snow coverage in forward reflection angles and -15% in backward reflection angles [65].

Gueymard suggested a way of modeling for reflectors with only diffuse but without specular reflection. It is proposed to deal with low anisotropic situations, which are mostly the case for ground reflection a solar panel may encounter, as specular reflection mainly happens on metal, ice and calm water surfaces. The model distinguishes between the reflectance for beam and diffuse radiation. It assumes the reflection of sky diffuse light is isotropic, while the reflection of sun beam is considered as anisotropic with a directional component [34].

Further, for reducing modeling calculation, they simplified the anisotropy of the reflected radiance as an ellipsoidal pattern in each half hemisphere (Figure 14).

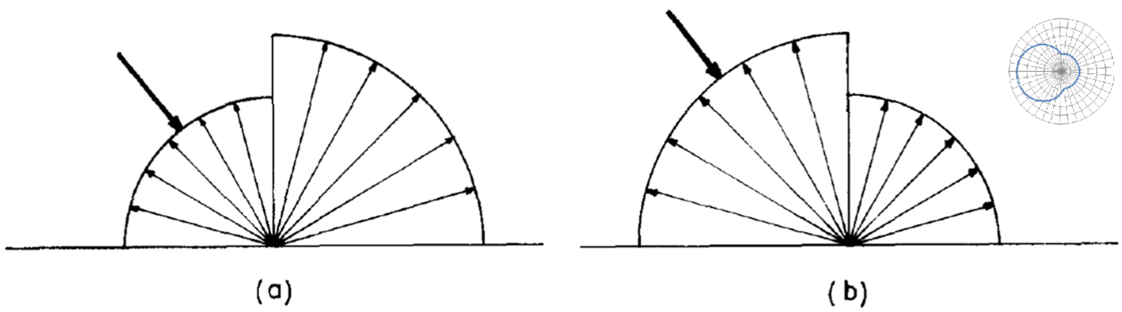

Figure 14 Simplified forward (a) and backward (b) directional reflection in Gueymard's albedo model, insert in up-right corner is the top-view of (b) [34]

2.2.2 Determining model selection

Since our project is about bi-facial, and the side opposite to the sun receives sky diffuse light and ground reflection only. This requires to model albedo in more details and accuracy, especially for justifying improvement of bifacial to mono-facial.

Gueymard's model deals with directional reflection, and gives a set of numerical data for typical ground types, most suitable to our needs. This simple model has been verified by Psiloglou et al. They stated that the model gives better results than isotropic models as well as another anisotropic model, and as a general model, it usually gives a good fit in the validation period and its performance is comparable with that of their new site-specific models [66]. The model is also commented and recommended in the textbook of "Solar Radiation and Daylight Models" in 2004 [67].

Based on previous discussion and balancing the output accuracy vs. model complexity, Gueymard model is chosen for sun beam reflection model.

As for the sky diffuse radiance, since it comes from all direction of the sky, the directional component in reflection may wash out. To simplify calculation, this project will only consider directional reflection for beam incidence, and Lambertian reflection for diffuse radiance.

2.3 Solar cell and panel modeling

As discussed in literature review, bifacial solar cells receive radiation from both front and rear sides, and usually the semiconductor cell cross-sectional structure, including two junctions, is not symmetric. However, researches confirmed that the output current under bifacial illumination is simply the sum of currents generated from both sides for any diode-type solar cells, and the classical circuit model of PV cells may be used for both sides [68]. These conclusions allow taking front and rear side into consideration together in a simple way.

The bifacial solar cells are working under the condition with no concentration, and the maximum irradiance may be 2 suns, one-diode model is sufficient and is to be used in this project for the solar cell modeling.

Other aspects to be considered are the conversion from photonic irradiance power into electrical power; and solar cell working temperature issue. These will be discussed and described in details in corresponding section 3.7 .

Chapter 3 Mathematical modelling and Simulation Algorithm of the project

3.1 Model design considerations and simplifications

1. The model simplifies as the ground albedo does not have retro-impact on sky diffuse light.
2. Reflection from panels and their racking is also neglected, and the justification is given in section 3.7 .
3. Assume no internal reflection at the inner interfaces within panel module.
4. No spectrum variation, instead simply assuming AM 1.5 standard spectrums at different level of intensity, and also, one refractive index for one material in the panel module. For simplification, it is also modeled this way for ground reflections (such as of grass).
5. The ground is simplified as flat extends to infinite, with summer as grass/turf and winter as half grass, half snow. The albedo of snow is simplifies as intermediate in value of 0.6 (0.4 for old snow and 0.8 for fresh snow) [69].
6. The temperature at any given time is simplified as identical all over the solar panel.
7. The panel is 6 mm thick but in the model is simplified as no thickness.
8. The where-about of junction box is to be determined but should be outside of either front or rear panel surface. Therefore, it is not modeled yet.

It will be explained in context, should there be other simplifications.

3.2 Sky diffuse radiance modeling

3.2.1 Models with continuously changing sky diffuse radiance

Perez model uses the same sky clearness ε as in their earlier 3-section sky model to categorize sky conditions as well as the sky brightness Δ [33]. Then the relative luminance (or radiance) is introduced as:

$$f(Z_{Sp},\chi) = [1 + \mathrm{a} \bullet \exp(\frac{b}{\cos Z_{Sp}})] \bullet [1 + \mathrm{c} \bullet \exp(d \bullet \chi) + \mathrm{e} \bullet \cos^2 \chi] \tag{3.1}$$

where Z_{Sp} is the zenith angle of the considered sky element and χ is the angle between this sky element and the position of the sun given by eq. (2.15). The coefficients *a*, *b*, *c*, *d*, and *e* are adjustable coefficients, functions of insolation conditions taking the form of:

$$a(\varepsilon) = a_1(\varepsilon) + a_2(\varepsilon)Z_S + \Delta[a_3(\varepsilon) + a_4(\varepsilon)Z_S]$$

$$b(\varepsilon) = b_1(\varepsilon) + b_2(\varepsilon)Z_S + \Delta[b_3(\varepsilon) + b_4(\varepsilon)Z_S]$$

$$c(\varepsilon) = c_1(\varepsilon) + c_2(\varepsilon)Z_S + \Delta[c_3(\varepsilon) + c_4(\varepsilon)Z_S]$$

$$d(\varepsilon) = d_1(\varepsilon) + d_2(\varepsilon)Z_S + \Delta[d_3(\varepsilon) + d_4(\varepsilon)Z_S]$$

$$e(\varepsilon) = e_1(\varepsilon) + e_2(\varepsilon)Z_S + \Delta[e_3(\varepsilon) + e_4(\varepsilon)Z_S]$$

Except when $\varepsilon = 1$, i.e. the sky is overcast, where

$c(\varepsilon = 1) = e^{[\Delta(\mathrm{c}_1 + \mathrm{c}_2 Z_\mathrm{S})]^{\mathrm{c}3}} - c_4$, and $d(\varepsilon = 1) = -e^{\Delta(d_1 + d_2 Z_S)} + (d_3 + \Delta d_4)$.

The corresponding set of the parameter values are tabulated in Appendix A .

Therefore, the relative distribution of diffuse radiance over the sky dome may be expressed as:

$$L_{Sp} = f(Z_{Sp}, \chi) = [1 + \mathrm{a} \bullet \exp(\frac{b}{\cos Z_{Sp}})] \bullet [1 + \mathrm{c} \bullet \exp(d \bullet \chi) + \mathrm{e} \bullet \cos^2 \chi] \qquad (3.2)$$

Since *DHI* is a sum of contribution from all over the sky, and the above is merely a distribution, this sum is named as a preparatory DHI:

$$DHI_{Prep} = \sum_i \frac{L_{Sp.i}\,\mathrm{A}_{\mathrm{Sp.i}} \cos(Z_{Sp.i})}{2\pi} = \sum_i \frac{[1 + \mathrm{a} \bullet \exp(\frac{b}{\cos Z_{Sp.i}})] \bullet [1 + \mathrm{c} \bullet \exp(d \bullet \chi_i) + \mathrm{e} \bullet \cos^2 \chi_i]\,\mathrm{A}_{\mathrm{Sp.i}} \cos(Z_{Sp.i})}{2\pi} \qquad (3.3)$$

On the other hand, in this project, the real DHI value is known from measurement. A ratio can be taken as a normalization factor:

$$f_{NormDHI} = DHI_{Measured} / DHI_{Prep} \tag{3.4}$$

Follow suit, the actual radiance on sky dome may be obtained from: $L_{SpActual} = L_{Sp} \times f_{NormDHI}$, hence the actual radiance anywhere on sky dome in details is given as:

$$L_{SpActual.j} = \frac{2\pi[1+\mathrm{a}\bullet\exp(\frac{b}{\cos Z_{Sp.j}})]\bullet[1+\mathrm{c}\bullet\exp(d\bullet\chi_j)+\mathrm{e}\bullet\cos^2\chi_j]\bullet DHI_{Measured}}{\sum_i[1+\mathrm{a}\bullet\exp(\frac{b}{\cos Z_{Sp.i}})]\bullet[1+\mathrm{c}\bullet\exp(d\bullet\chi_i)+\mathrm{e}\bullet\cos^2\chi_i]\,\mathrm{A}_{\mathrm{Sp.i}}\cos(Z_{Sp.i})} \tag{3.5}$$

This way, the diffuse distribution over the sky dome is maintained, while all the sky dome radiance received on ground will be summed up to be exactly the measured DHI.

As discussed in literature review above, the distribution of diffuse irradiance over the sky dome is continuous and gradually varying, and is expected to be the closest to the reality, thus gives the best simulation results. Then, comparing CIE model and Perez's 1993 continuous distributive model, Perez model is chosen in this project as it is simpler in calculation and gives a very good result and even better than CIE model.

3.2.2 The approximation of sky diffuse distribution in this simulation

In this simulation, the sky dome is modelled as a hemisphere with a normalized unit radius, and indicates all the sky patches as in infinite by treating rays from the same sky patch as parallel lines. Because of the normalized unit radius, the sky patch area in the calculation becomes simply its solid angle. The sky dome is further divided into patches, with divisions in azimuth and elevation (Figure 15). The density of patching vs. simulation accuracy will be discussed in section 3.5 .

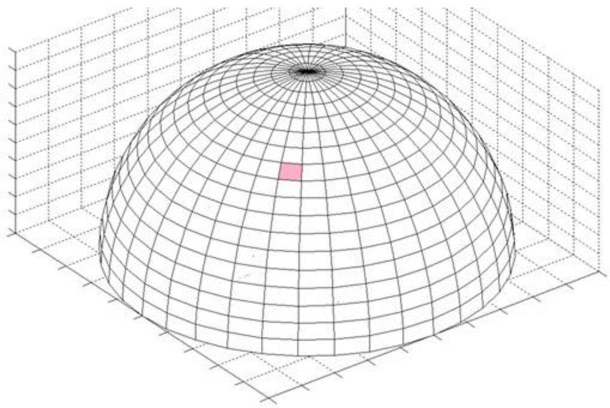

Figure 15 Sky dome division in simulation

Each patch is assumed small enough, and all the values over the patch are represented by the values at its center of mass. By assigning values to sky patch centers using eq.(3.5), a sky diffuse distribution can be obtained (Figure 16).

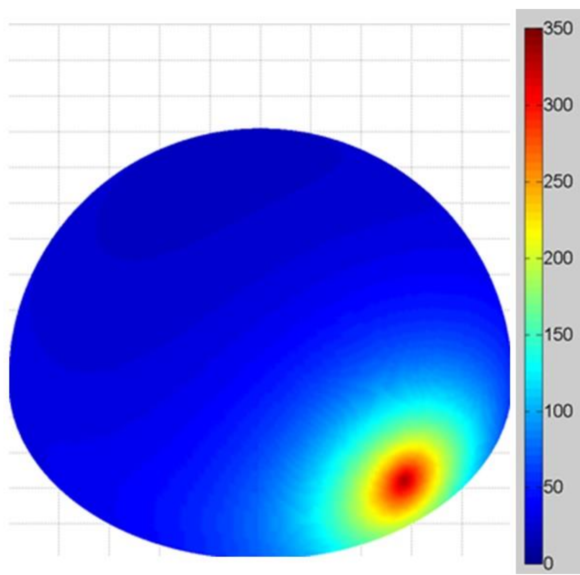

Figure 16 Sky diffuse radiance distribution at 9:30 AM, Jan. 1, 1966 with DNI = 830 W/m^2, and DHI = 98 W/m^2 from Ottawa Int'l Airport TMY Dataset

It needs to point out that Perez's model works only when the sun is above horizon. When there is sky diffuse radiance (non-zero DHI) before sunrise or after sunset, although the sky at such times are usually much brighter on the half to the sun, however, since the amount of DHI is very small, and a greater radiance on either east or west side actually does not change the irradiance on the ground or the panel, we simplify the sky diffuse as isotropic distribution for easy calculation without any significant impact on the total output.

3.3 Gueymard's reflection model

This section only gives the basic explanation and resulted formulas for modeling, and please refer to Appendix B for detailed description and derivation.

3.3.1 Reflectance to a beam of any incidence angle in Gueymard's model

Gueymard et al. defined a few reflectance indices:

ρ : usually reported mean daily albedo;

ρ_d : diffuse reflectance, which is "almost" equal to ρ ;

ρ_n : reflectance to a normal incidence beam, assumed pure isotropic;

ρ_b : reflectance to a beam of any incidence angle.

Based on their reflection model, an expression of directional albedo for general beam reflectance is shown below:

$$\rho_b = [\rho_d - 0.023(\mathrm{f}_{ab} + \mathrm{f}_{af})] + [\delta_\gamma\, \mathrm{f}_{\mathrm{af}} + (1-\delta_\gamma)\, \mathrm{f}_{\mathrm{ab}}] \cos\left\{\arcsin\left[\cos(\beta)\sin(\gamma)\right]\right\} \mathrm{e}^{-1.77-1.53(\frac{\beta_S}{100})-3.61(\frac{\beta_S}{100})^2} \tag{3.6}$$

Where ρ_d is let equal to mean albedo ρ , and the value of ρ or ρ_d varies for different ground types; γ is the horizontal angle between incidence and reflection; β is the elevation angle of a reflection ray; f_{ab} and f_{af} are anisotropic reflection backward and forward factors also varying for ground types; for $[\delta_\gamma\, \mathrm{f}_{\mathrm{af}} + (1-\delta_\gamma)\, \mathrm{f}_{\mathrm{ab}}]$, where $\delta_\gamma = 1$ if $\cos\gamma > 0$, and $\delta_\gamma = 0$ otherwise, and the values of f_{ab} and f_{af} ; and β_S is the source (the sun) elevation angle in *degree*.

3.3.2 Power-wise analysis for reflection for Gueymard's model

The sun beam radiant flux reflected by a ground patch and reaches a panel patch may be expressed as:

$$\Phi(\mathrm{Z_r}) = \frac{[\rho_d - 0.023(\mathrm{f}_{ab} + \mathrm{f}_{af})] + [\delta_\gamma\, \mathrm{f_{af}} + (1-\delta_\gamma)\,\mathrm{f_{ab}}]G(\gamma)\, \mathrm{e}^{-1.77-1.53(\frac{\beta_S}{100})-3.61(\frac{\beta_S}{100})^2}}{\pi} DNI \cos(Z_S) \bullet \Omega_{GpPp}[A_{Pp}\cos(\theta_{GpPp})](\mathrm{W})$$

(3.7)

Where Ω_{GpPp} is the solid angle for a ground patch seen from center of the panel patch, and $A_{Pp}\cos(\theta_{GpPp})$ is the effective panel patch area facing the field ground patch center. Panel front incidence angle θ_{GpPp} may be obtained by first get the reflecting ray's horizontal angle from:

$$\omega_{GpPpH} = \arcsin\left[\frac{y_{Gp} - y_{Pp}}{\sqrt{(y_{Gp} - y_{Pp})^2 + (x_{Gp} - x_{Pp})^2}}\right] \tag{3.8}$$

Where x_{Gp}, y_{Gp} are ground patch central (center of mass) coordinates; and x_{Pp}, y_{Pp} are panel patch center coordinates on horizontal plane.

Since the horizontal angle is acquired from anti-sinusoidal function, the actual direction is to be determined by checking the signs of the difference of the two centres' coordinates. See sub-section 4.4.1 for detailed discussions.

The second step is to obtain the horizontal distance between the ground patch center and the panel patch center based on their x, y coordinates, and the reflecting ray's elevation angle is also known along with the panel patch's height. Notice that the elevation angle of reflecting ray is negative as the ray comes from low to high. Now, the incidence angle can be calculated using eq.(2.6), but with the said negative elevation angle β.

3.3.3 The solid angle of ground patches seen from panel patch

In this model, as sky radiance receiver and reflector, the ground is also divided into patches by divisions in azimuth and radius with regard to the origin (x_O, y_O, z_O) where (x_O, y_O) is set at the bottom central point of the panel under investigation, and z_O is simply set on ground, $z_O = 0$. This model sets 5 panels in a row. The racking structure is set as simple square-cross-sectional vertical posts at each panel corners. The neighboring panels share the racking posts. The posts are assumed blocking radiance without reflection (Figure 17).

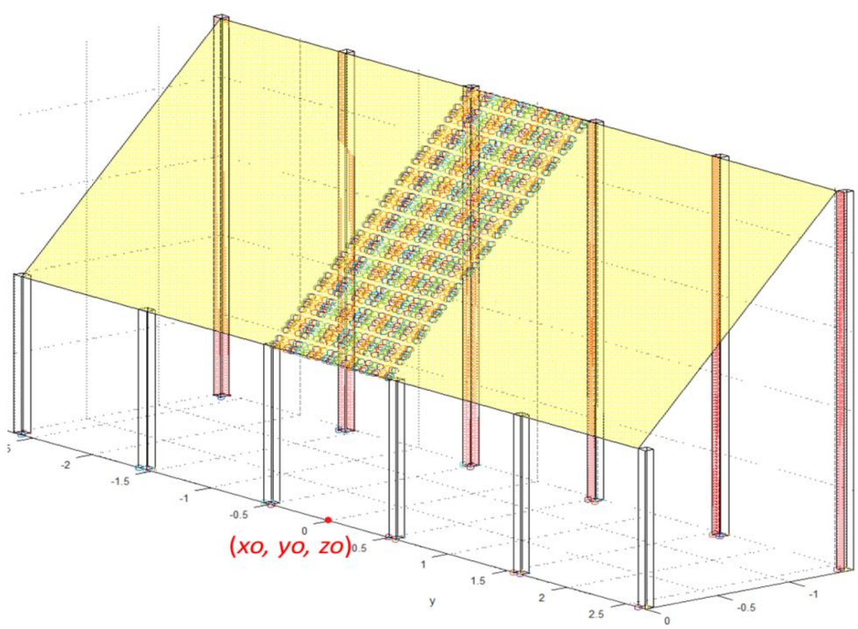

Figure 17 Panels, racking and coordinate origin

The definition of solid angle is: $\Omega = \frac{A}{r^2}(Sr)$, where A is the surface area of the spherical cap, $2\pi rh$; r is the radius of the sphere; h is the height of the cap; and Sr is the unit, steradian.

The solid angle of a far field ground patch and that of a near field patch are calculated differently, please see detailed description in Appendix B .

The radiant flux from the sun and reflected by a far field patch and then received by a panel patch may be expressed as below, and also need to mention that the far-field ground patches are simplified as never be shaded.

$$\Phi(\mathrm{Z_r}) =$$

$$\left\{[\rho_d - 0.023(\mathrm{f}_{ab}+\mathrm{f}_{af})]+[\delta_\gamma\,\mathrm{f_{af}}+(1-\delta_\gamma)\,\mathrm{f_{ab}}]\cos[\arcsin(\cos\beta_r\sin\gamma)]\mathrm{e}^{-1.77-1.53(\frac{\beta_S}{100})-3.61(\frac{\beta_S}{100})^2}\right\} DNI\cos(\mathrm{Z}_S)\bullet\frac{2\sin(\beta_{Gfp.in})}{N_{GpAzD}}[A_{Pp}\cos(\theta_{GfpPp})](\mathrm{W})$$

(3.9)

When the radiant flux is from a sky patch, the reflection is considered Lambertian, the expression is simplified as: $\Phi(\mathrm{Z_r}) = \rho_d \frac{I_{Sp}A_{Sp}\cos(Z_{Sp})}{2\pi}\bullet\frac{2\sin(\beta_{Gfp.in})}{N_{GpAzD}}[A_{Pp}\cos(\theta_{GfpPp})](\mathrm{W})$, and the total reflection from one far field ground patch to a panel patch is the summation of all sky patch irradiances:

$$\Phi(\mathrm{Z_r})_{\mathrm{total}} = \rho_d \frac{2\sin(\beta_{Gfp\bullet in})}{N_{GpAzD}}[A_{Pp}\cos(\theta_{GfpPp})]\bullet\left\{\frac{1}{2\pi}\sum_{i=1}^{skyPatches}[I_{Sp.i}A_{Sp.i}\cos(Z_{Sp.i})]\right\}(\mathrm{W}) \qquad (3.10)$$

The radiant flux from the sun, and reflected by a near field patch and received by a panel patch may be expressed as:

$$\Phi(\mathrm{Z_r}) =$$

$$\left\{[\rho_d - 0.023(\mathrm{f}_{ab}+\mathrm{f}_{af})]+[\delta_\gamma\,\mathrm{f_{af}}+(1-\delta_\gamma)\,\mathrm{f_{ab}}]\cos[\arcsin(\cos\beta_r\sin\gamma)]\mathrm{e}^{-1.77-1.53(\frac{\beta_S}{100})-3.61(\frac{\beta_S}{100})^2}\right\} DNI\cos(\mathrm{Z}_S)\bullet\frac{(\mathrm{d}_2^2-\mathrm{d}_1^2)}{N_{GpAzD}}\bullet\frac{\cos(\mathrm{Z_r})}{D_{GpPp}^2}[A_{Pp}\cos(\theta_{GpPp})](\mathrm{W})$$

(3.11)

When for Lambertian reflection to radiant flux from a sky patch, the expression is simplified as:

$$\Phi(\mathrm{Z_r}) = \rho_d \frac{I_{Sp}A_{Sp}\cos(Z_{Sp})}{2\pi}\bullet\frac{\pi(\mathrm{d}_2^2-\mathrm{d}_1^2)}{N_{GpAzD}}\bullet\frac{\cos(\mathrm{Z_r})}{D_{GpPp}^2}[A_{Pp}\cos(\theta_{GpPp})](\mathrm{W}) \qquad (3.12)$$

If there is no blocking between any sky patch to this near field ground patch, the irradiance on the ground patch is the summation of all sky patch radiant flux, and the total reflection from the near field ground patch to a panel patch is:

$$\Phi(\mathrm{Z_r})_{\mathrm{total}} = \rho_d \frac{(\mathrm{d}_2^2-\mathrm{d}_1^2)}{N_{GpAzD}}\bullet\frac{\cos(\mathrm{Z_r})}{D_{GpPp}^2}[A_{Pp}\cos(\theta_{GpPp})]\left\{\frac{1}{2\pi}\sum_{i=1}^{skyPatches}[I_{Sp.i}A_{Sp.i}\cos(Z_{Sp.i})]\right\}(\mathrm{W}) \qquad (3.13)$$

For radiance from a sky patch toward a near field ground patch, if the ray is blocked by any part of the racking, this ray becomes terminated at the racking as the assumption in this project that the racking does not reflect. If a ray hits the panel on its way from sky toward ground, the ray need to be multiplied by an angular transmission function for two air-glass interfaces, and an area-ratio factor (transparent area/total panel area), this case, only a portion of the ray will reach the ground.

3.4 Panels and Racking Geometry Modeling and Their Shading and Blocking Effects

3.4.1 Shading of sun beam on ground

Figure 18 generated in MATLAB, shows the panel array and racking system, and a sun-beam-only ground shading scenario to help algorithm explanation and description below.

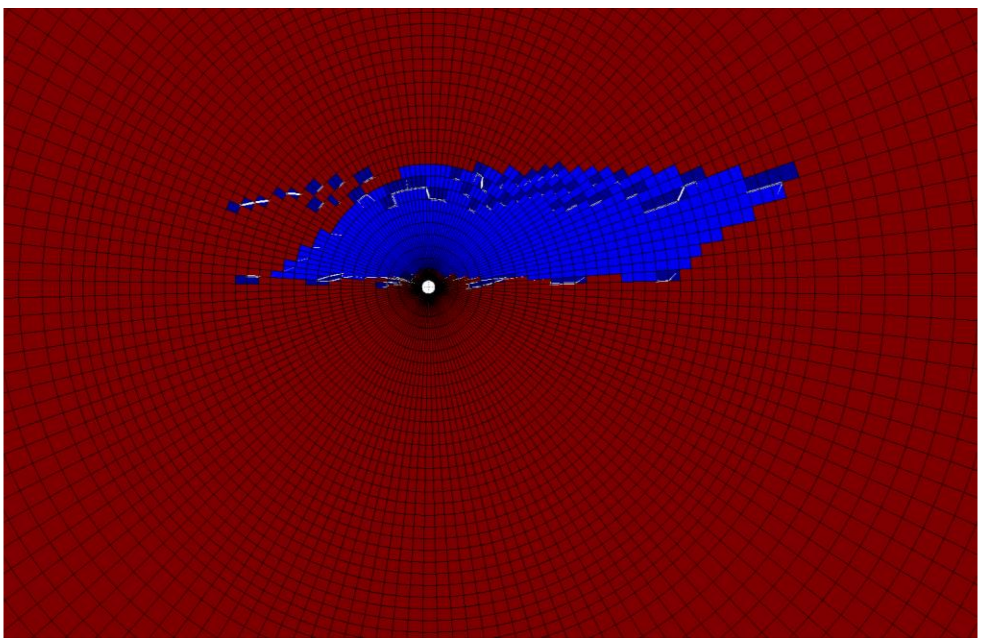

Figure 18 Ground shaded by panel array and racking at 15:30PM, July 10, Ottawa, ON. panel facing south with clearance = 0.5 meter (right of the figure is to the east)

3.4.1.1 Posts blocking sun beam on ground

Firstly, the position of the sun, its azimuth angle φ_S and elevation angle β_S determine the direction of the beam, and the coordinates of the center of mass of the ground patch (x_{Gp}, y_{Gp}) determines a point on the beam. Therefore, the line function for the ray can be generated as:

$$\frac{x - x_{Gp}}{\cos(\beta_S)\cos(\varphi_S)} = \frac{y - y_{Gp}}{\cos(\beta_S)\sin(\varphi_S)} = \frac{z}{\sin(\beta_S)} \qquad (3.14)$$

Any side of a post is on a vertical plane defined by coordinates of any 3 points on this side. As long as the beam is not parallel to the post-side plane, the intersection point can be obtained. Then checking if this point is within the narrow rectangular area representing the post-side determines if this beam is blocked by this post-side. Checking through all the post-sides if the beam is blocked by any of the post-side.

3.4.1.2 Panel shading sun beam on ground

The panel shading on the ground is checked a very similar manner. However, there are two differences.

Firstly, the panels can be set at any tilting angle and there is a clearance. A plane containing the panels is generated first, and then use the same beam-to-ground-patch-center line formula to obtain the intersection point on the plane, check if this point is between the bottom and the top heights of the panels, if yes, then check if the point is between the two sides of the panels at the intersection height.

Secondly, the panel is considered transparent in the gaps between solar cells. Therefore, even the sun beam reaches the panel before ground, the ground still receives a portion of the irradiance. Details of this transmission filtering is discussed in section 3.6.2.1 .

3.4.2 Panel Posts Block Sun Beam on Panel Rear Side

Based on the geometry of the model, there is no shading or blocking on panel front side. Nevertheless, when the sun is shining on the rear side, the taller posts block sun beam and cast shade on the rear side.

The racking is designed as shown in Figure 17. When beam comes from the sun, only those taller posts block beam on the panel rear side.

The blocking checking algorithm is very similar to racking blocking of sun beam to ground, except the receiving plane is the panel with a tilting angle, and azimuth angle. Therefore, the function of ray should include the 3-D coordinates of panel patches $\frac{x - x_{Pp}}{\cos(\beta_S)\cos(\varphi_S)} = \frac{y - y_{Pp}}{\cos(\beta_S)\sin(\varphi_S)} = \frac{z - z_{Pp}}{\sin(\beta_S)}$, where (x_{Pp}, y_{Pp}, z_{Pp}) is the 3-D coordinates of the panel patch center. Figure 19 is an example of the resulted shading plot from the simulation.

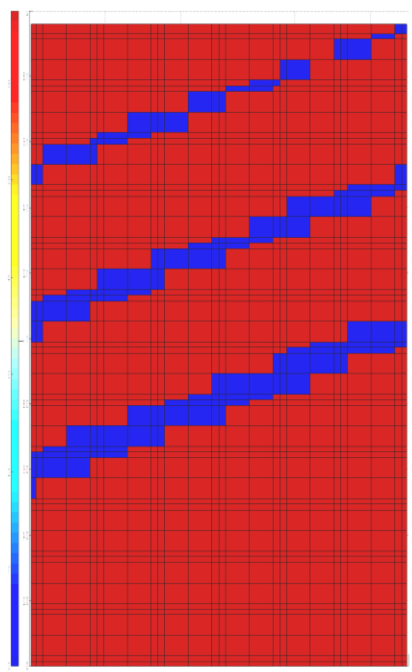

Figure 19 Three tall posts to the east shading on panel rear side at 5:30AM, June 21, Ottawa, ON. with panel tilt = 45.32°, South facing, clearance = 1 meter (right of the figure is on east)

3.4.3 Panel and Racking Shading of Sky Diffuse Radiance to Ground

Figure 20 shows the panel array and racking system, and a general shading scenario under isotropic sky diffuse radiance (a heavily overcast sky may generate a scene very close to this) to help algorithm explanation and description below.

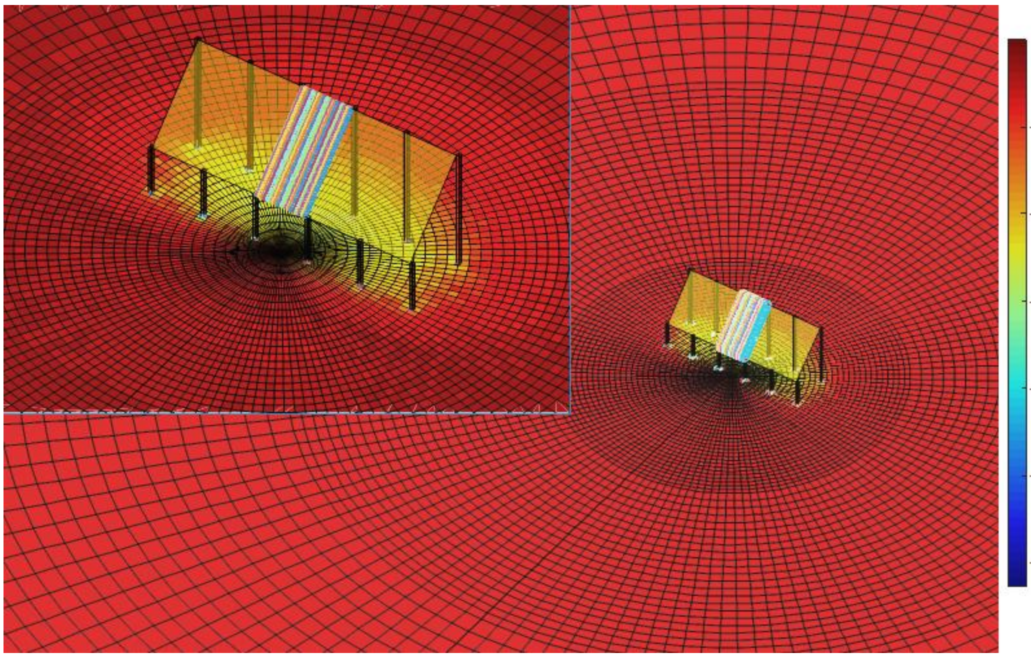

Figure 20 Five panels, racking on shaded field with middle panel under investigation (darkish red area further away from panels takes the highest value, i.e. not shaded)

The sky dome is divided in patches which are considered small enough that they are represented by their center of mass. Hence, geometrically, they are also considered as point source.

Therefore, the checking algorithm of shading and blocking for a sky patch is the same as for the sun. The representing point of a sky patch is the center of mass of the sky patch. Such center determines the azimuth angle φ_{Sp} and elevation angle β_{Sp} of the ray. Therefore, the line function for the ray can be generated same as for the sun beam to the ground. Panel shading of sky diffuse radiance on ground takes parallel similarity. The final shading and blocking of the whole sky diffuse radiance on a ground patch is of course the sum up through all the sky patches. A four-dimensional matrix is generated this way containing block and shade information of all sky patches to all ground patches.

3.4.4 Determining the "viewing" relation between sky patches and the two sides of panel

when β_{Sp} and φ_{Sp} are given as the elevation and azimuth angles of the sky patch center of mass, the incidence angle θ_{SpPf} from a sky patch toward the panel front side can be obtained same as beam incidence angle using eq.(2.6).

A sky patch can be seen from panel front side if $\theta_{SpPf} < 90°$, and cannot been seen by neither front or rear side if it is 90°, otherwise be seen by the rear side.

3.4.5 Panel Posts Block Sky Diffuse Radiance on Panel Rear Side

The blocking checking algorithm is very similar to racking blocking of sky to ground, except the receiving plane is the panel with a tilting angle. Therefore, the function of ray should include the 3-D coordinates of panel patches $\frac{x - x_{Pp}}{\cos(\beta_{Sp})\cos(\varphi_{Sp})} = \frac{y - y_{Pp}}{\cos(\beta_{Sp})\sin(\varphi_{Sp})} = \frac{z - z_{Pp}}{\sin(\beta_{Sp})}$, where (x_{Pp}, y_{Pp}, z_{Pp}) is the 3-D coordinates of the panel patch center.

Same as the blocking of sun beam on panel rear side described in sub-section 3.4.2 , if the sky patch can be seen in the rear side, its rays can be checked over the panel rear patches, and a four-dimensional matrix of the blocking information is generated.

3.4.6 Ground reflection to panel front and rear sides

There is also a viewing factor between ground and panel. Similar as that between sky and panel discussed above, any of the ground patches is also seen by one side of the panel only. If θ_{GpPf} is the incidence angle of the reflected ray from a center of mass of a ground patch to a panel front side, and $\theta_{GpPf} < 90°$, then the ground patch is faced by panel front side, and not be seen by neither side if it is 90°. Otherwise, it is faced by panel rear side. The incidence angle from a ground patch toward the panel front side can be obtained using the method described in sub-section 3.3.2 . Since the reflection is always from ground to a panel patch above, the ground to panel elevation angle takes negative value in this incidence angle calculation, but notice that it takes positive value in solid angle calculation in sub-section 3.3.3 .

3.5 Simulation errors, their compensation and reduction

3.5.1 Identifying Main Errors – in the ground to panel reflection

When a whole surface is divided into patches, and patches are represented by their geometric centers, errors are brought about. Some of the errors are negligible, but some are not.

In this project simulation, panel patches are very small in size, and furthermore, a few patches are to be grouped to be a solar cell in final electrical power output calculation, this will further cancel out small variations, therefore, errors are not significant.

For the sky dome, since all the rays from a sky patch are in parallel, the error may only come from the concentration of a sized patch into a representing geometric central point. The sky dome patching error is checked as a normalized isotropic sky should give a normalized DHI of value π, indeed, when patched as 18 and 5 divisions, it gives 3.151, which is only 0.3% greater than π, which is negligible. Higher resolutions give an even smaller error.

However, the comparatively greatest error happens in the calculation of reflection from ground patches toward panel patches. The reasons are: the ground patches are shaped as annular sectors, and such shape is seen distorted from a panel patch. The closer the ground patch sector to a panel patch, the greater the distortion. This distortion not only changes its solid angle seen from a panel patch, but also changes the representativeness of using the annular sector geometric center in calculating the distance between the ground patch and the panel patch.

When the ground is assumed Lambertian albedo, and there is no shading, the theoretical reflection received on a panel patch is an integral of reflection over the ground onto a panel patch: they are $\pi\rho\left(\frac{1-\cos\Sigma_P}{2}\right)$ and $\pi\rho\left(\frac{1+\cos\Sigma_P}{2}\right)$ for front or rear panel patch respectively. An error exists when the reflection sum up over all the ground patches onto a panel patch differs from the theoretical value. Obviously, such error is contributed by all the ground patches. Due to the complexity of the distorted shapes, it will be extremely complicated if we are to find out each individual ground patch's contribution to the error.

3.5.2 Error compensation for isotropic (Lambertian) reflection

To compensate the error, a ratio of the sum up to the theoretical value is obtained:

$$f_{GpPpfComp} = \frac{\pi\rho\left(\frac{1-\cos\Sigma_P}{2}\right)}{\rho\sum_i\left[\Omega_{GpPpf.i}\bullet\cos(\theta_{GpPpf.i})\right]} = \frac{\pi\left(\frac{1-\cos\Sigma_P}{2}\right)}{\sum_i\left[\Omega_{GpPpf.i}\bullet\cos(\theta_{GpPpf.i})\right]}$$ for front side, and

$$f_{GpPprComp} = \frac{\pi\left(\frac{1+\cos\Sigma_P}{2}\right)}{\sum_i\left[\Omega_{GpPpr.i}\bullet\cos(\theta_{GpPpr.i})\right]}$$ for rear side.

The compensation above is in fact to assume that each ground patch contributes to the error proportionally to its share in the sum-up $\sum_i\left[\Omega_{GpPpr.i}\bullet\cos(\theta_{GpPpr.i})\right]$, which is based the mathematical concept of the "best unbiased estimation".

Since each panel patch on each side has an individual compensation factor, there will be two 2-dimensional matrices for the two panel sides (Figure 21, and Figure 22). Although these compensation matrices are obtained under isotropic ground brightness condition, since these compensations are purely geometrical, they can be applied to any ground brightness distribution including scenarios when ground patches are shaded, or blocked. In Figure 23, it is the rear side normalized reflection being shaded by posts, and the compensation same as that in Figure 22. It can be seen that the artificial effect, on the left plot due to ground patch size, disappeared on the right plot after same compensation, and provides a perfect distribution.

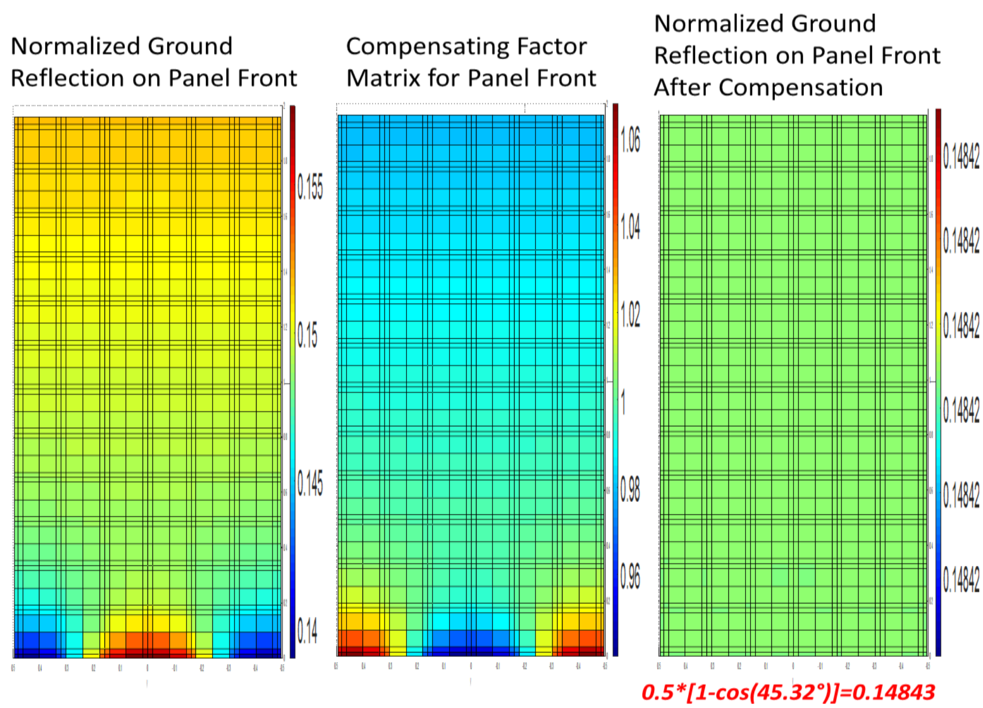

Figure 21 Normalized Isotropic Ground Reflection on Panel Front Side, Its Error by Numerical Sum-Up and Compensation, Due South, Σ_P=45.32°, Clearance=0.2 meters

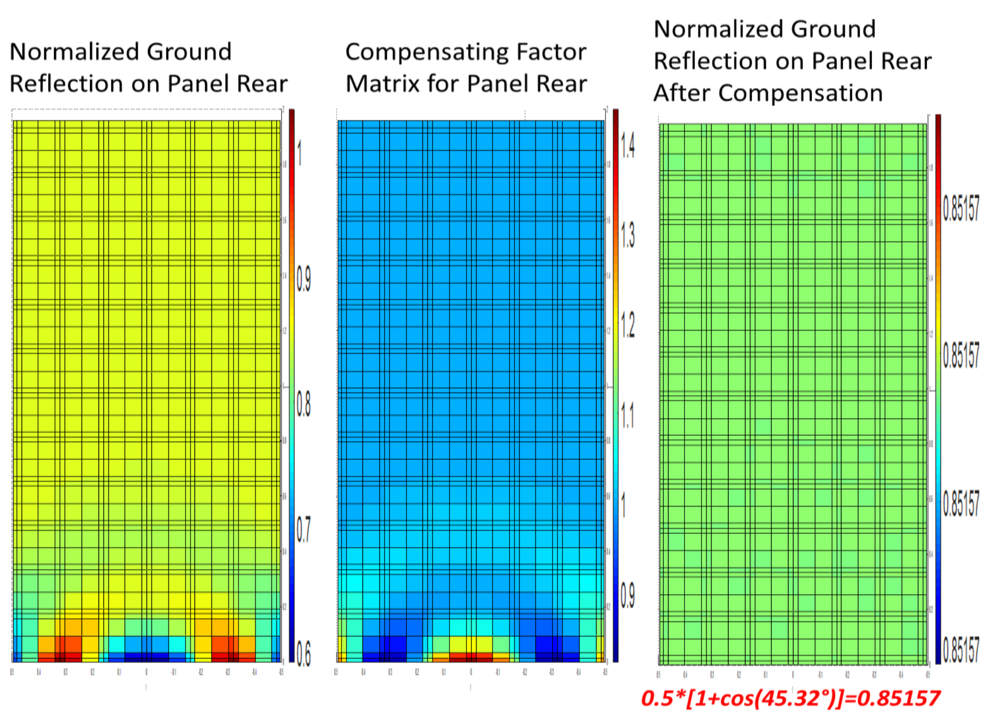

Figure 22 Normalized Isotropic Ground Reflection on Panel Rear Side, Its Error by Numerical Sum-Up and Compensation, Due South, Σ_P =45.32°, Clearance=0.2 meters

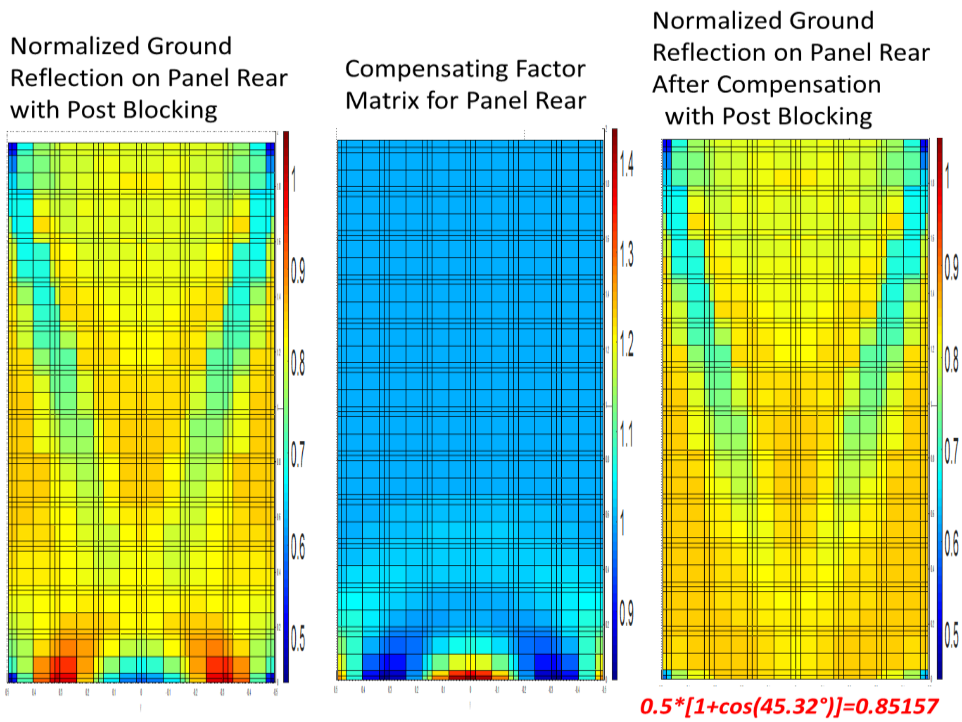

Figure 23 Normalized Isotropic Ground Reflection on Panel Rear Side with Blocking, Its Error by Numerical Sum-Up and Compensation, Due South, Σ_P =45.32°, Clearance=0.2 meters

3.5.3 Further reduction for remained error in directional component of reflection of sun beam

Such compensation works perfectly for Lambertian reflection. However, when reflection is not Lambertian, there is a small amount remnant error even after the compensation.

From Gueymard's model, the directional reflection received at any panel patch is an integral over the ground region seen at this panel patch of this side. However, the integral can only be done numerically, and is complicated to obtain and takes a long computation time.

On the other hand, after the above compensation, the distributions on both sides of the panel have only a very small portion near the panel bottom. Averaging the distributions over each side of the panel should give very good results, which will be checked and proved once the model is built (please see sub-section 5.1.3).

3.6 Panel optical transmission modeling

3.6.1 Sunpreme ® solar panel

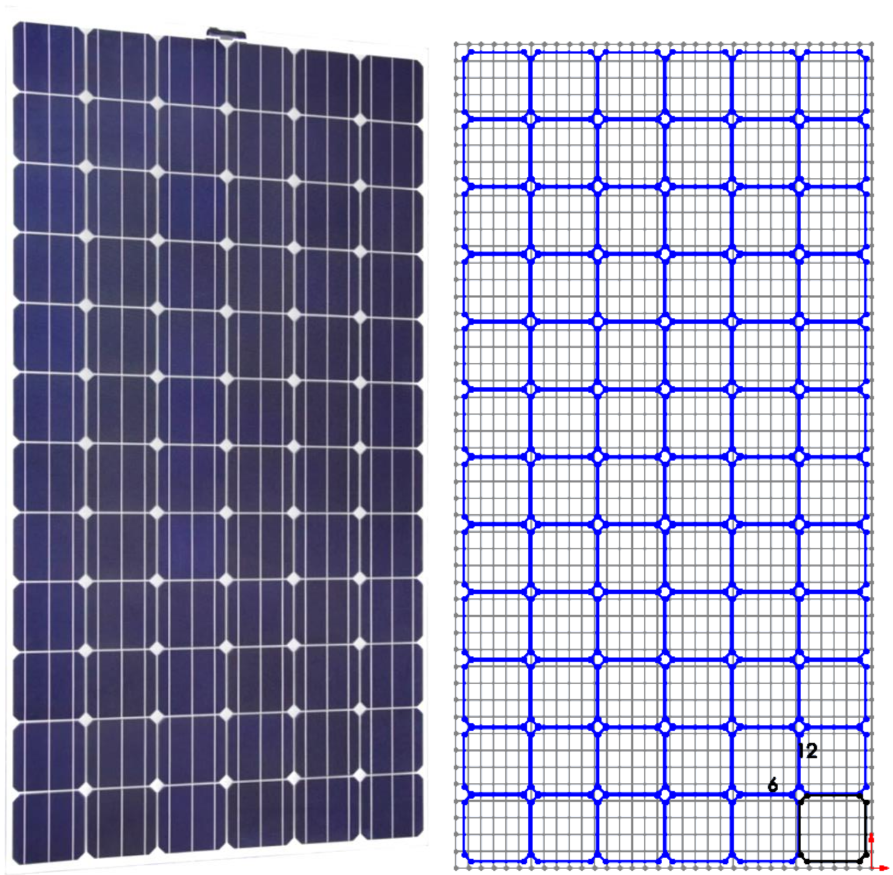

Figure 24 the solar cell layer out of the panel under investigation [70]

The solar panel in this project is from Sunpreme ® and is 1960mm×990mm in size, with 72 solar cells arranged as 12 rows by 6 columns. The between-cell-gaps ending at the long edges are 3mm in width, and the gaps ending at the long edges are 4mm in width. The remained space becomes the panel edges. The edge on panel top is 30 mm wide, at bottom 16mm, and 14.75mm on each side (Figure 24) [70].

The solar cell is a PNN+ type bifacial solar cell. It consists of a P-type amorphous Silicon (a-Si) at the top, with an intrinsic a-Si layer connects it to the N-type Cubic Zirconia base, and another layer of intrinsic a-Si under the base connecting to an N-type a-Si as the bottom layer, as well as

Indium-Tin-Oxide (ITO) anti-reflection coating and then fingers and bus bars on top and bottom side of the cell (upper part in Figure 25) [71].

The solar cell physical size is 156.75mm by 156.75mm with 16mm-legged cut-offs at four corners. There are 3 bus bars on each of the front and rear side, and 92 fingers on the front side, but up to 200 fingers on the rear side to increase the electrical performance [71]. The bus bars and fingers cover 8.6% and 15.3% of solar cell areas on front and rear sides respectively.

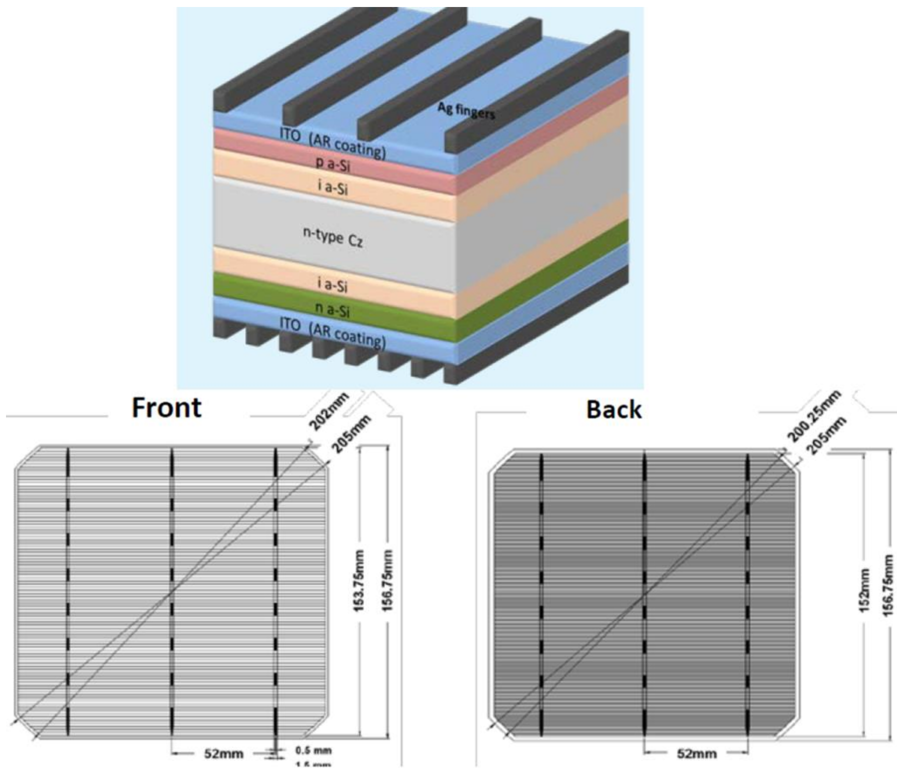

Figure 25 Solar cell front and rear side bus bars and fingers [71]

All the irradiance and power on panel patches are to be merged into irradiance and power on each solar cell. To make the conversion easier, the panel is patched in a varying-sized manner to match the solar cell period (Figure 26).

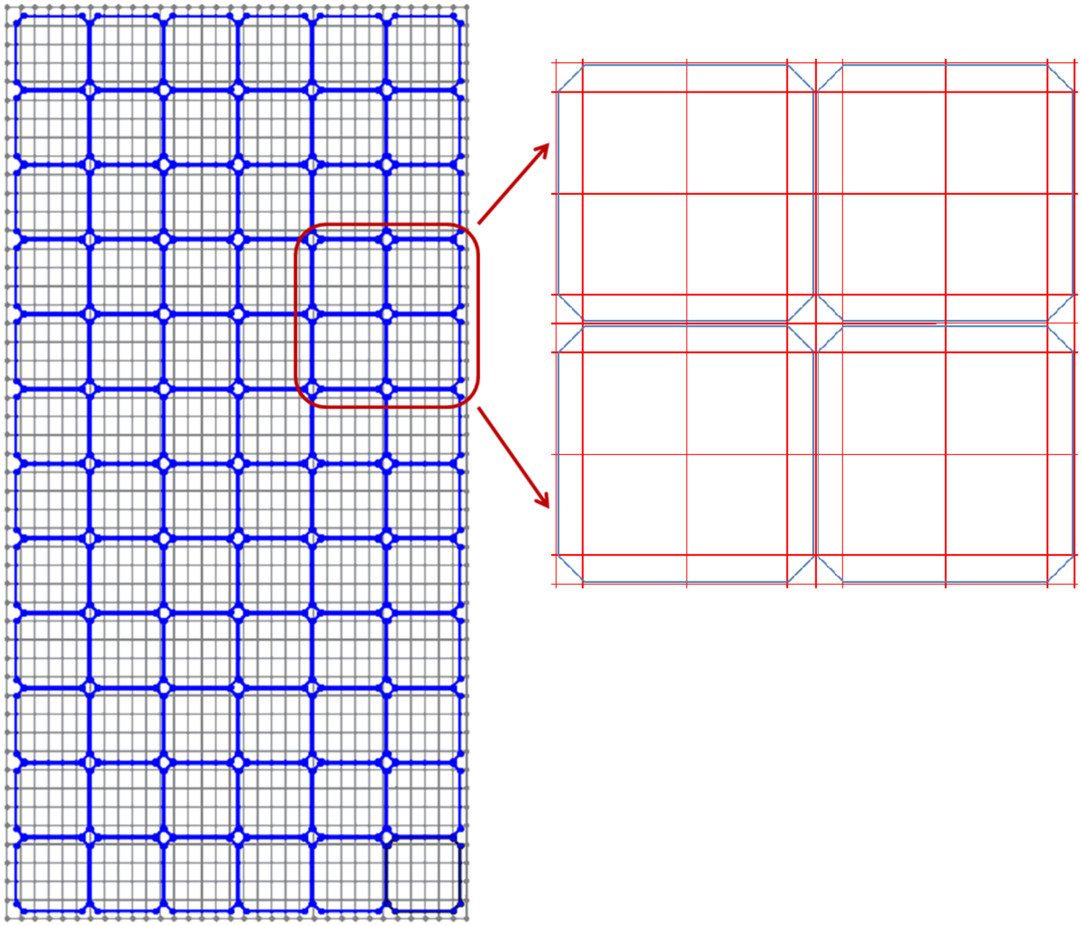

Figure 26 The periodically varying-sized panel patching to make patch-to-solar cell irradiance conversion calculation easier

3.6.2 Panel optical transmission modeling

There are two types of transmission to discuss in this section: the optical transmission of panel shading on ground; and incident irradiance transmitting through the panel and entering into solar cell silicon layer.

The model neglects internal secondary reflections within the panel structure.

3.6.2.1 Panel optical transmission modeling for panel shading

Not like post blocking. Panel shading allows a certain fraction of the incidence irradiance passing through to reach ground (Figure 27).

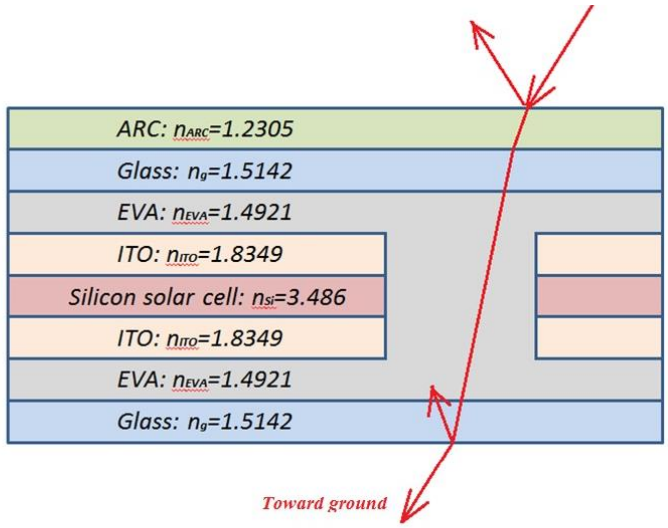

Figure 27 Transmission of incidence passing through panel toward ground

The model simplifies the panel shading as a transparency of the panel: the solar cells block all radiance while edges and between-cell-gaps allow irradiance to pass through. This gives a filtering relating to an area ratio: $f_{PT} = \frac{(A_P - n_{Sc} \bullet A_{Pp})}{A_P}$, where A_P is the total panel area, $n_{Sc} \bullet A_{Pp}$ is the area covered by solar cells.

In these edge and gap areas where there is no solar cell, and EVA has a refraction index very close to that of glass, therefore, the model simplifies the panel as glass with ARC layer on the top. The three interfaces reflect irradiance, and the model further neglects the multi-reflection within the glass as these multi-reflections are very small fraction of the total incidence. Applying Fresnel equation to a radiation of any incidence angle passing through these interfaces gives a transmittance of the panel, $T(\theta) = \prod_{i=1}^{N}[1 - \mathrm{R}_i(\theta_i)]$, where N is the number of interfaces, θ_i is the incidence angle at each interface, $\mathrm{R}_i(\theta_i)$ is the reflectance on each interface with such incidence angle.

The product of these two factors gives the fraction of radiance power passing through panel towards ground. $T_P(\theta) = f_{PT} \bullet T(\theta)$. This fraction is applicable to both sun beam and sky diffuse radiance passing through panel toward ground.

3.6.2.2 Panel optical transmission modeling for solar cell receiving power

Based on the panel's Incidence Angle Modifier (IAM) curve (normalized curve) provided by Celestica (Figure 28), the optical transmission is modeled as: the optical power entered solar cell Silicon layer as a product of irradiance reaching the air-glass surface, transmittance at normal incidence, IAM, cos(θ), and the cell area at each panel patch. $T_{Pf}(\theta)$, and $T_{Pr}(\theta)$ for front and rear side respectively: $T_{Pf}(\theta) = T_{PfN} \bullet IAM(\theta_{Pf}) \bullet \cos(\theta_{Pf})$, and $T_{Pr}(\theta) = T_{PrN} \bullet IAM(\theta_{Pr}) \bullet \cos(\theta_{Pr})$.

Where T_{PfN} is transmittance at normal incidence on front side, and T_{PrN} for rear side. Due to less of one ARC layer on the air-glass interface, the rear side transmittance at normal incidence T_{PrN} is slightly lower than that on the front side. The IAM curve is used for both sides as the difference is negligible.

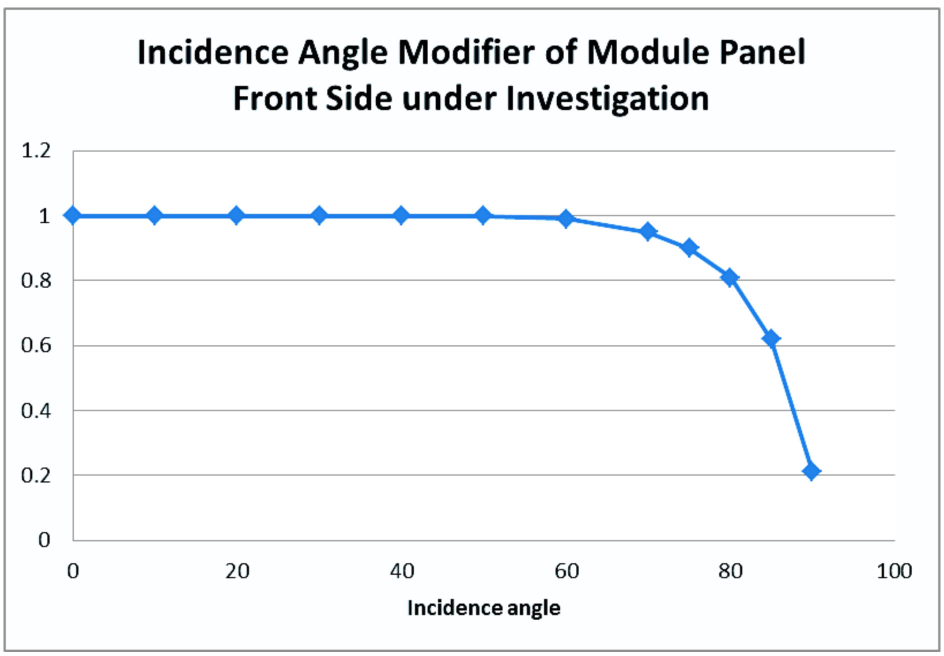

Figure 28 Incidence Angle Modifier (IAM) of Module Panel Front Side

3.7 Considerations of solar cell and solar panel reflections

Another aspect is the reflection from the panel to the ground and then re-reflected back to panel. According to model, the most significant panel reflection which returns back and received by the panel is when panels are set vertical and the solar beam reaches the panel at a very large incidence angle, therefore a large fraction of the beam is specularly reflected toward the near-by ground. At such worst case, the albedo of such near-by ground with extra panel-reflection-induced irradiance diffuses over a hemisphere, and part of it may return to panel(s).

Assuming such worst scenario and notice that, when the incidence is almost 90 degree, although the reflection is maximum, but the reflection is also at such angle which cannot enter the panel at all. Therefore, the maximum resulted second reflection back into panel then solar cell may be estimated tracing the ray as follow.

Step 1: Considering the panel reflectance along with the transmittance of the extra ground reflection together, the maximum possible such second order reflection can transmitting into the panel is when beam incidence angle = 78 degree. 32.6% of the beam is reflected toward the ground.

Step 2: In such case, there is a brighter strip on the ground. Also considering the worst scenario for the panel setting at the lowest clearance of 0.2 m, the horizontal distance of the brighter strip is between 0.042m and 0.468m. Even consider such a strip is stretching east-west infinite. The solid angle of this strip seen at the panel bottom takes 1.84 solid angle. i.e. at most, there is $1.84/\pi=58\%$ of the ground solid angle seen from the bottom of panel is of such brighter strip.

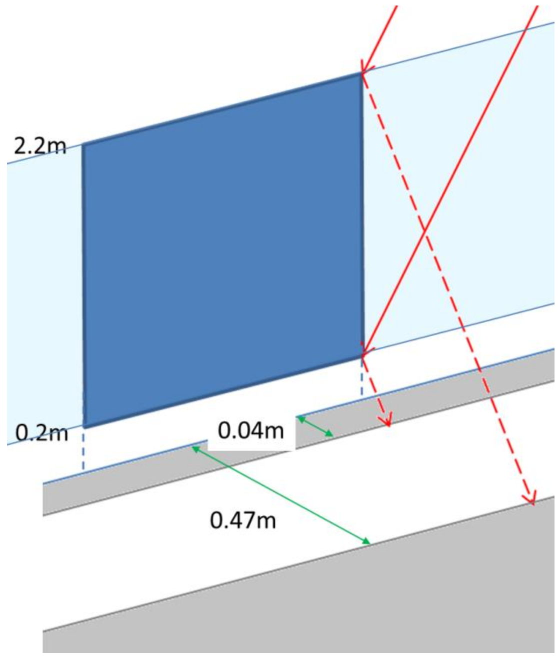

Figure 29 Panel(s) specular reflection of beam gives a bright strip on near-by ground

Step 3: The ground reflection follows the same path back to the panel has 67.4% transmitted through the glass-air interface.

Step 4: Furthermore, considering the product of IAM and reflecting –back-to-panel incidence angle's cosine factor, the average from 0 to 90 degree is 0.63, while the product at 72 degree incidence is 0.22. This gives a ratio of 35%.

Multiplying all the above factors gives a maximum of about 4% top-up on beam's ground reflection as contribution to the total on-panel irradiance. Considering this is the scenario of all the related factors set to the worst cases which actually happens rarely; also, such ground reflection is a small fraction of the total irradiance received by panel, and only happens along with solar beam irradiance, hence it is always a tiny fraction of the total photonic power entering solar cells at any time stamp. Such small amount requires much more complicated computation, it is justifiable to have this second order reflection to be neglected.

3.8 Solar cell modeling

3.8.1 Conversion from power entered in silicon into current

When irradiance is from the front side of panel, once the total amount of photonic power entered silicon layer, a conversion from photonic power into electrical current is taking place. This conversion is calculated based on an IQE curve and the photocurrent may be calculated [72]:

$$I_{SC} = q\int_{\lambda_1}^{\lambda_2} \frac{P(\lambda)}{E(\lambda)} T(\lambda) IQE(\lambda) d\lambda \tag{3.15}$$

Where I_{SC} is photon generated short circuit current in solar cell, q is electron charge, $P(\lambda)$ photonic influx power at a given wavelength, $E(\lambda)$ the photon energy at this wavelength, $T(\lambda)$ is optical transmittance at this wavelength when at normal incidence on solar cell defined as a ratio of photonic flux power right above the solar cell (should be above anti-reflection coating if there is such layer) and right after entering the solar cell exciton generation region, and $IQE(\lambda)$ is solar cell internal quantum efficiency at this wavelength.

In this project, it is simplified as all the irradiance is a standard AM 1.5G source and there is no spectral change when flux travelling through interfaces. Based on this simplification, once a flux entered silicon layer (the exciton generation region of solar cell in this project) on the front side, a conversion from photonic power into electrical current is done by multiplying a conversion ratio.

Due to lack of internal quantum efficiency (IQE) data of the bifacial solar panel under investigation, the conversion ratio $r_{PI} = 0.425(A/W)$ at STC condition used in this project is calculated based on an IQE curve of a typical good quality monocrystalline mono-facial silicon solar cell standard AM1.5G spectrum (Figure 30) [73]. This is also mentioned in Statement of Originality.

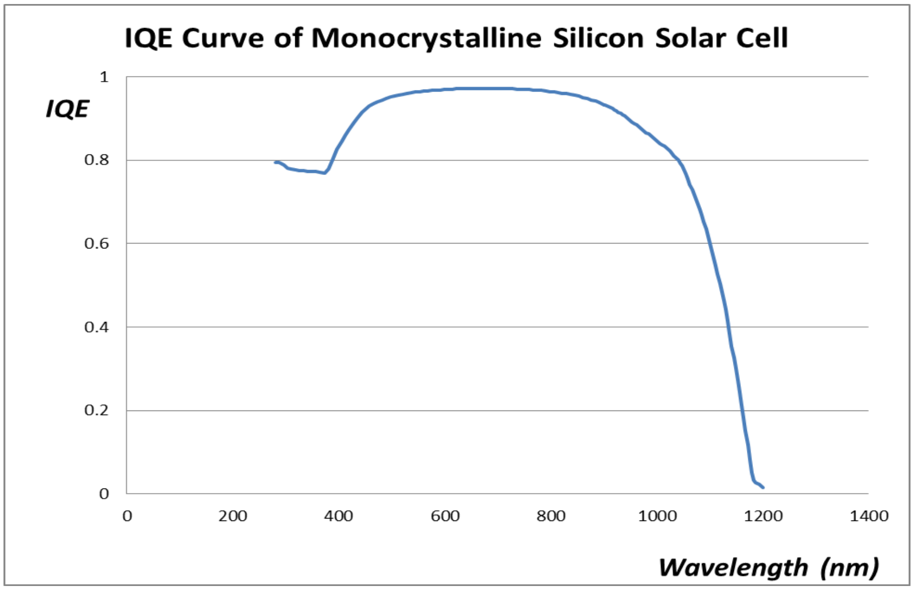

Figure 30 IQE curve of monocrystalline silicon solar cell to be used in photonic to short circuit current conversion [73]

Once the photonic power entered silicon is known, the corresponding short circuit current may be acquired from the above mentioned conversion ratio.

When irradiance is from rear side, the conversion efficiency is that of the front side multiplying solar cell's bifaciality of 95% (value provided by Company).

The total short circuit current of the solar cell under irradiation from both sides is simply the sum from both sides.

3.8.2 Solar cell single diode model, parameters, and its I-V curve

A measured dark albedo I-V curve is provided by the company (Figure 31). Using single-diode model for one solar cell and assuming all the 72 solar cells have identical properties, the series and shunt resistances are distributed evenly and the cells receive identical irradiance, the I-V curve of a single cell is simply 1/72 of the total voltage at the same current level. The single-diode model with series and parallel (shunt) resistances may be expressed as [3]:

$$I = I_{SC} - I_0 \left[e^{\frac{q(V + I \bullet R_S)}{mk \cdot t}} - 1 \right] - \frac{V + I \bullet R_S}{R_P},$$

where R_S and R_P are solar cell series and parallel resistances respectively. Temperature t is at Standard Testing Condition of 298.15k. Through regression, values of the parameters are obtained and listed below (Figure 31):

m=1.445; $I_0 = 4.651\times10^{-8}$; $R_S = 0.008791(\Omega / cell)$; $R_P = 2.059(\Omega / cell)$; $I_{SC} = 8.9895$(A) and $V_{OC} = 0.707(V)$.

$$I = I_{SC} - 4.651\times10^{-8}\left[e^{\frac{q(\mathrm{V}+0.008791\cdot I)}{1.445k\cdot t}} - 1\right] - \frac{V + 0.008791\cdot I}{2.059} \text{ (Ampere/Cell)} \tag{3.16}$$

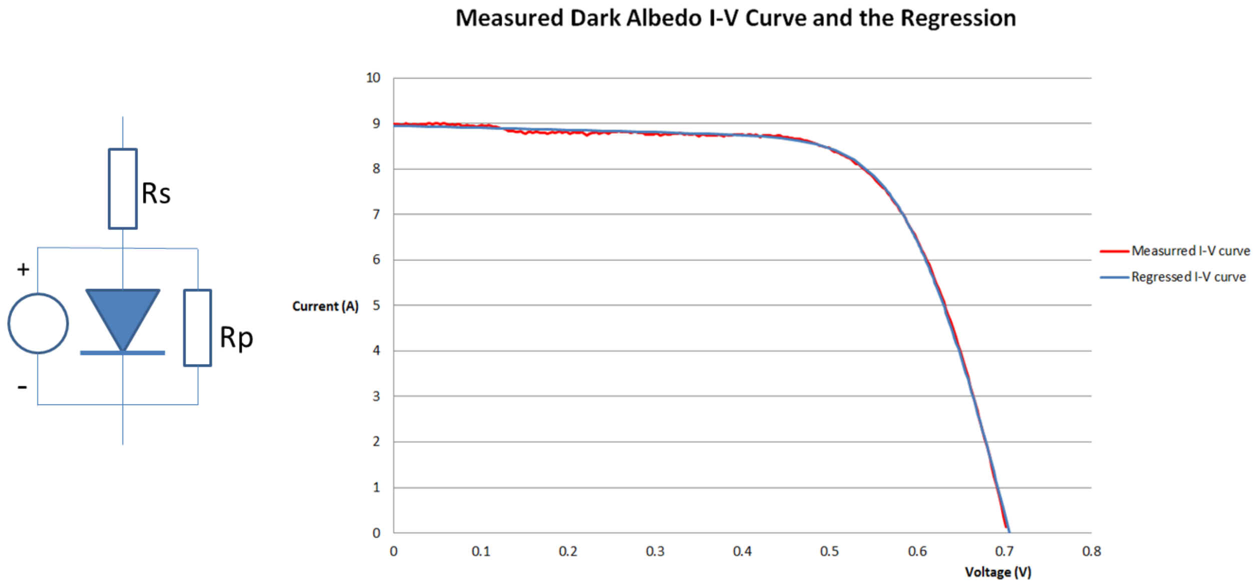

Figure 31 Left: Solar cell single-diode model; Right: Measured Dark Albedo I-V Curve Provided by Celestica and its Regression

3.8.3 Panel temperature estimation

The panel temperature may be estimated as follow once the total irradiance received on the glass surfaces is known [74, 75]:

$$t_{Module} = t_{AmbientAir} + \frac{NOCT - 20}{800} E(\mathrm{W/m^2}) \tag{3.17}$$

where E is the received irradiance by the panel in W/m^2. An average of irradiance over the panel is used since the assumption that all solar cells on the panel have the same temperature at the same time. Module temperature will be lower than this when wind velocity is high, as this model does not take wind into consideration due to data availability. Nominal Operation Cell Temperature (NOCT) for a typical module is suggested as 48°C in [74], and 47°C in [75]. Here in this project, it is chosen 46°C from manufacturer's data sheet (46+/-2°C) [70]. The lower NOCT is possibly because of the reduced infrared absorption without the metal fully covered rear side.

3.8.4 Diode model adjustment when working temperature is off STC

Short-circuit current, $I_{SC}(t)$ varies with temperature as when temperature increases, the band gap decreases allowing more photons to generate electron-and-hole pairs, but open circuit voltage deceases along with the band gap. The relationship of short circuit current and open circuit voltage vs. temperature may be expressed as:

$$I_{SC}(t) = I_{SC.STC}[1 + 0.0003(t - 298.15)] \tag{3.18}$$

and:

$$V_{OC}(t) = V_{OC.STC}[1 - 0.0023(t - 298.15)] \tag{3.19}$$

Where T is the panel temperature in Kelvin, the short circuit current temperature coefficient $0.0003/°C$ (or $0.0003/k$) and open circuit voltage temperature coefficient $-0.0023/°C$ (or $-0.0023/k$) are from manufacturer's datasheet [70].

For the dark current vs. temperature, since this is diode internal property, it can be calculated using ideal diode equation with ideality factor m obtained from measured I-V curve as above described: $I_0(t) = I_{SC}(t) \bullet e^{\frac{-qV_{OC}(t)}{mk \cdot t}}$.

Assuming all the solar cells have the same properties, and have the same temperature at the same time, hence, the same coefficient values for their dark current expression.

Since V_{OC} also varies with I_{SC}, it needs to have an open circuit voltage expression including both shot circuit current and temperature. To simplify the calculation, using the ideal diode model's simple formula and the related values from STC and its regression gives:

$$V_{OC}(t, I_{SC}) = V_{OC.STC}\left[\frac{\ln(I_{SC.STC.AVE} / \mathrm{I}_{0.\mathrm{STC}})}{\ln(\mathrm{I}_{\mathrm{SC}.STC} / \mathrm{I}_{0.\mathrm{STC}})}\right][1\text{-}0.0023\times(t\text{-}298.15)] \tag{3.20}$$

where $V_{OC.STC}$ and $\mathrm{I}_{\mathrm{SC}.STC}$ are from the STC measured I-V curve provided by Celestica; $I_{0.STC}$ is the dark current value regressed from the curve; $I_{SC.STC.AVE}$ is the average of all solar cell short circuit currents converted from photonic power and not yet adjusted by temperature coefficient. Therefore, dark current may be finally expressed as:

$$I_0(t, I_{SC}) = I_{SC.AVE}[1+0.0003(t-298.15)]\bullet e^{\frac{-q}{mk\cdot t}\left\{V_{OC.STC}\left[\frac{\ln(\mathrm{I}_{\mathrm{SC.STC.AVE}}/\mathrm{I}_{0.\mathrm{STC}})}{\ln(\mathrm{I}_{\mathrm{SC}.STC}/\mathrm{I}_{0.\mathrm{STC}})}\right][1\text{-}0.0023(t\text{-}298.15)]\right\}} \tag{3.21}$$

The resulted dark current agrees very well to other researchers tested results [76].

A resulted example of the dark current vs. solar cell short circuit current and working temperature based on eq. (3.21) is shown in Figure 32. It can be seen that increasing working temperature raises dark current exponentially, while short circuit has a much less effect on dark current.

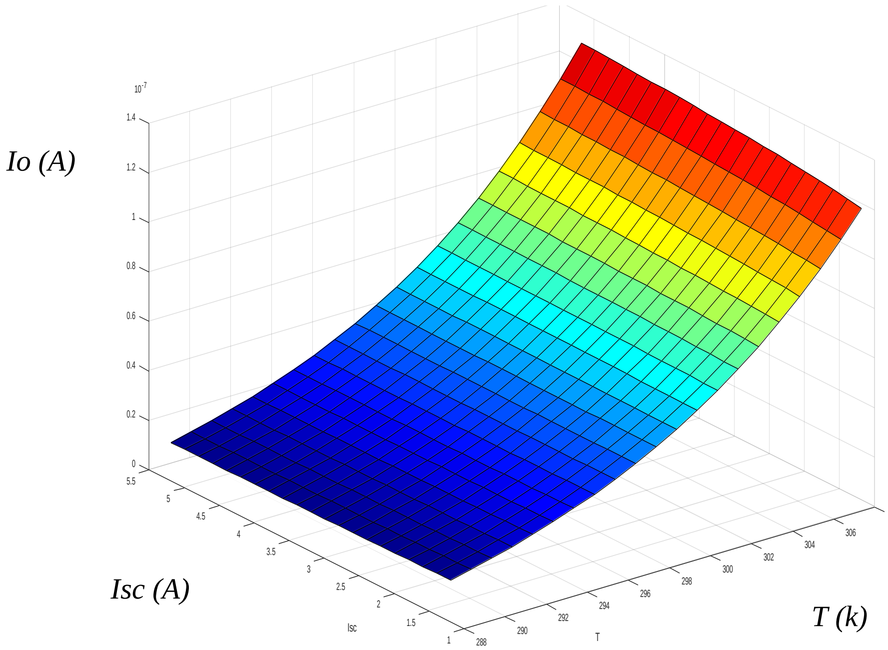

Figure 32 Solar cell dark current vs. short circuit current and working temperature from eq. (3.21)

3.8.5 Power and energy outputs

Since all the solar cells on a panel are wired in series, summing up in voltage of all these I-V curves gives the total I-V curve of the panel. Then finding the max power point gives the output power of the whole panel at each time stamp, and multiplying the time stamp span (3600 seconds) gives the energy output of each time stamp.

A sum up for each time stamp gives the annual energy yield.

Chapter 4 Simulation Algorithm Design

The simulation is designed using MATLAB©. The model in-takes data at an hourly base for a typical meteorological year; builds up geometric structures of sky dome, ground as reflector, panels and their racking posts; checks the ray blocking and shading due to the geometry; and outputs the annual energy generated by a bi-facial solar panel under investigation (Figure 33).

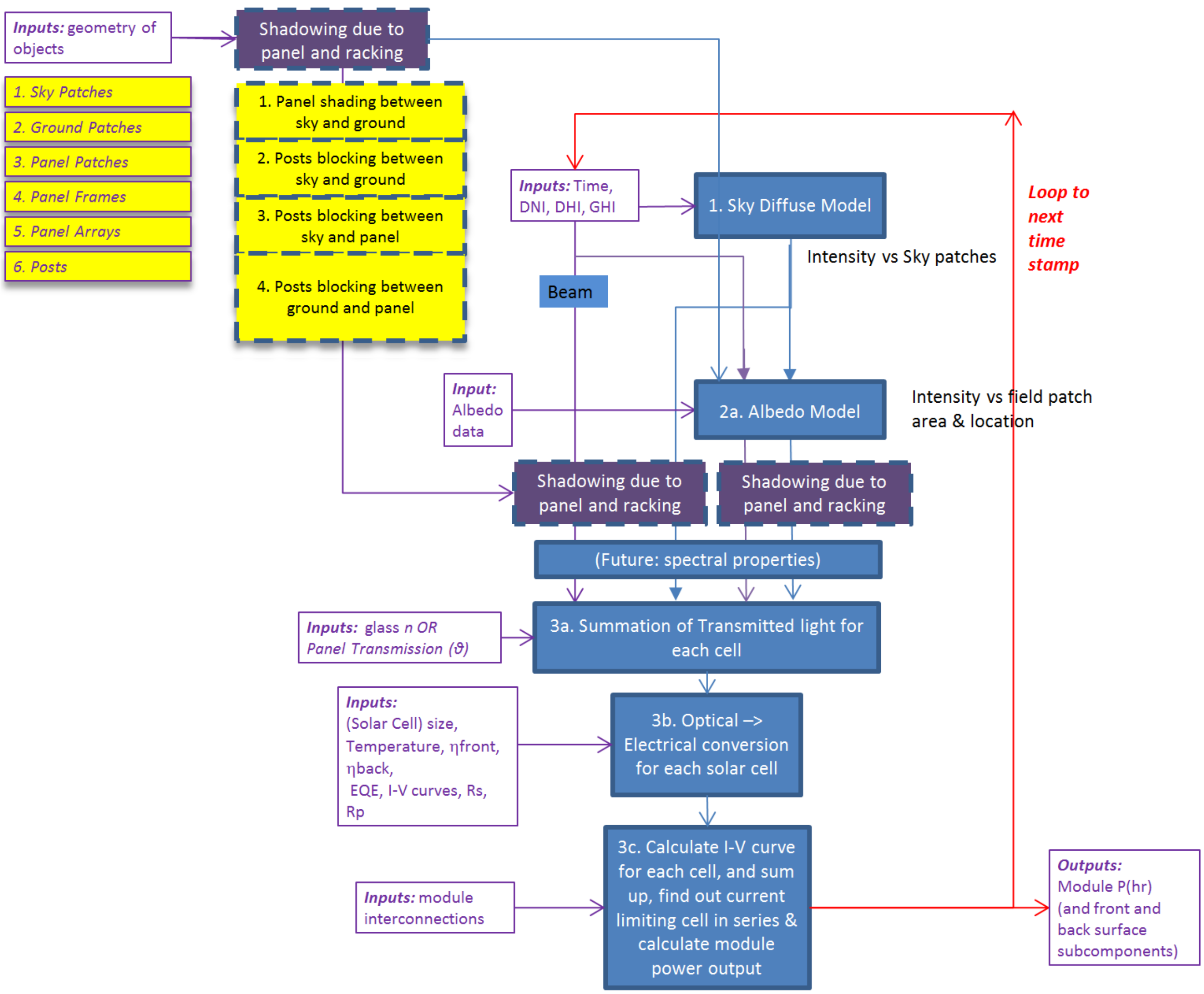

Figure 33 The top-layer scheme of the bifacial solar panel simulation algorithm

The first section of this chapter sequentially describes the sub-models one by one in general. The following sections will go into detail explanations of the most complex parts and points in each of the sub-models. Please refer to Appendix D for parameter names and meanings.

4.1 The main function structure and its components

The main function is called: "BifacialAnnualPowerOutput". Following the logic flow of the algorithm shown above, the first layer structure of the main function is designed as below (Figure 34). The main parts of the simulation are briefed in sub-sections, and more detailed explanations are in following sections.

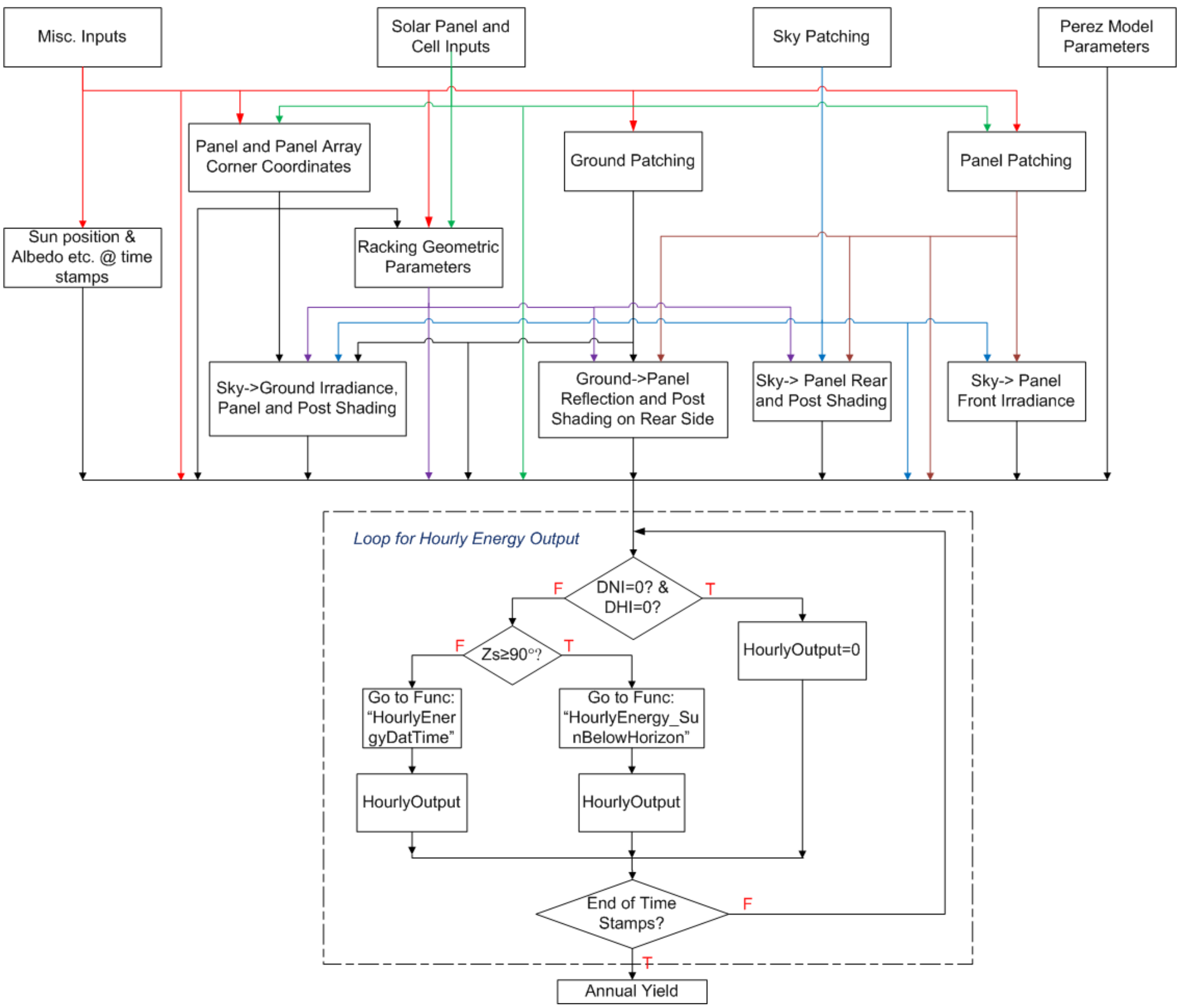

Figure 34 The scheme of the bifacial solar panel simulation flow chart in Matlab

4.1.1 Miscellaneous inputs and input functions

1) There are a few parameters which are provided in the main function for easy to change their values when running simulation in analysis. These parameters include sky patch and ground patch resolutions, solar panel azimuth angle, tilting angle and clearance.

2) The first function "CWEC_SunPosition_AlbedoData" mainly takes data from Excel file and load into MATLAB, and the data are listed below:

Input	***Input names in code***
local latitude (°)	L
local longitude (°)	Longitude
longitude of the time zone (°)	Longitude_timeZone
Output	***Output names in code***
day numbers in a year	n_day
hour numbers in a day	Hr
extraterrestrial solar radiance changed daily (W/m^2)	I0
Direct normal irradiance (W/m^2)	DNI
Diffuse horizontal irradiance (W/m^2)	DHI
Ambient temperature at test site (°C)	T_amb
diffuse reflectance (Appendix B)	rho
forward anisotropic coefficient (Appendix B)	f_af
backward anisotropic coefficient (Appendix B)	f_ab
solar elevation angle (°)	Beta_Sun
solar zenith angle (°)	Zenith_Sun
solar azimuth angel (°)	phi_Sun
air mass	airMass

3) The third function "Perez1993Parameters" reads data for Perez 1993 model from an Excel file, and outputs Perez model's coefficients based on their paper [33].

Detailed explanation and schematic chart are in section 4.2 .

4.1.2 Panel, ground and Sky dome geometry related functions

Firstly, there are five functions either provide or generate geometric parameters of panel, panel array and racking. Details will be explained in sub-section 4.3.1 .

Secondly, comes the ground geometry function "groundPatchGenetation" contains two parts. The first part generates ground patches as annular sectors in polar coordinate system, and the second one converts the geometric parameters into Cartesian coordinates. Refer to sub-section 4.3.2 for details.

Thirdly, there are three sky dome geometry and related functions (details to be explained in sub-section 4.3.3), namely:

> "skyPatchAndSp_Panel_front_Normalized_irrdiance",
> "sky_Panel_rear_blockingAnd_normalized_irradiance" and
> "SkyPatch_to_Gp_PanelAndPosts_BlockChecking".

The fourth part contains functions regarding ground to panel reflection and related error reducing compensations. There are three functions in this part.

1) The first function "Gp_Pp_RayDirection_And_Rear_Post_Block_Check" outputs firstly a 4-D matrix providing information of posts blocking reflection rays from ground patches toward panel rear side patches, and secondly also a 4-D matrix of horizontal angles of each said rays to be used in calculations for directional reflection of solar beam.

2) The second function "groundToPanel_Compensating" outputs 4-D matrices with information of ground patch to panel patch reflection geometric factors on both front and rear side, and geometric factors relating to them. This function also carries out compensation of geometric approximation error for Lambertian reflection and outputs two 2-D matrices each for panel front and rear side (Such error analysis is discussed in sub-sections 3.5.1 and 3.5.2).

3) The third function “groundToPanel_WithCompensation” is a relatively simple function, and outputs 4-D matrices of ground to panel reflection geometric and compensating information from above functions.

Details for these functions will be explained in section 4.4 .

Once these mainly geometric related functions are performed, the simulation now goes into a loop calculating the power output at each time stamp over the whole year.

4.1.3 Loop to compute power and energy output at each time stamp as well as the total annual energy output

This part is a loop to compute power and energy output at each time stamp as well as the total annual energy output. There are three choices at each time stamp. When both DNI and DHI are zero at a time stamp, which is considered as during night time, the output hourly energy is simply zero, otherwise, the hourly energy output requires calculation.

When the sun is above horizon, the code chooses function “HourlyEnergyDayTime” to calculate corresponding hourly energy output.

When the sun is below horizon, such as right before sunrise, or right after sunset, when there is still some diffuse radiance in the sky but no direct solar beam, the code chooses another function “HourlyEnergy_SunBelowHorizon” to calculate the hourly energy output. Obviously, this function only needs to calculate sky diffuse radiance and the corresponding ground reflection. In such case, since Perez model cannot handle such situation where the sun is below horizon, a simplified isotropic sky diffuse distribution model is used. Details are explained in section 4.5 .

After the loop, the hourly energy outputs are summed up to provide the annual energy yield.

In following sections, the above introduced code parts are to be explained in more details with those parts and functions of higher complexity are chosen to be given further detailed descriptions and explanations of algorithms to help better understanding.

4.2 Details in Miscellaneous inputs and input functions

In the first function in this part, "CWEC_SunPosition_AlbedoData", besides reading data from Excel file "CAN_ON_Ottawa.716280_CWECepw_a" in the same folder, there is also a sub-function "SunPosition", which provides outputs of solar elevation angle "Beta_Sun", and solar zenith angle "Zenith_Sun" using eq. (2.2) and eq. (2.3); and the solar azimuth angle "phi_Sun" using eq. (2.4); and air mass value "airMass" using eq. (2.5). The flow chart of the "CWEC_SunPosition_AlbedoData" function is shown in Figure 35 below. The variable names and their meanings can be found in Appendix D .

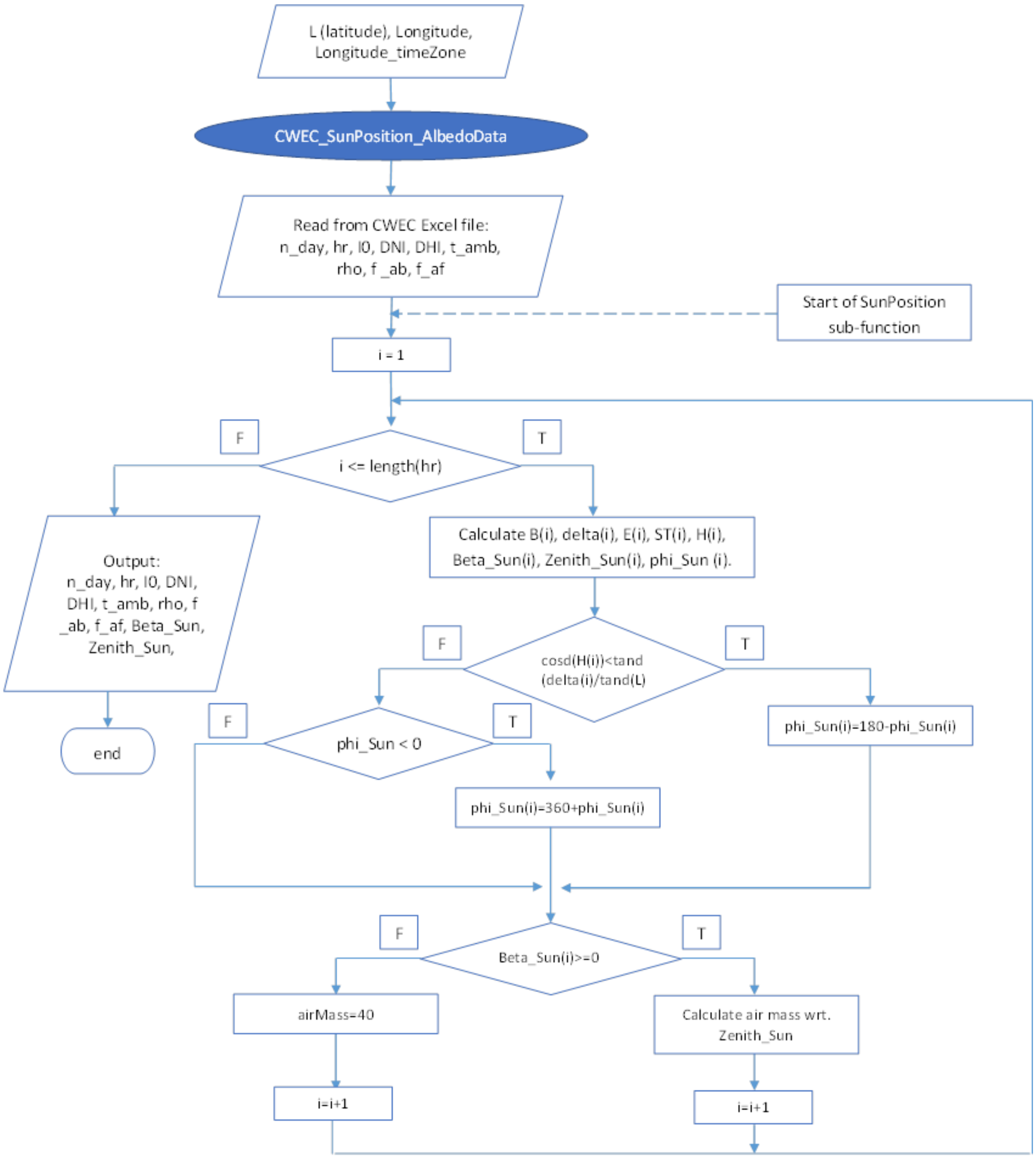

Figure 35 Flow chart of function “CWEC_SunPosition_AlbedoData” algorithm

4.3 Details in Panel, ground and sky dome geometries related functions

In this part, there are five functions either provide or generate geometric parameters of panel, panel array and racking. The five functions either provide or generate geometric parameters of panel, panel array and racking. Two of them will be given more detailed explanation afterward.

1) The first panel related function “PanelSolarCellParameters” outputs panel and solar cell related parameters. Most of these parameters are provided by manufacturers. For other parameters, the solar cell patching division number here we choose it to be 4. The front side and rear side normal incidence transmittances are calculated based on the interfaces the light needs to pass through to get into the silicon layer. The solar cell electrical parameters at STC are regressed values from a measured I-V curve of the panel under investigation. The front and rear side uncovered area ratios are also calculated based on the dimensions of bus bars and fingers provided in manufacturer’s data sheet. The photonic power to short circuit current conversion ratio “Ratio_PhPToI” is also calculated based on IQE [73].

2) The second function “PanelCorners” provides the geometric dimensions of the panel under investigation. The inputs are panel tilt angle, azimuth angle, clearance, panel height, and panel width, and outputs are the panel four corners x, y, z coordinates and the height of the taller posts.

3) The third function “PanelArrayCorners” provides the geometric dimensions of the five panels as a whole piece as that the gap between panels is too small hence being neglected. The inputs in fifth function are input here plus panel numbers and Racking post side size. The outputs are the panel array four corners’ *x*, *y*, *z* coordinates of the whole panel array.

4) The fourth function “PanelPatchCoordinatesAndAreaAndRatio”, based on panel geometry parameters, provides the panel patching related outputs for later calculations.

5) The fifth function “SquarePostsCoordinates” provides the four corner coordinates of each post for later calculations.

4.3.1 The first panel related function “PanelSolarCellParameters”

1) Provides panel and solar cell geometric parameters;

2) Calculates transmittances of panel front and rear sides based on the different numbers of layers and corresponding refractive indices on the optical paths;

3) Provides values for conversion ration from silicon layer received photonic power to current, and regressed solar cell electrical parameters such as tested short circuit current, open circuit voltage, series and shunt resistances, dark current, and ideality factor. These values are calculated based on measured data from manufacturer and considered as inputs to the simulation.

4.3.2 Details in ground geometry related function"groundPatchGenetation"

This function firstly generates ground patches as annular sectors in polar coordinate system, and then converts the geometric parameters into Cartesian coordinates.

The ground patch radial sizes are determined based on the highest point of the panel. The height at the top of the panel is determined by the clearance, the panel's size and its tilting angle. Such ground patching size determination is because that the higher the top of the panel, the larger the ground near-field area is needed to reduce the simulation error in far field simplification.

The far field patch center radius is considered a constant for all the panel patches. To ensure negligible error due to such simplification, it requires the far field patches to be further away if the panel top point is at a greater height. Therefore, the ground patching radii are functions of the top point height. The patch size is smaller near the coordinate center thus also near or right underneath the panel.

For the near field patches, the center of mass is used as the patch's representative point, which may be calculated as:

$$r_{GpCM} = \frac{2}{3} \bullet \frac{\sin(\varphi_{Gp\bullet div}/2)}{\varphi_{Gp\bullet div}/2} \bullet \frac{R_{Gp}{}^2 + r_{Gp}R_{Gp} + r_{Gp}{}^2}{R_{Gp} + r_{Gp}}$$

Where $\varphi_{Gp\bullet div}$ is the azimuth division angle in radians, R_{Gp} and r_{Gp} are respectively the outer and inner radius of the annular sector. Here r becomes 0 when the sector is the inner most, i.e. touching the origin.

4.3.3 Details in sky dome geometry and related functions

4.3.3.1 The first function "skyPatchAndSp_Panel_front_Normalized_irrdiance"

The first function "skyPatchAndSp_Panel_front_Normalized_irrdiance" generates sky patches in a spherical coordinates with its radius normalized to be unit. By simplifying the sky patches to a trapezoidal shape, the zenith angle of sky patch center of mass may be obtained as:

$$Z_{SpCM} = Z_{up} + \frac{90^\circ}{3Z_{Sp\bullet div}} \left[\frac{\sin(Z_{up}) + 2\sin(Z_{low})}{\sin(Z_{up}) + \sin(Z_{low})} \right].$$

It then checks which sky patches to be seen by the panel front side, and calculates the geometric-sense contribution of each sky patch onto the front side. Similar to the checking condition about whether the sun is shining on front or rear side of the panel, for each sky patch, once its incidence angle on panel front is acquired, it is checked as shown in Figure 36.

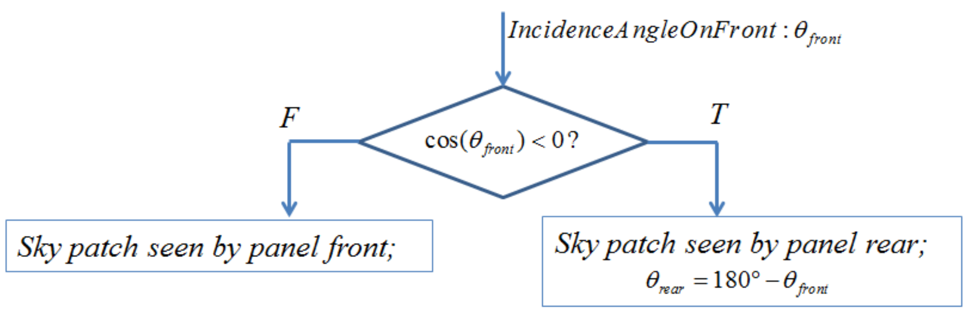

Figure 36 Flow chart for checking whether each sky patch is seen by panel front or rear side

As a sky patch is not seen by the front side, the sky patch is not directly contributing to the front side irradiance. The model set its cosine factor: $\cos(\theta_{SpPf}) = 0$, so to eliminate its contribution. The same zero contribution is set to rear side if a sky patch is not seen by rear side.

The sky patches are generated as over a hemisphere with unit radius, a normalized hemisphere. The total hemispheric normalized area is 2π, which is also the hemispheric solid angle. Likewise, a sky patch's normalized area is the same as its solid angle seen from ground.

Then, we normalize the sky with an isotropic and unit power flux per solid angle, and for a normalized isotropic diffuse sky, its normalized irradiance from one patch onto panel front may be $I_{SpPfNormalized} = \Omega_{Sp} \bullet \cos(\theta_{SpPf})$ where Ω_{Sp} is the sky patch's solid angle seen on ground, we also have $I_{SpPfNormalized} = \mathrm{A}_{Sp} \bullet \cos(\theta_{SpPf})$ where A_{Sp} is the sky patch's normalized area. In such way, the matrices containing geometric information are to be used later with sky diffuse distribution.

4.3.3.2 The second function "sky_Panel_rear_blockingAnd_normalized_irradiance"

This function firstly generates a 4-D matrix called "Sp_Pp_Post_Block". Its elements take value 0 when a corresponding sky patch is not seen by the rear side, and take value 1 if is seen. Then it uses geometric information of posts locations, and checks for each ray linking a seen sky patch and a panel rear patch to see if the ray is blocked by any of the taller posts. If the ray is blocked, the corresponding element is reset to 0.

Step 1: check if a sky patch is on the left or right side of the panel rear side, and chooses either of the corresponding sub functions: and "Sp_Pp_Post_left" and "Sp_Pp_Check_right". Each of the function only checks half of the posts, hence saves running time.

Step 2: within one of the sub-function: the ray line function is generated using the sky patch's elevation and azimuth angles and the ground patch central coordinates. The post side is a vertical plane, its function is same as the intersection line function between this vertical plane and the horizontal ground plane. Then, calculate the coordinates of the intersecting point of the ray and each of the panel side plane.

Step 3: now, checking if the intersecting point is between the post side edges and also within the post height (Figure 37). If the answers to both conditions are yes, the ray is blocked by this post side, and the corresponding matrix element is set to 0. Checking through all the posts gives a full picture of the post blocking between sky patches and panel rear side under such geometric arrangement.

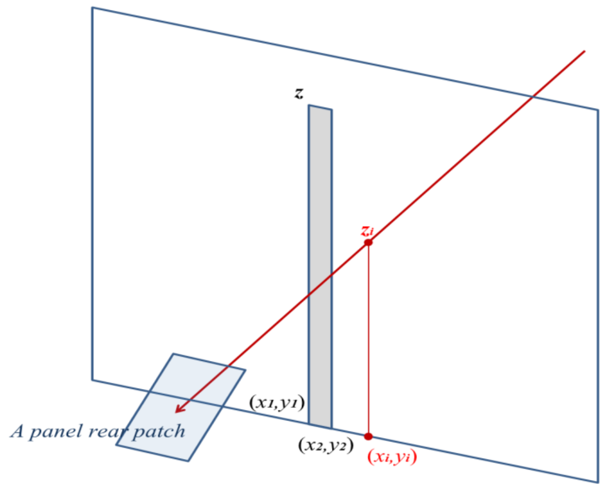

Figure 37 Diagram of whether post side blocking ray from sky patch toward panel rear patch, the grey-shaded narrow strip area represents a post side, and the larger parallelogram represents the plane containing it

Notice that if a post side, as well as the vertical plane containing it, is parallel to y-axis, we cannot judge whether the intersecting point is between the post side edges by comparing the edges' and the intersecting point's x coordinates. Vice versa, we cannot use y coordinates to judge it if the plane is parallel to x-axis. Therefore, another checking layer here to check whether the panel azimuth angle is near facing east or west, so to choose the intersection checking whether done with x coordinates or y coordinates.

Figure 38 shows the algorithm how the blocking is checked for one side of a post. Looping through all four sides of each post gives a 4-D matrix information of both viewing-factor and post blocking. Finally, it then also calculates the geometric-sense contribution of each sky patch onto the rear side.

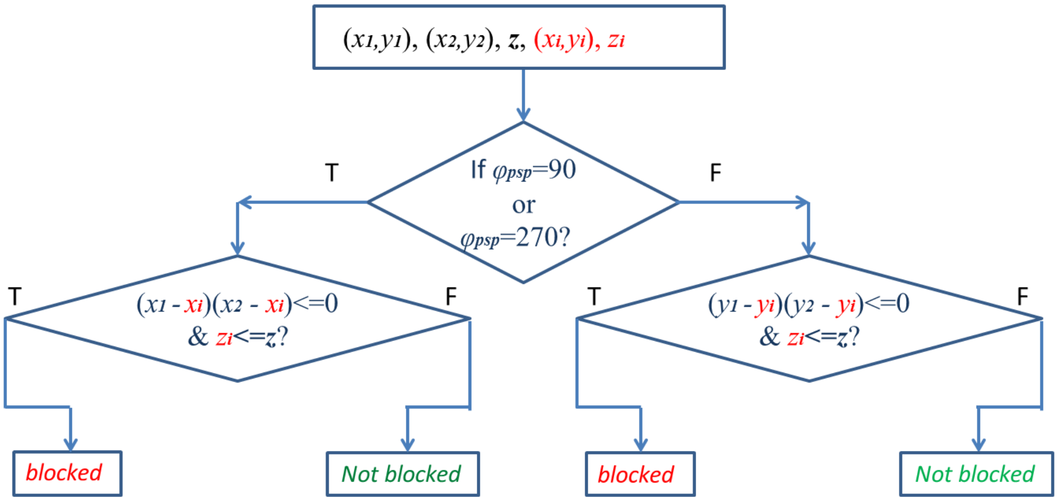

Figure 38 Checking whether a post side blocks ray from a sky patch toward a panel rear patch

4.3.3.3 The third function is "SkyPatch_to_Gp_PanelAndPosts_BlockChecking"

This function contains two sub-functions, one is to check posts blocking sky patch rays toward ground patches, and another is to check rays shaded by the panel array. The results are two 4-D matrices. A third matrix of same dimension can be obtained by element-by-element product of the two. This becomes the output as the normalized geometric-sensed sky diffuse radiation contribution to ground irradiance matrix with information of panel and post shading. Below are the sub-functions in details.

The blocking of a sky patch ray toward a ground patch is checked very similarly as that of sky patch toward a panel rear patch.

The panel is modeled as not transparent for solar cell covered areas but transparent elsewhere. The model simplified the calculation as a percentage of identical transparency all over the panel defined by the ratio of the transparent area to the total panel area. Therefore, there is a fraction of a ray, either sunbeam or a sky patch ray, hit the panel array, passes through and reaches the ground. This is discussed in sub-section 3.4.1.2 .

The sub-function "Sp_Gp_Panel_Shading_Check" checking of ray shading from a sky patch toward a ground patch by the panel array is also geometrically very similar. However, since the panel can be set at any tilting angle, the checking is more complicated.

When the panel tilting angle $\Sigma_P = 0$, i.e. the panel is set flat, the panel shading algorithm needs to be done differently. In this case, we need to check if the ray from sky patch toward ground patch hits the panel array horizontal rectangular area hanging at the height of clearance. If the hit is outside of the rectangular area, the ray is not shaded, the corresponding matrix element is set to be 1; if it is within the rectangular area, the ray is shaded, and thus the element is set to the value of the fraction passing through panel reaching ground patches (Figure 39).

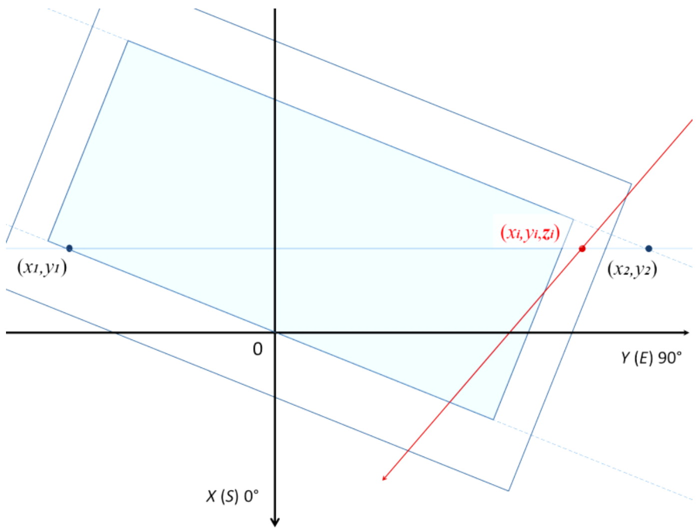

Figure 39 Diagram of whether panel array shading a ray from a sky patch toward a ground patch, the shaded area represents panel array, and the larger parallelogram represents the plane containing the panel array. Panel is set horizontal

When the panel is set at a non-zero tilting angle, it starts with checking if the intersecting point is within the panel height range, i.e. between the heights of the shorter posts and taller posts. The Z coordinate of the intersecting point is used to obtain the points on the panel array edges (x_1, y_1) and (x_2, y_2), and then using the coordinates of these two on-edge-points to check if the intersecting point is between the panel array left and right sides. The ray is shaded only when the point is within these two ranges. i.e. within the height range; and either between x_1 and x_2, or between y_1 and y_2 (Figure 40).

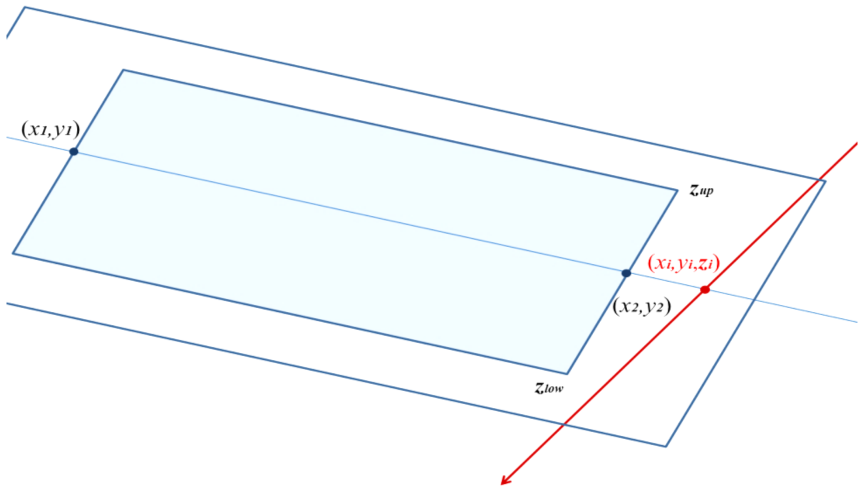

Figure 40 Diagram of whether panel array shading a ray from a sky patch toward a ground patch, the shaded area represents panel array, and the larger parallelogram represents the plane containing the panel array. Panel is set at a tilting angle

When panel array is approximately facing south, it is more accurate to use x coordinate to do the checking, and if it is approximately facing east or west, then use y coordinates. The flow chart of the whole function is shown in Figure 41.

Now, applying element multiplication of the post blocking matrix with this panel array shading matrix gives another 4-D matrix containing all the post blocking and panel array shading information for all the rays from sky patches toward ground patches.

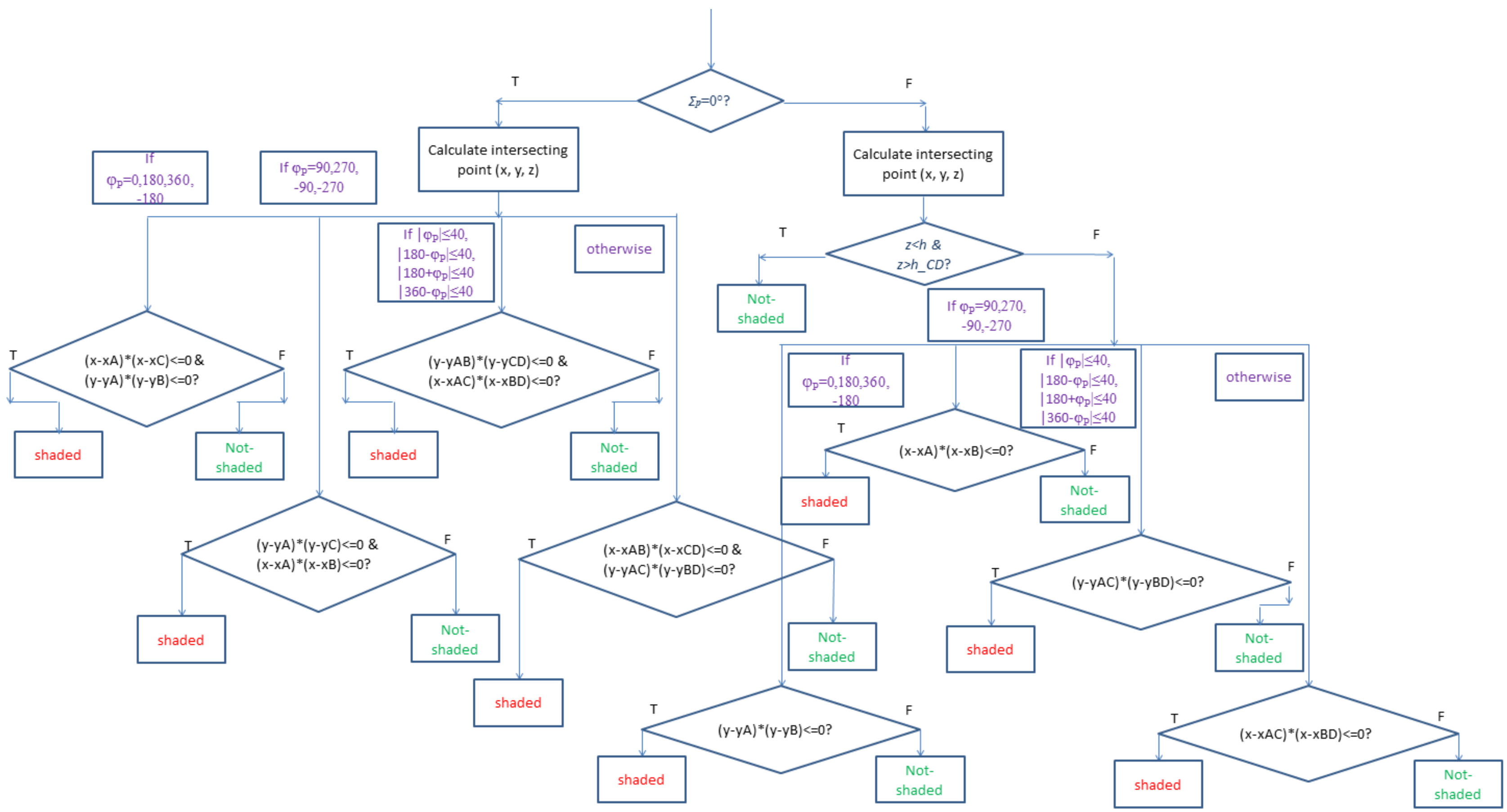

Figure 41 Sub-function "Sp_Gp_Panel_Blocking_Check" checking ray from sky patch toward ground patch shaded by panel array

4.4 Details in ground to panel reflection and related functions

4.4.1 The first function "Gp_Pp_RayDirection_And_Rear_Post_Block_Check"

This function firstly outputs a 4-D matrix providing information of posts blocking reflection rays from ground patches toward panel rear side patches, and secondly also a 4-D matrix of horizontal angles of each said rays(see eq. (4.1)) to be used in calculations for directional reflection of solar beam.

Since the horizontal direction of a reflecting ray from a ground patch toward a panel patch is calculated from inverse trigonometric function (see eq.(4.1)), the exact direction (in which quadrant) needs an algorithm to check and determine (Table 1).

$$\omega_{GpPpH} = \arcsin\left[\frac{y_{Gp} - y_{Pp}}{\sqrt{(y_{Gp} - y_{Pp})^2 + (x_{Gp} - y_{Pp})^2}}\right] \tag{4.1}$$

Table 1 determination of ground patch to panel patch ray horizontal angular direction

if $\omega_{GpPpH} \geq 0$ && $(x_{Gp}-x_{Pp}) \geq 0$	$\omega_{GpPpH} = \omega_{GpPpH}$
if $\omega_{GpPpH} \geq 0$ && $(x_{Gp}-x_{Pp}) < 0$	$\omega_{GpPpH} = 180 - \omega_{GpPpH}$
if $\omega_{GpPpH} < 0$ && $(x_{Gp}-x_{Pp}) \leq 0$	$\omega_{GpPpH} = 180 + \lvert \omega_{GpPpH} \rvert$
otherwise	$\omega_{GpPpH} = 360 - \lvert \omega_{GpPpH} \rvert$

Then, there is a condition check, whether the panels are set horizontal? If yes, there is a sub-function "Gp_Pp_PostsBlocking_Allover_Check_Sigma_p_0" specifically for such setting, this sub-function is called for each of the ground patch and panel patch pair, thus eventually provide a 4-D matrix for the ground to panel rear side reflection post blocking information.

There is another sub-function "Gp_Pp_PostsBlocking_Allover_Check" for tilted setup. This sub-function has a relatively higher complexity. Firstly, the sub-function checks if the panel array is facing east or west or other directions? There is a checking condition whether a ground patch can be seen by panel rear side, and this checking condition has different expression for each of the above mentioned panel facings. If a ground patch cannot be seen by the rear side, the matrix element is assigned a 0, otherwise, the sub-function continues. The following steps under each of the panel array directions are the same, and the flow chart is shown below (Figure 42):

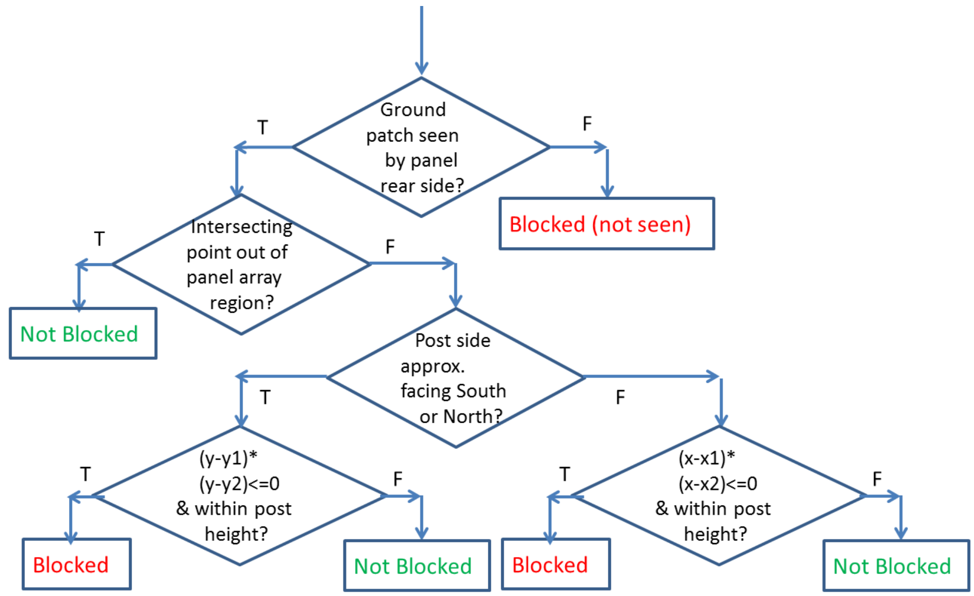

Figure 42 flow chart of sub-function "Gp_Pp_PostsBlocking_Allover_Check" checking if a reflection is blocked from a ground patch toward a panel rear side patch by any of the post side

4.4.2 The second function "groundToPanel_Compensating"

This function "groundToPanel_Compensating" outputs 4-D matrices of

(a) Elevation angles of each above said ground patch toward panel patch rays;

(b) Checking which ground patches being seen by panel front side, and then incidence angles onto front side panel patches of the said rays;

(c) Incidence angles onto rear side panel patches of the said rays;

(d) Spatial distances/lengths of each said rays;

(e) The ground patch to front panel patch reflection geometric factor, in which each element is a purely geometric-sensed ground to panel reflection contribution factor:

$f_{GeoGPf}= f_{SeeGPf} * \Omega_{GpPpf} * cos(\theta_{GpPpf})$,

where f_{SeeGPf} is the seen factor (also called view factor by other authors) which is set to be one if a ground patch can be seen by panel front side, and set to zero if not be seen, Ω_{GpPpf} is ground patch solid angel seen from a panel patch, $cos(\theta_{GpPpf})$ is the panel patch incidence cosine factor. In Matlab code, the expression for a single element is given as: Gp_Ppf_geo=seeFactor_G_Pf*Gp_Pp_SolidAngle*cosd(theta_G_Pf);

(f) Similarly a factor for the rear side, except that the seen factor needs to include information of post blocking, i.e. if a reflecting ray from a ground patch toward a panel rear side patch is blocked by any of the posts, the matrix element is also set to zero;

As discussed in section 3.5 , ground reflection contains error mainly from ground patching, and requires compensation. The compensation for Lambertian reflection is done by a ratio of the theoretical value over the cumulated reflection sum up value for each panel patch. Therefore, this function also outputs two 2-D matrices each for panel front and rear side. More details on the compensation algorithm are explained below:

The model can deal with panel tilting angle from 0° to 90°. The ground reflection onto front side may become zero when tilting angle is near or equal to zero. This makes some or all of the front side compensating factors become 0/0 type discontinuity.

To avoid such failure, elements in both front and rear side compensating factor matrices are default to be 1s.

During the checking, keep the element’s value to be 1 if the theoretical value = 0.

Another type of situation is to check if any of the panel patches sees none of the ground patch centers, this panel patch compensating factor is also set to 1. This is the case only when the panel is set horizontal or almost horizontal, the rear side sees almost the whole ground, but front side does not see any or barely sees a very small number of far field ground patches at a skimming angle. In such circumstances, either the all the front panel patches, or some of them see none of the ground patch centers.

The normalized reflection received on the rear side is about 10^4 times greater than that received on the front side; besides, the received reflection on front side is at such an almost zero incidence angle and essentially impossible to have a transmittance. i.e. the reflection onto front side does not contribute any recognizable amount to the total. Therefore, it is acceptable to assign a small value to let the model overcome such 0/0 discontinuity without any de facto influence on the output.

Figure 43 shows the algorithm flow chart of checking conditions and the ground to panel compensating factor value setting process, where $f_{GpPpComp}$ is the ground to panel compensating factor (separately for front and rear side); $\Sigma_{GpPpRefl}$ is the sum-up of Lambertian reflection from ground patches received on the panel patch; and G_{Fract} is the normalized theoretical value of reflection from the ground fraction received by the panel side, and $G_{Fract.f} = \pi\rho\left(\frac{1-\cos\Sigma_P}{2}\right)$ for front side.

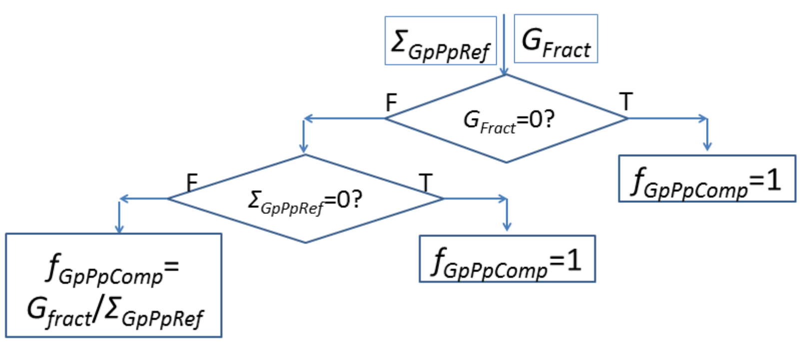

Figure 43 Lambertian reflection error compensating algorithm

Same procedure for rear side which also has a different value of normalized theoretical value of reflection as $G_{Fract.r} = \pi\rho\left(\frac{1+\cos\Sigma_P}{2}\right)$.

4.4.3 The third function “groundToPanel_WithCompensation”

The third function is a relatively simpler function which outputs three 4-D matrices. One is the compensated ground patch to front panel patch reflection geometric factor matrix; another is for panel rear side; and the third is for rear side but without post blocking between ground and panel rear side. The third matrix is used later for further error reduction in directional reflection calculation. The elements in these matrices contain corresponding geometric information for ground patch to panel patch reflection.

4.5 Details in the loop for hourly output energy

Once all the geometric related information are acquired or achieved through previous calculations, the model now starts to calculate the energy output at each hourly time stamp. The code uses a loop to go through the Excel file “CAN_ON_Ottawa.716280_CWECepw_a” row by row. The structure of the loop is shown below:

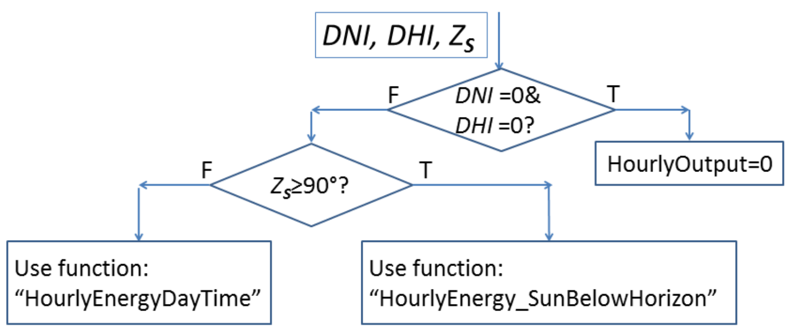

Figure 44 Hourly energy output calculation loop structure

Among these two, function “HourlyEnergyDayTime” has a much higher complexity. Here below is the detailed explanation for the most complicated parts in it.

4.5.1 A few detailed explanations for function “HourlyEnergyDayTime”

In function “HourlyEnergyDayTime” calculating day time hourly energy, if DNI is zero (such as when it is heavily overcast), the code set all the beam related values to be zero.

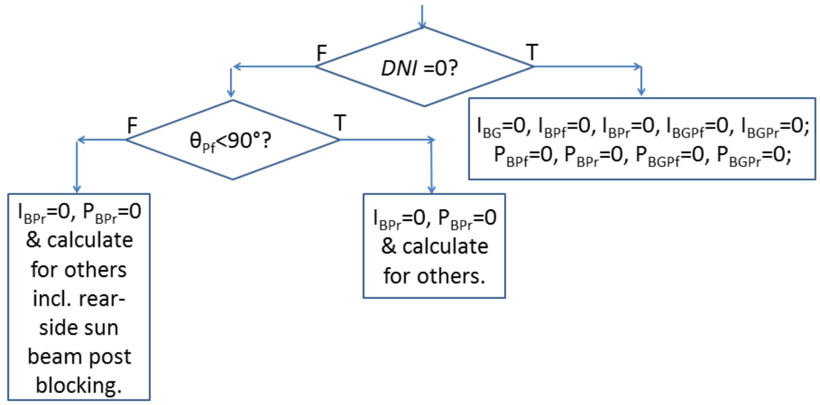

Figure 45 Flow chart for sun beam related calculations in sub-function "HourlyEnergyDayTime"

When calculating the ground reflection of sun beam, the whole ground reflection of sun beam is also geometrically compensated as Lambertian reflection to sky diffuse irradiance based on discussion in section 3.5.2 and 4.4.2 . However, the directional fraction of the beam reflection is of course not Lambertian, and there is a certain amount error remained, which is also due to the ground patching, (this will be shown from simulation model output in Figure 58). To compensate the remained error (separately for front and rear side), firstly, calculate the unshaded, Lambertian-compensated reflected beam radiance received on each patch of the panel; and secondly, a simple average of the radiance over all panel patches; thirdly, an error reduction compensating factor for beam reflection for each panel front patch is obtained as a ratio: $C_{ErBGPf.i} = \bar{I}_{BGPfNS} / I_{BGPfNS.i}$, where subscript *ErBGPf.i* stands for error reduction beam ground panel front and *i* means for each of the patches; *NS* in *BGPfNS* means not-shaded. In the code, it is expressed as:

"Sun_Gp_Ppf_ErReductCompensator(ip,jp)=
Sun_Gp_Ppf_NoShading_Panel_Avg/Sun_Gp_Ppf_NoShading_illumin_SumUp_Compensated(
ip,jp)" .

where (ip, jp) for panel patch index.

Similar to the compensating factors for Lambertian reflection, there are cases when the beam reflection is zero, which brings about the 0/0 type discontinuity. The algorithm to avoid simulation failure is shown below (Figure 46). Same algorithm applies to rear side. These error reduction compensating factors are to be multiplied to the previously calculated reflected irradiance of beam, and to the corresponding power received in the solar cells.

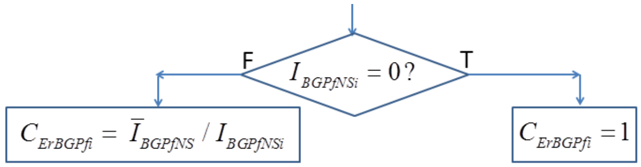

Figure 46 Flow chart for avoiding failure in directional reflection of beam error reduction compensation calculation

4.5.2 A few detailed explanations for sub-function "skyPatchFromPerez93Model"

As mentioned in section 3.2 for Perez 1993 model, when DHI value is provided, and solar zenith angle, epsilon hence the epsilon bin number and delta values are all known, the preparatory radiance value at the zenith can be calculated. Furthermore, once the solar azimuth angle is also known, the spherical angular distance from each sky patch to the sun can be calculated, and then the radiance values at each of the sky patch centers can be calculated following the steps shown below (Figure 47).

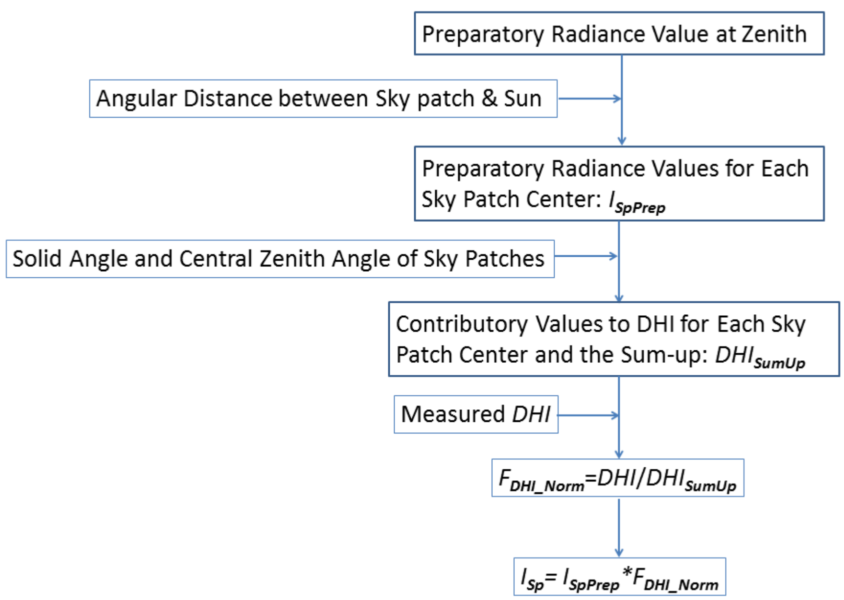

Figure 47 Flow chart to calculate radiance (W/Sr/m^2) at sky patch centers in Perez's 1993 model

These sky patch radiance values are used to calculate for panel incidence or transmittance with the corresponding angular information, also used to calculate shaded ground irradiance distribution which becomes a non-isotropic radiation source providing reflection toward panel.

Once the irradiances from the sun, the sky diffuse, the ground reflections are all calculated and acquired, as well as the ambient temperature is known from the "CWEC_SunPosition_AlbedoData", with the simplification that all the solar cells over the panel have the same working temperature at the same time, then this working temperature can be calculated using eq.(3.17).

At the same time, with the incidence angle information, the area ratio of bus bars and fingers, and the panel optical transfer functions for front and rear sides, all the corresponding photonic power from the sun, the sky diffuse, the ground reflections are also calculated and acquired. The conversion from photonic power into electrical power now can be calculated, which are grouped in function "PowerSumUp", and explained below.

4.5.3 A few detailed explanations for sub-function "PowerSumUp"

After considering the coverage of solar cell surface area by bus bars and fingers, the amount of photonic power eventually entered a panel patch is obtained. Group panel patches into solar cells accordingly gives photonic powers received by each solar cell from front and rear sides.

Since the design has different area coverage ratios for solar cell front and rear side, the ratios are multiplied separately. Also, a bifaciality factor is multiplied to the rear side. Provided by the manufacturer, bifaciality value of 0.95 is used here. The conversion ratio from photonic power into number of excitons under standard testing condition is obtained with assumption of an AM 1.5 spectrum, and a good quality mono-crystalline silicon solar cell simulation result. However, it is easy to achieve and adjust without any change of the algorithm in this simulation, though.

Taking the actual solar cell working temperature from above into consideration, the actual short circuit current for each solar cell can be obtained using eq. (3.18). Combined with the open circuit voltage thermal coefficient from eq.(3.19), as well as the regressed dark current at standard test condition, the dark current at any working temperature and voltage level may be calculated using eq. (3.21). Further with the regressed series and shunt resistances and ideality factor, the actual I-V curve for each solar cell now can be obtained.

Summing up these solar cell I-V curves along voltage gives the total I-V curve of the panel. Then find the max power point on the panel total I-V curve gives the output power of the whole panel at each time stamp. The calculation flow chart is shown in Figure 48. Multiply the time stamp span (3600 seconds) gives the energy output of each time stamp.

In case the sun is below horizon with non-zero DHI, the power conversion is the same except there are fewer power items in the summation.

Finally, sum up output energy at each hourly time stamp gives the annual energy yield.

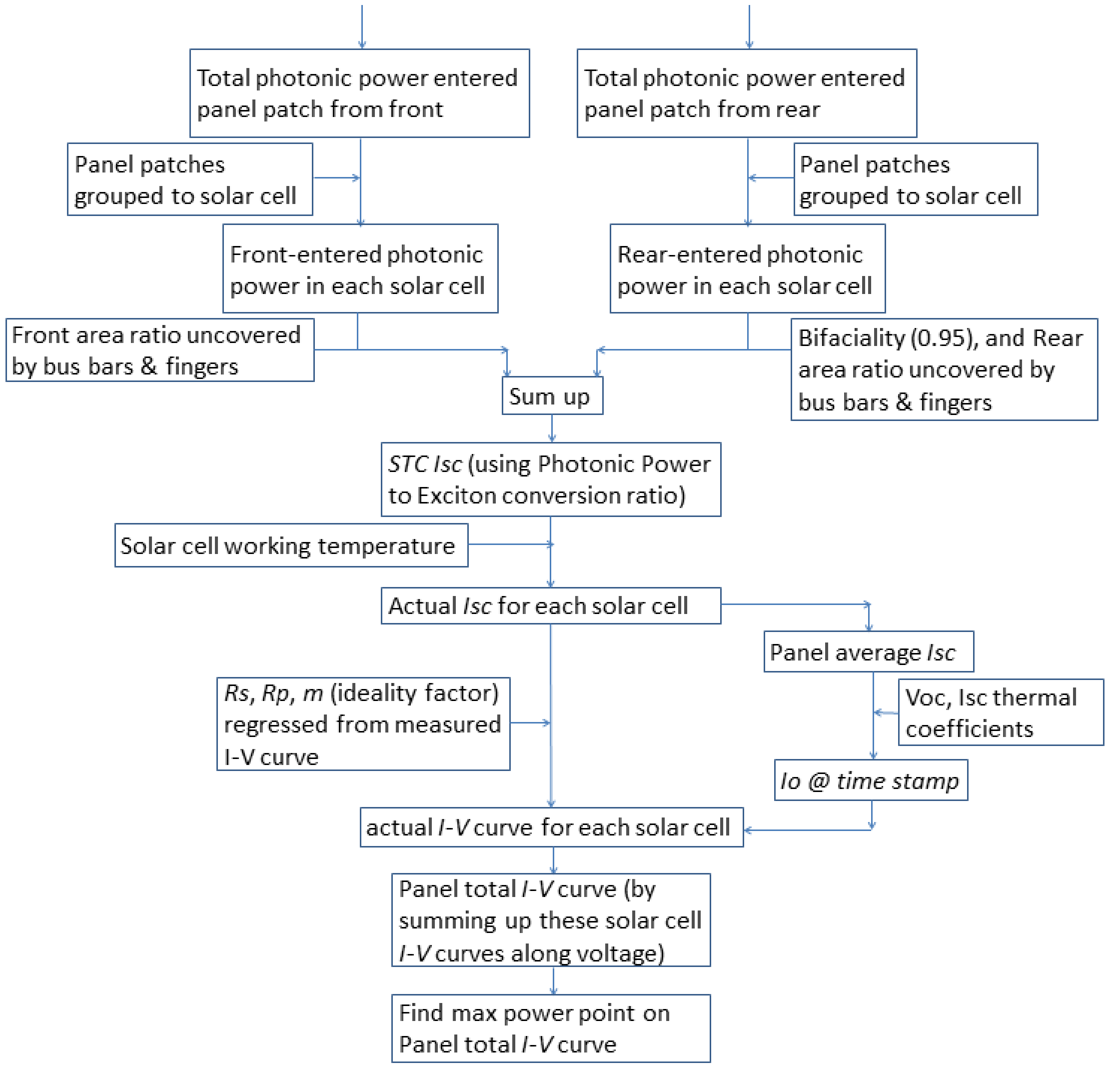

Figure 48 Flow chart of conversion from photonic power entered silicon into panel electrical output

Chapter 5 Result Analysis and Discussions

5.1 Model quality checks

Any model contains simplifications, and approximations, however, the total error should be controlled within a tolerance. It is even more important for a model also to be used as a platform. Therefore, the model quality is the foremost aspect to be scrutinized.

5.1.1 Geometry related checking: sky and ground patching resolution, and panel array rotation

This section is to check the model quality. It includes a convergence test of the model's annual yield change when varying the sky patching and ground patching resolutions.

5.1.1.1 Convergence test

In the convergence test, the panel array is set at south facing, and tilt angle at 40°, clearance at 0.2 meters.

Since the panel patching is at a very high resolution comparing to the ground and sky patches, the output convergence test is set to check the output along with the sky patching and ground patching resolutions. The sky and ground patching resolutions are set as below, and a stabilizing convergent trend is seen when resolutions increase (Table 2).

Table 2 convergence test of annual yield vs. ground and sky patch dimensions

	sky patch dimensions			ground patch dimensions			Annual energy yield (kWh)	Improvement
Setting #	azimuth	elevation	# sky patches	azimuth	radial (# div)	# ground patches		
5	2.5°	2.25°	5760	2.5°	160	23040	484.6	-0.015%
4	2.5°	2.25°	5760	2.5°	80	11520	484.7	0. 44%
3	5°	4.5°	1440	5°	40	2880	482.6	0. 15%
2	10°	9°	360	10°	20	720	481.8	0. 88%
1	20°	18°	90	20°	10	180	477.6	~

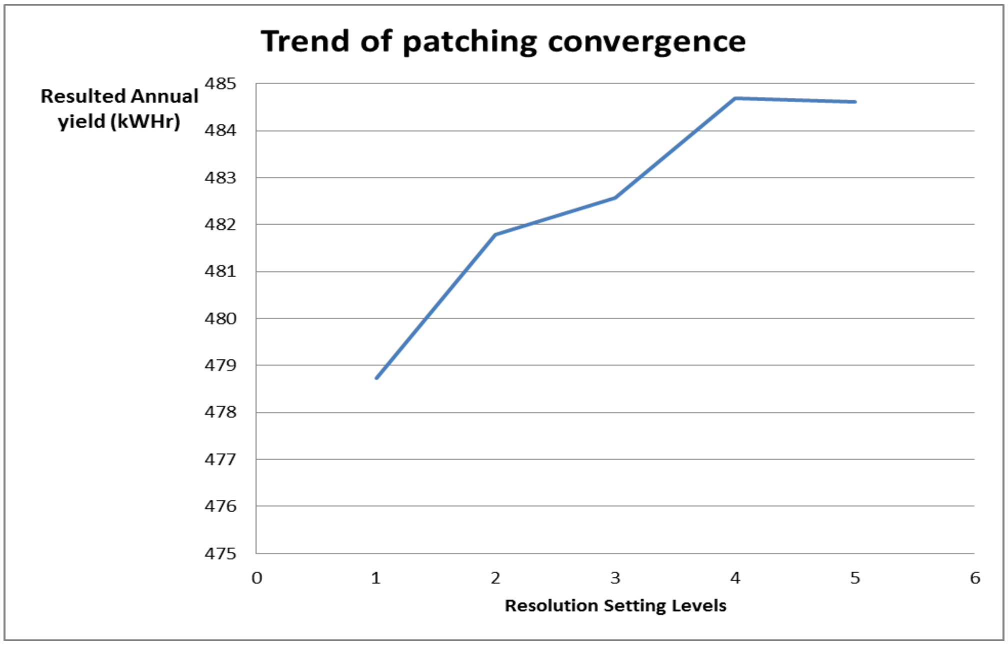

Figure 49 Convergence test: annual yield output vs. sky and ground resolutions

5.1.1.2 Patching resolutions for the most computationally economic combination

The higher the patching resolutions, the more accurate the results, however, the much more computation load. This sub-section is to investigate and determine the most computationally economic resolution combination. A very strict criterion is set to choose the lower resolution setting if next resolution increase gives an improvement significantly less than 0.1%.

The bifacial panel with racking under investigation is set as below:

Panel azimuth angle	Panel tilting angle	Clearance
0° (facing south)	40° (choose it as a whole numbered angle close to the optimal)	0.2 m (a very low clearance therefore, prone to a high simulation error, especially at low resolution)

1. Starting with the lowest sky and ground patching resolution settings, then increasing the ground radial resolution and check the corresponding annual yield as shown below. Therefore, the most economic ground radial patching should be of 20 divisions:

Sky patching	Ground patching	Annual yield	Improvement
18(azm)*5(elev)	18(azm)*10(radial)	456.97 (kWh)	~
18(azm)*5(elev)	18(azm)*20(radial)	458.80 (kWh)	0.401%
18(azm)*5(elev)	18(azm)*40(radial)	458.97 (kWh)	0.036%

2. Based on ground radial patching of 20 divisions from above, and vary the sky dome elevation division from 5 to 10, i.e. corresponding dimension changing from 18° to 9°. The corresponding annual yield are shown below, and the division is chosen to be 10:

Sky dome patching	Ground patching	annual yield	Improvement
18(azm)*5(elev)	18(azm)*20(radial)	458.80 (kWh)	~
18(azm)*10(elev)	18(azm)*20(radial)	459.23 (kWh)	0.093%
18(azm)*20(elev)	18(azm)*20(radial)	459.29 (kWh)	0.014%

3. Based on ground radial patching of 20 divisions, and sky dome elevation division of 10, now choosing to vary the sky dome azimuth division at 18, and 36, the improvement is only 0.0095%. Therefore, choose sky azimuth division at 18.

Sky dome patching	Ground patching	annual yield	Improvement
18(azm)*10(elev)	18(azm)*20(radial)	459.23 (kWh)	~
36(azm)*10(elev)	18(azm)*20(radial)	459.27 (kWh)	0.0095%

4. Lastly, the most economic ground patching division is determined from below:

Sky dome patching	Ground patching	annual yield	Improvement
18(azm)*10(elev)	18(azm)*20(radial)	459.23 (kWh)	~
18(azm)*10(elev)	36(azm)*20(radial)	459.24 (kWh)	0.0038%

Therefore, the most economic patching combination is as mid row in red below. It shows that when sky elevation division increases from 5 to 10, and ground radial division increases from 10 to 20, the total computation increases by factor of 400%, the improvement is about 0.5% which is significant for a high accurate simulation. However, among the simulations above, the maximum annual yield of 459.68 (kWh) is when Sky dome patching is 18(azm)*40(elev), and Ground patching is 18(azm)*20(radial). This is another 400% increase in computation load, but only have an improvement of 0.1%, which is considered as negligible in this project. Therefore, the most economic patching combination is chosen and recommended as sky azimuth 18, by elevation 10; and ground azimuth 18, by radial 20.

Sky dome patching	Ground patching	Annual yield	Improvement
18(azm)*5(elev)	18(azm)*10(radial)	456.97 (kWh)	~
18(azm)*10(elev)	18(azm)*20(radial)	459.23 (kWh)	0.495%
18(azm)*40(elev)	18(azm)*20(radial)	459.68 (kWh)	0.099%

5.1.1.3 Rotating panel to check the output change and stability

Another aspect of the simulation's reliability and stability is the variation or discrepancy when the system rotates against the coordinates. It is realized that the output fluctuation has the highest relative percentage in rear side. Therefore, this test specifically focuses on the rear side power output. The simulation model system should be considered well stable and reliable if the largest fluctuation on rear side is acceptable.

For verifying the model performance at different settings, the panel array is now intentionally set at different resolution combinations.

By rotating the panel array and racking away from facing the solar azimuth angle both to the east and to the west for 90°, the panel power output should change and makes a symmetric and smooth curve. For the front side, when moving off from the sun, the power output from panel front side should decrease, while the rear side power output should actually increase at the same time as sky region opposite to the sun is usually the darkest.

On the other hand, due to the patching as modeling approximation, the model may not provide smooth curves for such rotation; and furthermore, although the panel is set to rotate +/- 90° off the solar azimuth angle, however, the sky and ground patches do not rotate accordingly, the output curves are not necessarily symmetric neither.

For cloudy sky condition, the checking time stamp is set at 11:30AM, June 17th of Ottawa typical weather with DNI=1 (W/m^2), DHI=202(W/m^2), solar elevation angle at 68.06°, and azimuth angle at 2.02°. Since DNI is extremely small, checking is basically on sky diffuse radiance and the corresponding ground reflection. Figure 50 clearly show these above said overall trends, as well as the fluctuating error margins due to approximation.

Firstly, as expected, among these curves of different resolution combinations, the greatest fluctuation is of near +/-0.5% when the patching resolution is the lowest. Again, considering the rear side only contributes a fraction of the total power, this fluctuation is negligible in the total power output. This proves the model stability in aspect of system rotation.

Secondly, when the resolution is the lowest in the first row of Table 3, the output power curve is near 1% above the curves comparing to higher resolutions. Notice that this rear side power is a very small portion of the total in which such fluctuation is even a smaller percentage. On the other hand, however, this still indicates that there is a convergence need to consider along with computation load if a very highly accurate output is required.

Table 3 Resolution settings for panel rear side power output vs. panel azimuthal rotation under cloudy sky conditions

Sky dome patching	Ground patching	Panel tilting
18(azm)*5(elev)	18(azm)*20(radial)	45.32°
36(azm)*5(elev)	18(azm)*20(radial)	45.32°
36(azm)*5(elev)	36(azm)*20(radial)	45.32°

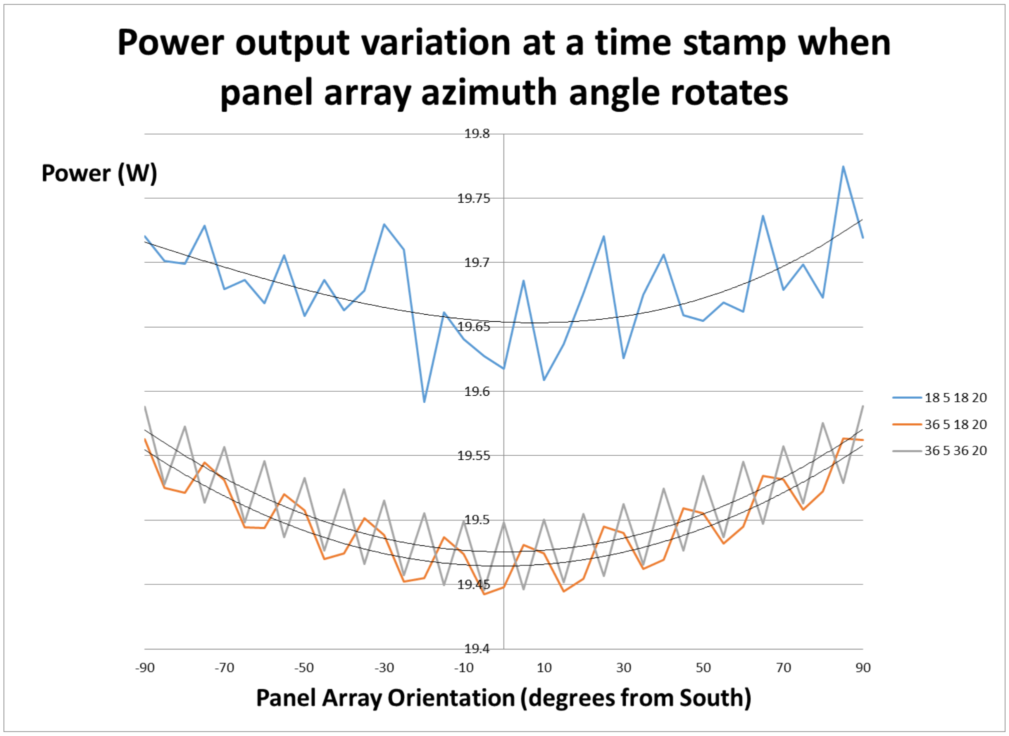

Figure 50 Panel rear side power output vs. rotation of panel array azimuth angle at cloudy noon

For a sunny sky condition, the checking time stamp is set at 11:30AM, June 14th with DNI=818 (W/m^2), DHI=166(W/m^2), solar elevation angle at 67.94°, and azimuth angle at 1.63°. To signify the reflection for analysis purpose, the albedo is set to a high value of 0.6. From Figure 51, it can be seen that the rear side power curve is not smooth nor exactly symmetric when the panel array is rotating. However, the DNI incidence on panel front changes smoothly when panel array rotates. Since DNI incidence on front side is dominant in this case, the total output curve is also overall very smooth (Figure 52).

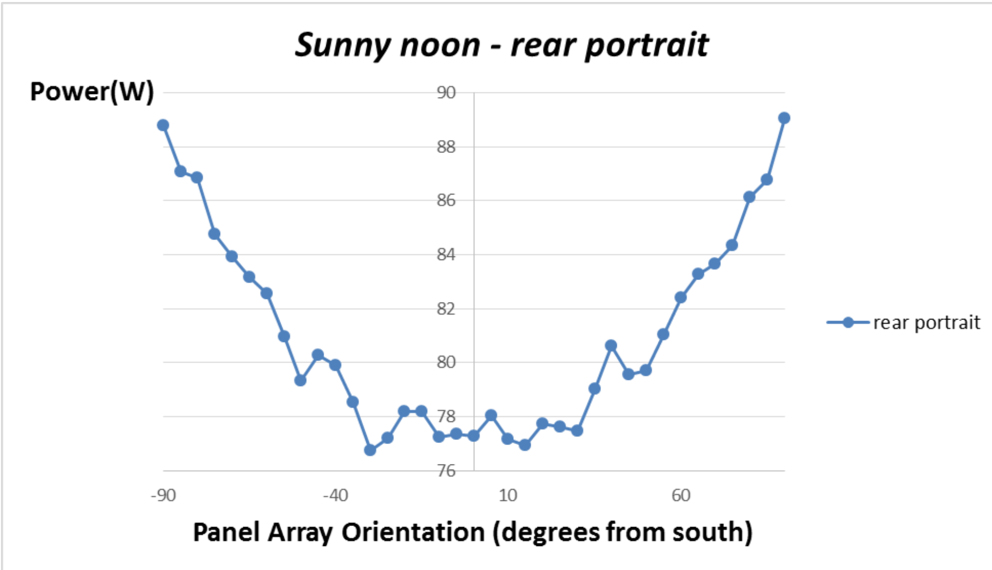

Figure 51 Panel rear side power output vs. rotation of panel array azimuth angle at sunny noon

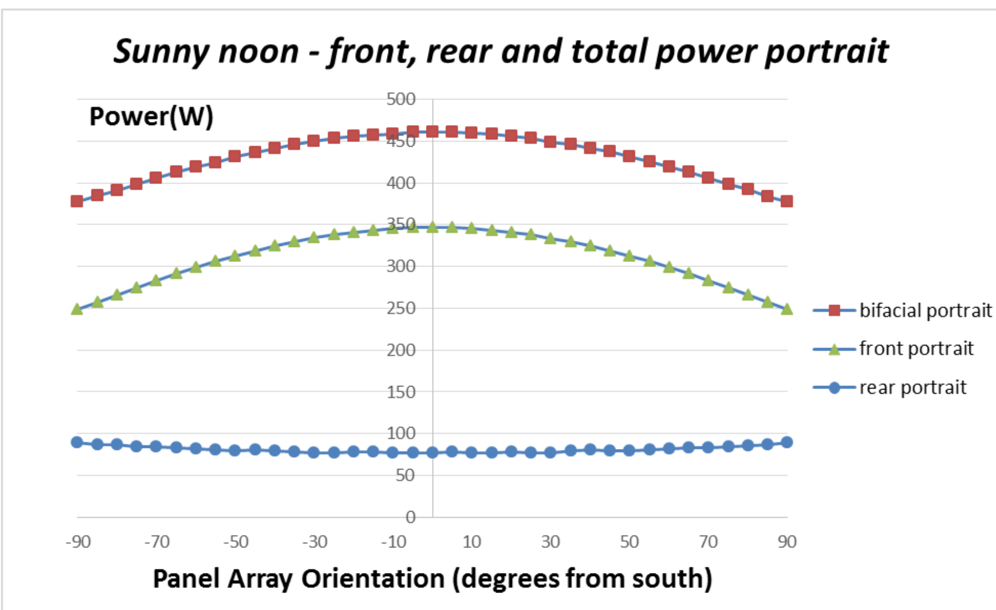

Figure 52 Panel front, rear side and total power outputs vs. rotation of panel array azimuth angle at sunny noon

All above tests show that this simulation model system is very stable and reliable.

5.1.2 Comparing results before and after compensation for Lambertian albedo

As mentioned before, for all the irradiances on panel, the ground reflection carries the largest error ratio. This is mainly due to the ground patching using a center of mass point representing a whole patch. Secondly, comparing to the sky patches, the ground patches are also close to the panel, hence the shape of the ground patches are distorted when viewed at a panel patch. Increasing ground patch resolution can reduce such error significantly, however, this increases computation time by a factor of square. Therefore, a compromised resolution with compensation(s) is determined, and compensations are introduced.

As mentioned in before, the compensation for Lambertian reflection error is done by comparing the sum up results with theoretical values. Therefore, the compensation is done with ground reflection as normalized to be unit. Here an example of the compensation effect. The panel is set facing south with latitude tilting angle of 45.32° for Ottawa, and clearance at 0.2 meter. The sum up on the front side has a distribution in left of Figure 53, after multiply it with the compensation matrix (the middle of the figure), it results an isotropic distribution exactly at the theoretical value (Figure 53). The same for the rear side (Figure 54).

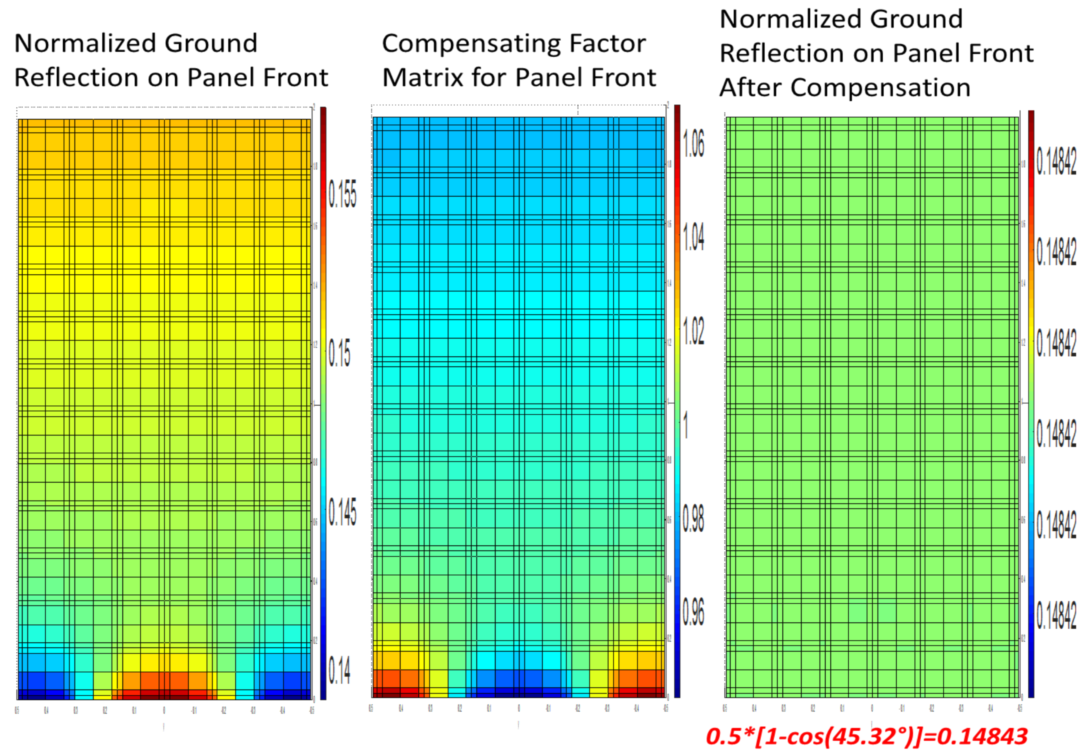

Figure 53 Normalized ground reflection sum up on panel front side and its compensation

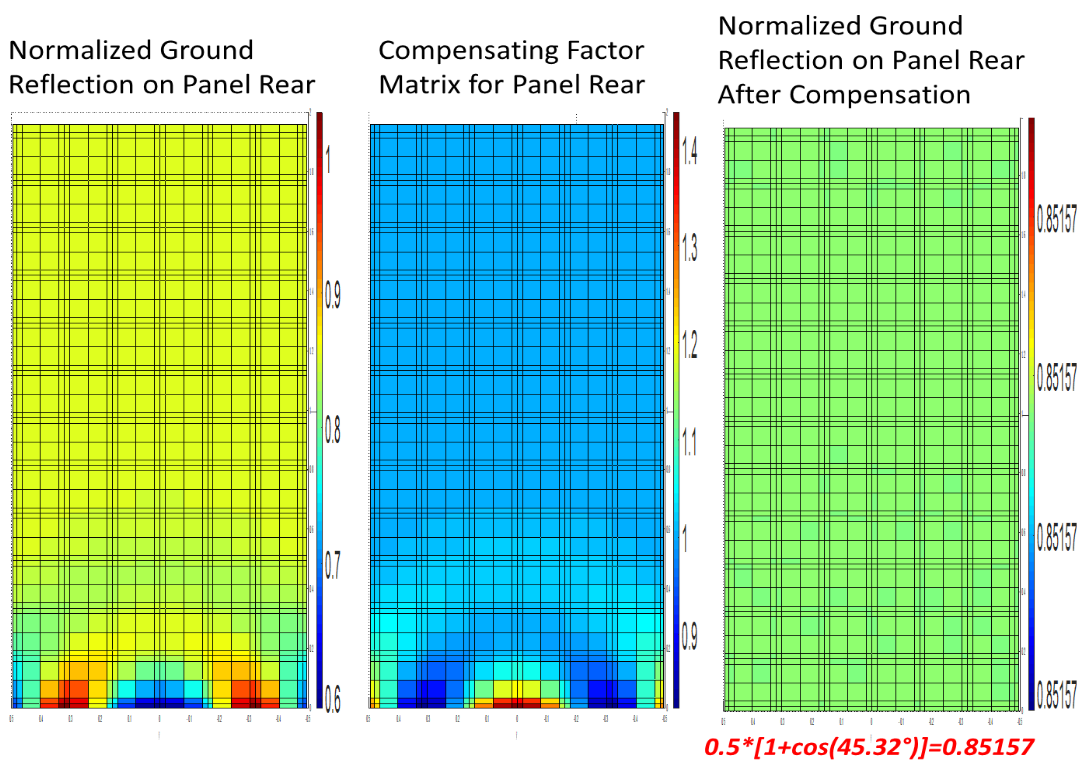

Figure 54 Normalized ground reflection sum up on panel rear side and its compensation

Above proves the effectiveness of the compensation. Furthermore, since the compensation is completely geometric, it is effective regardless of the irradiance intensity and its variation, nor the shading and blocking.

One more step to the complexity, assume the ground is isotropic in luminance, and the posts only block the reflection on way from ground to panel rear side. With such post blocking on the rear side, the sum up has a distribution containing the blocking information, as well as the error. Figure 55 shows the effect how multiplying this compensation matrix picks out the error.

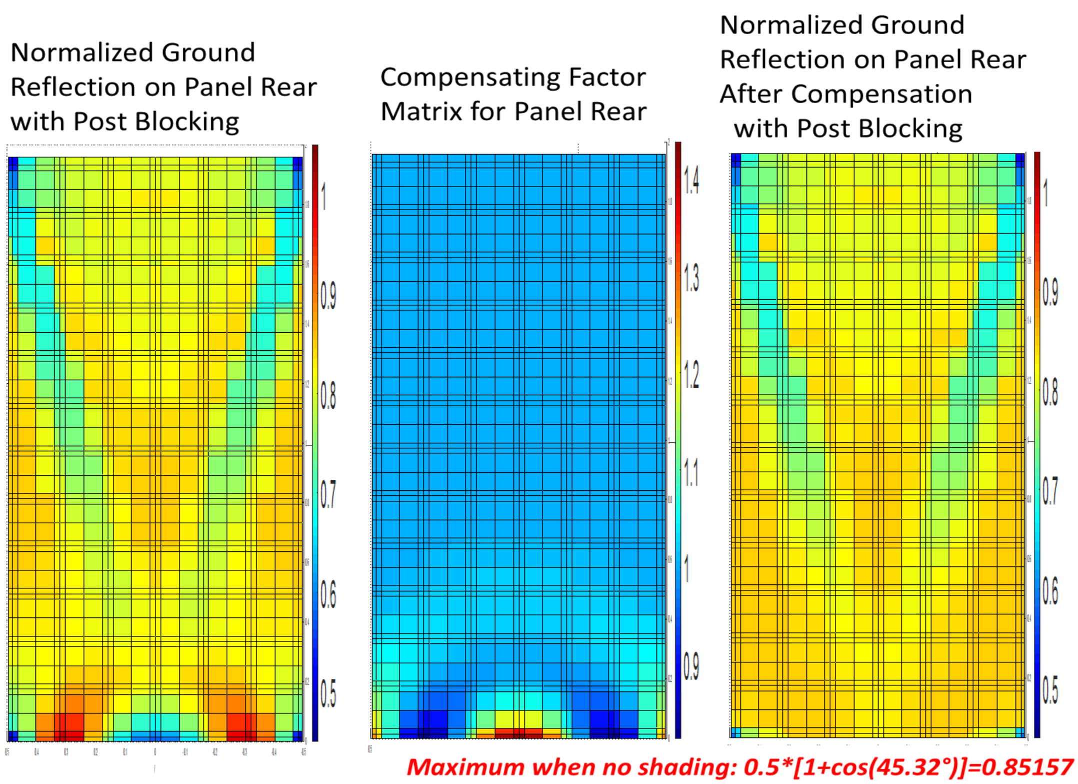

Figure 55 Apply compensation to reflection sum-up on post-shaded panel rear side

When in reality, it needs to consider both panel and post shading on the way from sky to ground and the post blocking of ground reflection onto panel rear side.

When clearance is low, the panel self-shades the ground not only under and behind itself, but also has some shading right in the front. Therefore, even the front side receives less reflection, especially the lower part receives even less, which is shown in the right side (after compensation) of Figure 56. Quantitatively, this makes the reflection received on the panel reducing from the theoretical value of 0.1484 down to 0.0921 at the panel top and 0.0887 at bottom.

As for the rear side, due to the very low clearance, the ground self-shading is severe. Overall, the upper part of rear side receives much more ground reflection than the lower part. The received maximum reflection is 0.4118 in the middle of upper edge, and the minimum is at the bottom corners due to both self-shading and part of the reflection blocked by the short post nearby. Notice that the upper corners are also darker than the rest of the upper part due to the longer post blocking, however, due to the height, the upper corners still can receive good amount of reflections, this makes them not the darkest spots (Figure 57).

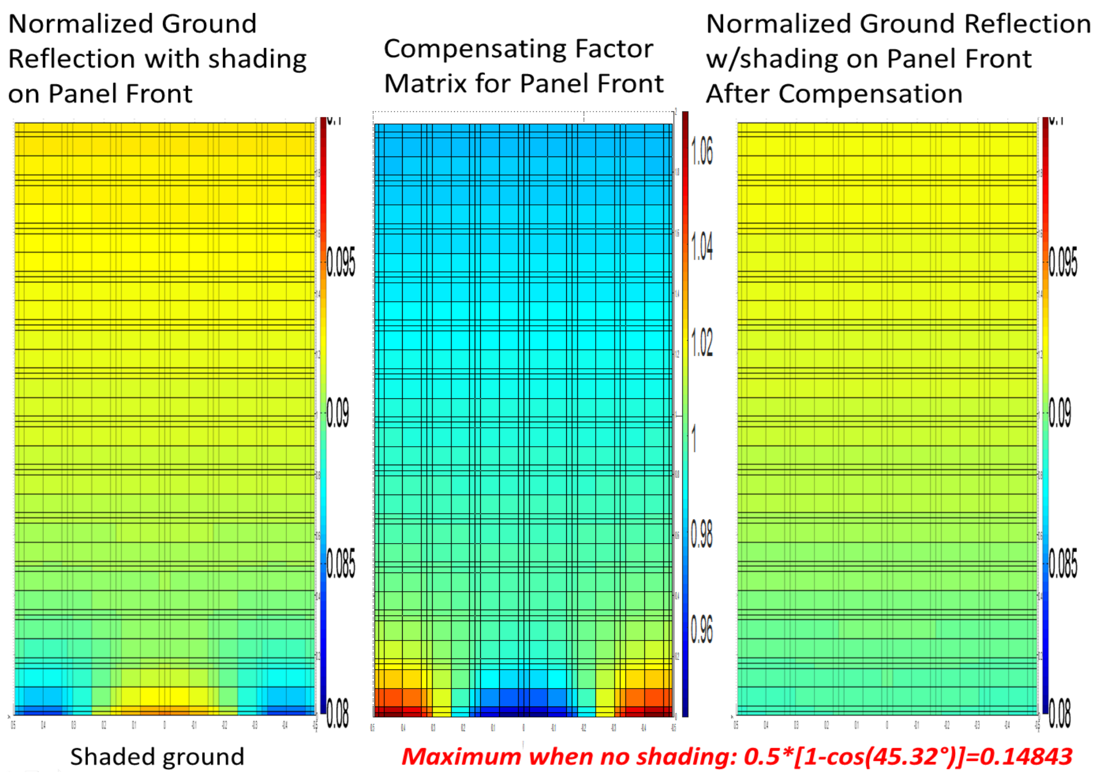

Figure 56 Compensation on panel front side with self-shaded ground reflection

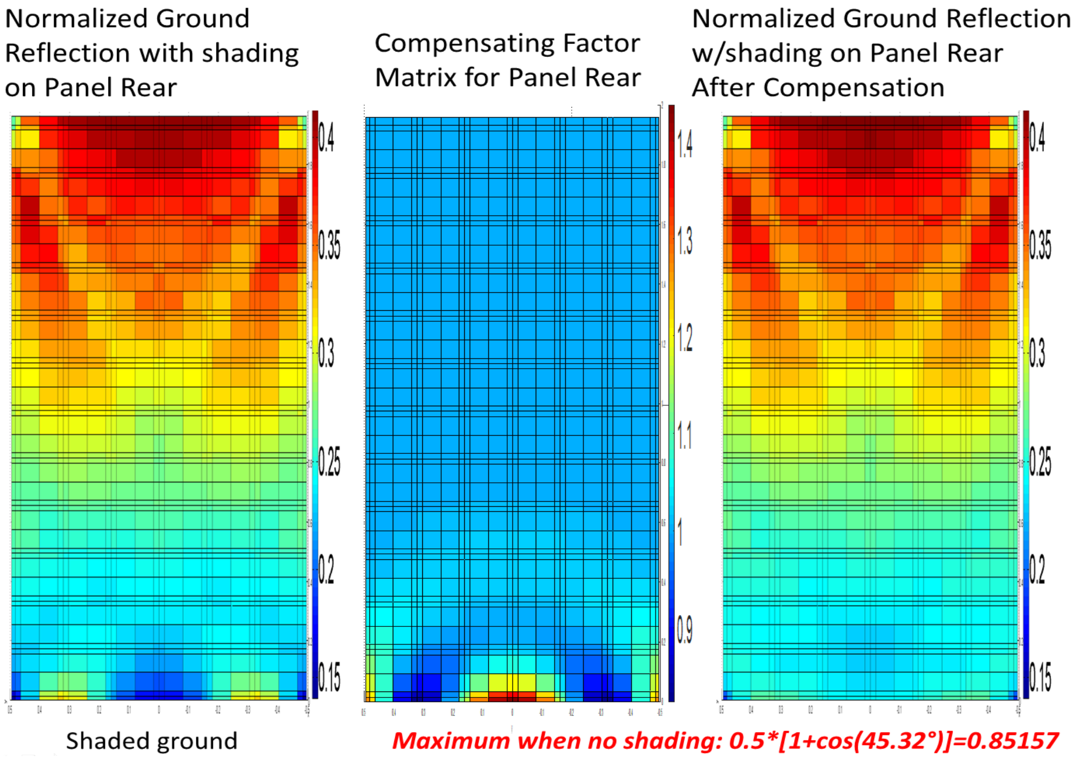

Figure 57 Compensation on panel rear side with self-shaded ground and post blocking of albedo

5.1.3 Reduction of remaining error in directional albedo after Lambertian compensation

A test is conducted to check the Lambertian compensation results, and the second step error reduction for the directional reflection. The settings and conditions are shown in table below. The changes are demonstrated in Figure 58 and Figure 59. As expected, the Lambertian compensation removes most of the artificial distribution, and the directional reflection error reduction irons out the remained artificial. Notice that the values at panel top remain practically unchanged before and after the error reduction. The values at the center of top edge changes from 3.558 (W/m^2) to 3.554(W/m^2), a -0.1% change for front side; and changes from 12.01 (W/m^2) to 12.03(W/m^2), a 0.17% change for rear side. This is a good proof that the averaging as the error reduction step only eliminates the artificial near the panel bottom but does not introduce any extra or new error in the process.

Table 4 Simulation conditions for error reduction in directional reflection at the exemplary time stamp

sky patching	18 (azimuth)*5(elevation)
ground patching	18(azimuth)*20(radial)
time	12:30PM, June 19
panel settings	South; Latitude tilting; & 0.2m
Sun zenith angle	65.31°
Sun azimuth angle	-32.28°
DNI (W/m^2)	105
DHI (W/m^2)	435

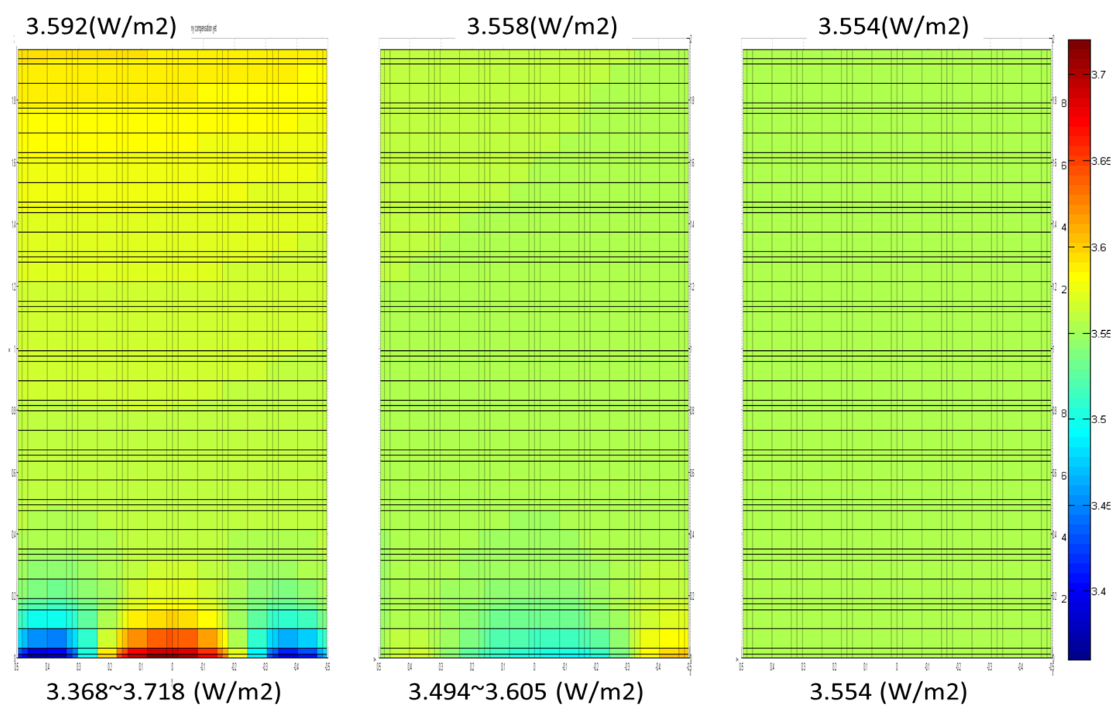

Figure 58 Two steps of compensation on front side

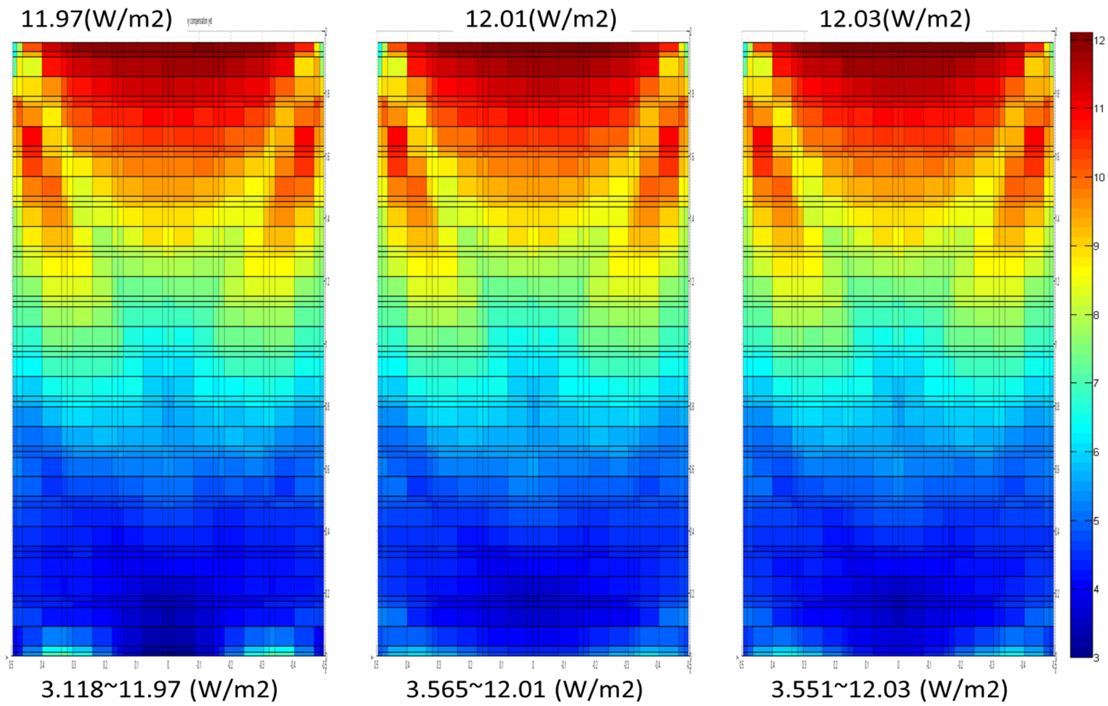

Figure 59 Two steps of compensation on rear side

Needs to point out that all the above model quality, stability and reliability tests are set at extremely error-prone conditions with very low clearance of 0.2 meter, and very low patching resolutions. The errors should be reduced rapidly when clearance increases to a usual setting of at least 0.5 meters. This guarantees simulation error is negligible when in real use.

5.2 Shading and other installation related discussions

5.2.1 Output change due to racking blocking direct beam on rear side in spring and summer early mornings and late afternoons

The impact of post blocking direct beam on rear side happens in spring and summer early mornings and late afternoons. This sub section is to investigate its impact on panel yield.

The panel array is set as south facing; latitude tilting (45.32°); and 1 meter clearance. The output gives annual energy yield 474.4 kWh. When taking out the racking for direct beam only in the simulation, so there is the direct beam on the panel rear side is not blocked, but other shadings remain. Contrary to expectations, the annual energy yield only increases to 474.8 kWh. This is a negligible 0.097% increase. This indicates that the posts casting shades of direct beam on rear side dose not significantly impact the panel annual energy yield.

This may be due to firstly, the short period of times in early morning and late afternoon when the sun is shining on the rear side; secondly, and it happens only in a fraction of a year. Moreover, when it happens, there is a very large incidence angle with relatively low DNI value at the time. This is to say that the energy output at those time stamps are small anyway even there is no post blocking.

Take an early morning time with the related parameters in Table 5 to illustrate the situation.

Table 5 Simulation conditions at an early morning time when there is a post blocking of beam on panel rear side

			Solar position (N.E.)		Incidence angle
time	DNI	DHI	elevation	azimuth	on panel rear side
5:30AM, July 10th	393(W/m^2)	64(W/m^2)	14.32°	107.30°	88.23°

Firstly, the simulation is set that all the conditions and situations as normal as in reality except there is no post blocking the beam onto panel rear side (a scenario can only be done in simulation). The rear side irradiance distribution is shown in the left of Figure 60, and the total photonic power received at each solar cell is shown in the left of Figure 61. The corresponding panel hourly energy output at the time is 0.0166 kWh. Notice that the cell receiving the least power is the one at the upper-right corner, and it is known that when solar cells are in series, the cell with the least short circuit current is the limiting cell playing the most important role in determining the panel's output, while decrease in other cells essentially does not matter.

Then, set all conditions as in reality with the posts blocking beam which gives three sharp shades onto rear side as shown on the right side of Figure 60, the shaded area near the upper right corner enlarged, which makes the cell at the corner receiving a bit even less photonic power from 1.684 (W/cell) down to 1.664 (W/cell) (right of Figure 61). This reduces the hourly output from 0.0166 kWh to 0.0165 kWh. This is a 0.6% output decrease. However, due to the small energy output, short duration of the day, and smaller fraction of a year, the total influence is less than 0.1% on annual energy yield as given above.

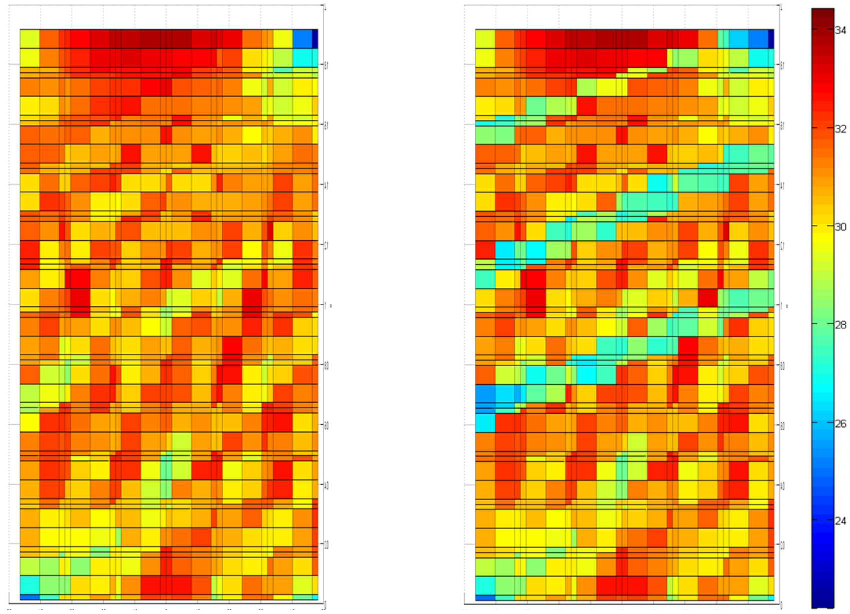

Figure 60 Comparison of patch power without or with post blocking direct beam on rear side

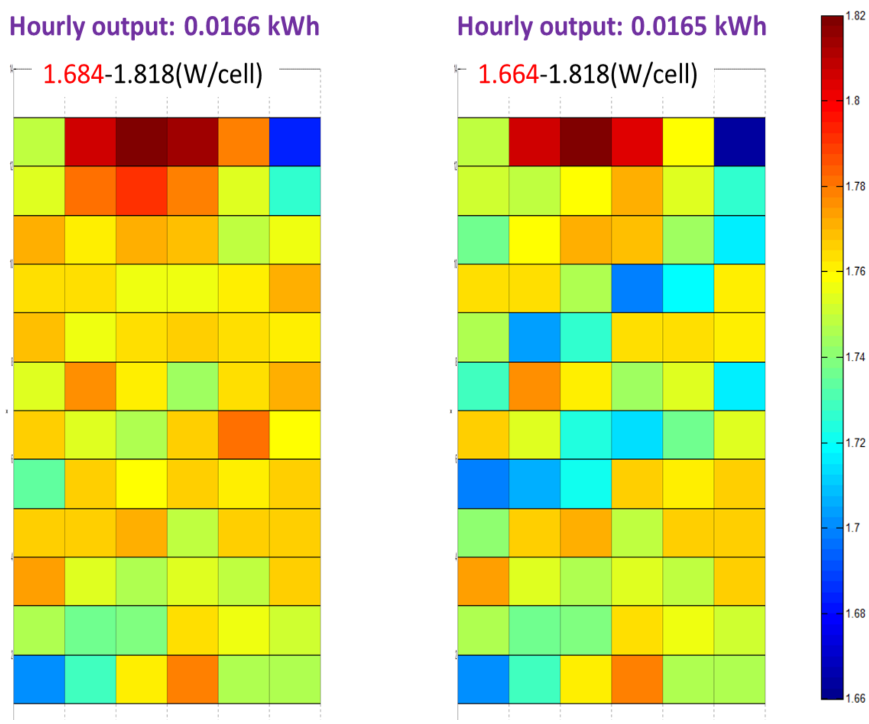

Figure 61 Comparison of solar cell power without (left) or with (right) post blocking direct beam on total power

5.2.2 Annual yield comparison between mono-facial and bifacial

For Ottawa, Ontario, when solar panel is set facing south with latitude tilt (45.32°), and 1 meter clearance, the bifacial boost is 13.44% from mono-facial 418.2 kWh to 474.4 kWh. For mono-facial, this is equivalent to a 215.5 kWh/m^2 in terms of panel area. This matches well with Haysom's PV calculation based on tests, which gives a 226 kWh/m^2 [77].

5.2.3 Impact of clearance

The solar panel self-shading is one of the main parameters of this project's investigation. Clearance impacts the self-shading significantly. Below are the relationships of panel solar cell maximum and minimum short circuit currents change vs. clearance at two days' noon time with one under sunny and another under cloudy sky conditions.

The trends can be seen that the maximum and minimum short circuit currents both increase along with clearance under both sunny and cloudy conditions, but the minimum currents increase faster than the maximum (Figure 62, and Figure 63). This is due to self-shading on the ground which induces mainly less reflection on rear side, the lower the cell, the significant the effect. When clearance increases, the self-shading effect reduces, and may eventually disappear if panel is raised high enough. Such trends have also been observed in other researches' experimental tests as shown in subsection 1.3.3.2 (Figure 5 [23] and Figure 7 [25]).

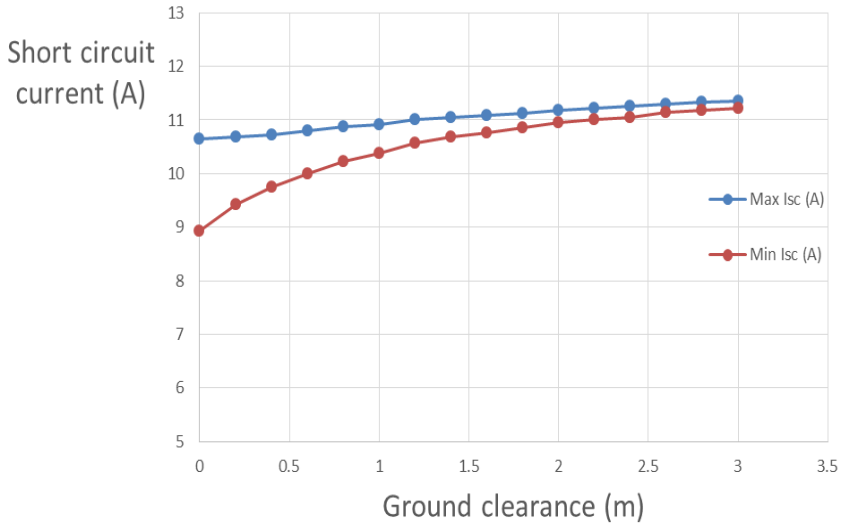

Figure 62 Effect of ground clearance on min. vs. max. short circuit currents at sunny noon

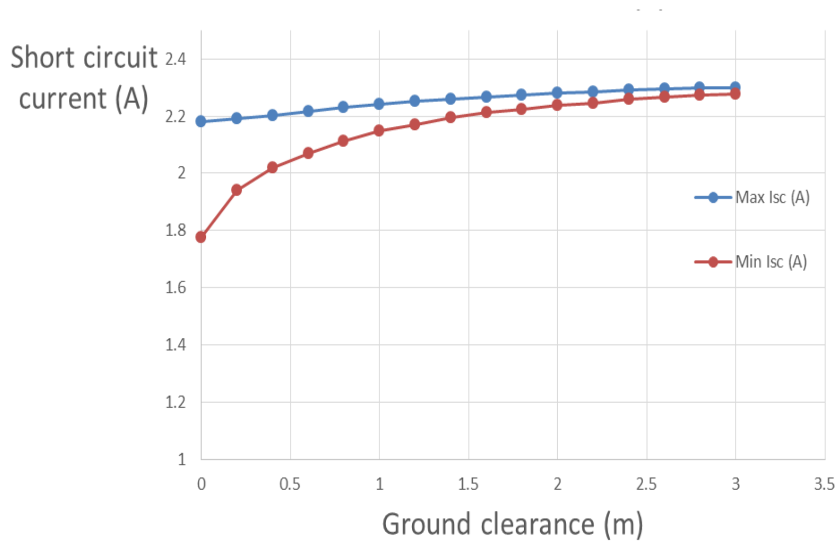

Figure 63 Effect of ground clearance on min. vs. max. short circuit currents at cloudy noon

Since the solar panel output is mainly limited by the cell with least received power, hence least short circuit current, the lower the clearance, the less the power output. In another word, when clearance is high enough and the ground shading disappears, the output would reach to its maximum. The panel is set at south facing with latitude tilting angle (45.32°), and varying clearance. The panel annual yield vs. clearance is listed in table below, and the trend is shown in Figure 64. The output increase slows down when clearance continues to increase. Since the higher the clearance, the greater the installation cost, it is possible to find out the optimal clearance with relevant market information.

Table 6 Bifacial panel annual yield vs. clearance with latitude tilting angle

Clearance (m)	0.5	1	1.5	2.5	3.5	4.5
Annual yield (kWh)	467.5	474.4	477.4	480.4	482.7	483.8

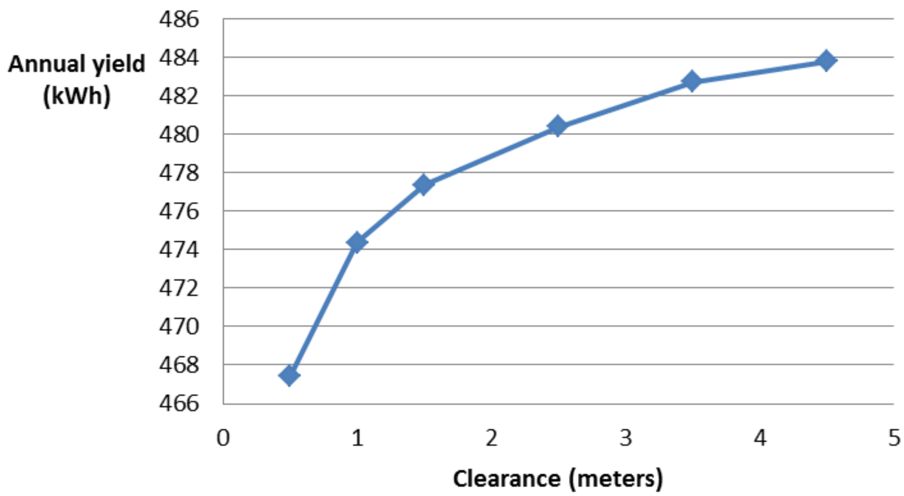

Figure 64 Bifacial panel annual yield vs. clearance with latitude tilting angle

5.2.4 Optimal tilting angle

For mono-facial flat solar panel's fixed optimal tilting angle, Siraki et al. concluded from a wide publication research that, it is expected to be smaller but close to the location's latitude for low latitude, while for higher latitude places the optimal tilt angle is even smaller. Another conclusion is that optimal tilting angle increases when albedo increases [78]. Darhmaoui and Lahjouji, regressing data from 35 Mediterranean sites, further suggested a formula for optimal tilt angle as: $\Sigma_{Opt} = 1.25351L - 0.00728944L^2$, where L is local latitude [79]. This gives the optimal tilting angle for Ottawa (Latitude 45.32°) as 41.84°. It needs to point out that a fixed optimal tilting angle should also be dependent on climate type, as well as ground reflection. Therefore, the optimal tilting angle in Ottawa may shift away from the above formula. Overall, from above, we expect a general conclusion of optimal tilting angle to be a bit smaller than local latitude.

In this simulation, when panel is set facing south with 1 meter clearance, this model gives 40° for mono-facial (Figure 65). The slightly flatter optimal setting for Ottawa comparing to the formula may be due to much more precipitation and cloudy days in winter comparing to Mediterranean region, thus it ends up with a tilt in more favor of summer time.

The optimal tilting angle is 44° for bifacial (Figure 66). Comparing to 40° of mono-facial, this may be because the higher tilting angle reduces self-shading thus increases more rear side contribution than front side loss, hence it shifts to a larger optimal angle for bifacial.

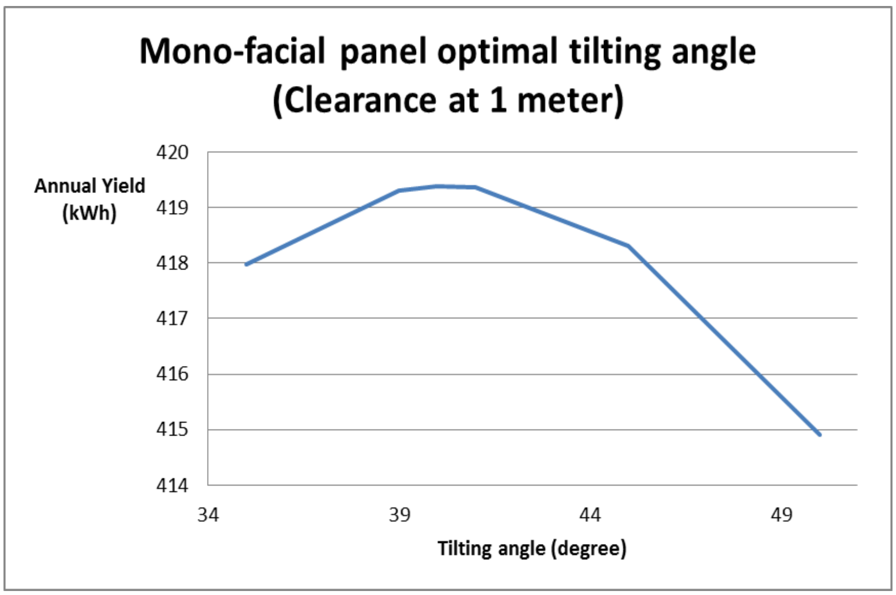

Figure 65 Finding mono-facial panel optimal tilting angle at 40° with 1 meter clearance

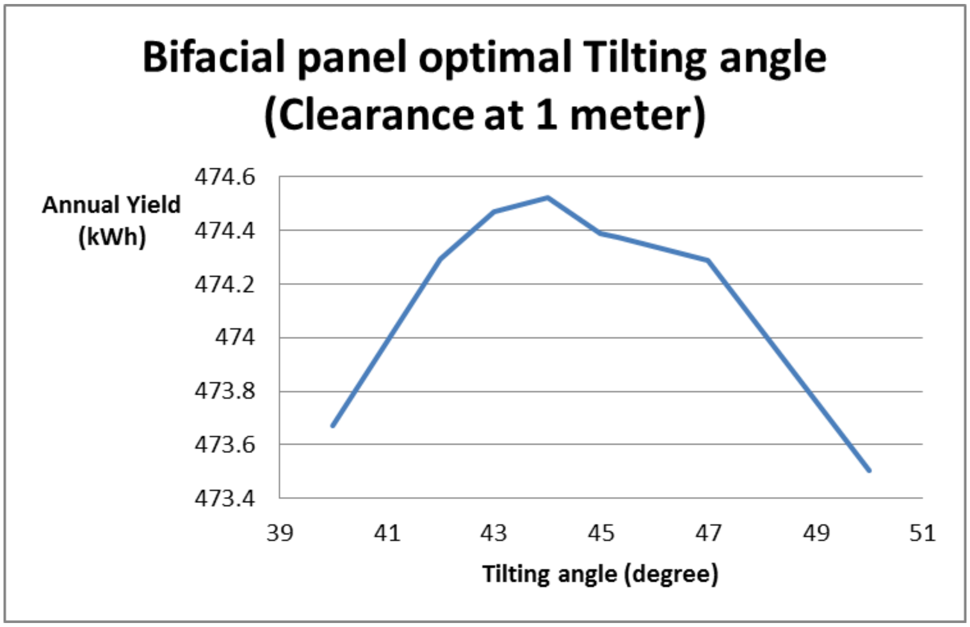

Figure 66 Finding bifacial panel optimal tilting angle at 44° with 1 meter clearance

Changing clearance would practically have no impact on mono-facial nor the front side of solar panel output unless the panel is set on or very close to ground, in which case, panel may somewhat self-shade the ground in front. However, clearance would significantly influence bifacial output, as well as the optimal tilting angle. When clearance is set at 3 meters, the bifacial optimal tilting angle shifts to 41°. This may be due to that self-shading reduces at higher clearance, hence the optimal tilting angle reverts toward that of mono-facial. However, as long as there is contribution from rear side, the optimal tilting angle will be always greater than that of mono-facial.

It needs to point out that the energy yield may not vary too much if the tilting angle is not too much off the optimal, as it can be seen in Figure 67, the annual yield only drops from 482.5 kWh to 482.3 kWh when tilting angle changes from optimal 41° to 45°. Interestingly, the dropping is less sharp when tilting angle increases from optimal, which gives a wider tolerance for installation, and a greater tilting angle is good for getting rid of dust, rain and snow.

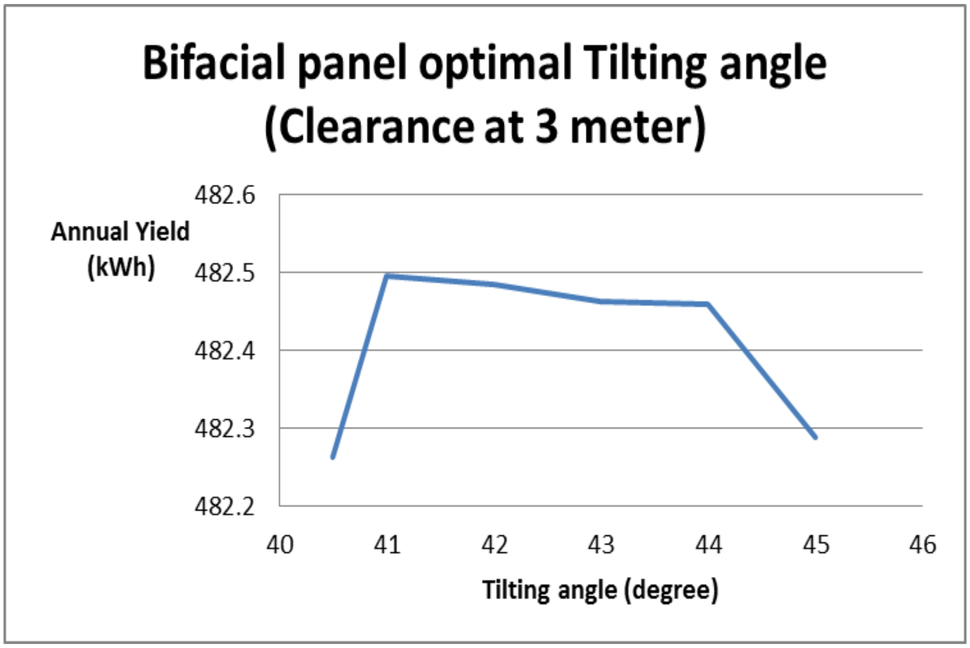

Figure 67 Finding bifacial panel optimal tilting angle at 41° with 3 meter clearance

5.2.5 East, west vertical installations, and south facing with latitude tilting

Bifacial solar panels may also be set vertical and east-west facing, which generates two output peaks in the morning and afternoon every day. Especially, the afternoon peak matches well with electricity demands in time [80]. Also, vertical setting is much better in dust preventing [81].

Singh et al. concluded that mono-facial tilting at latitude and facing south has about 10% less output than bifacial of the same setting, and bifacial set vertical and east-west facing also has a 10% less output, thus, bifacial vertical and east-west facing should provide approximately the same annual yield as that from a south facing, latitude tilting mono-facial [80]. The same conclusion is drawn by Hajjar et al. [81], and Joge et al. [82]. Needless to say that the actual result varies by case and is dependent on panel's bifaciality, and local albedo.

As the bifacial panels may be used in such way, our model is set to east-west facing and vertical to verify the outputs. Also, as at such setting, the posts in the model would block beam for a short period of time around noon time every day. Hence, the model is set to run either with or without the posts blocking. The outcomes are shown in table below. Indeed, the east-west setting's outputs are close to mono-facial south latitude tilting. The second point is that, the post shading beam on rear side happens at everyday noon time reduces the total annual yield by almost 3%. This drop is more significant comparing to the 0.1% drop in the case of post blocking beam on rear side in spring and summer early mornings and late afternoons (section 5.2.1). Another interesting observation is that front-side west-facing is about 1% greater than east facing, this might possibly be due to more cloudy morning time in Ottawa.

Table 7 Comparison of Bifacial panel annual yields at vertically East-West, West-East facing, and the impact of post blocking beam around noon; and comparison to a mono-facial at latitude tilt and south facing with clearance all set at 1 meter

Case	Tilt	Facing	Sides #	With racking posts?	Annual yield (kWh)
1	45.32°	S	bifacial	y	474.4
2	90°	E	bifacial	y	392.8
3	90°	W	bifacial	y	397.9
4	90°	E	bifacial	n	404.5
5	90°	W	bifacial	n	409.1
6	45.32°	S	mono-facial	y	418.2

Chapter 6 Conclusions and Future Work

6.1 Conclusions

First of all, although this simulation intends for North America implementation, it can be applied to anywhere in north hemisphere.

This simulation model set up a complicated scenario model with detailed consideration of various aspects.

The considerations include: a distributive sky diffuse model; a ground reflection model with seasonally varying albedo and ground material related varying directional reflection component; a real single diode solar cell model with its short circuit current; open circuit voltage and dark current all temperature-related; panel optical transfer functions separately for cells and for transmitting through toward ground; panel self-shading on ground; racking shading ground, blocking radiance from sky as well as ground albedo towards panel rear side; the panels can also be set at any combination of a tilting angle from 0° (horizontal) to 90° (vertical), and an azimuth angle from 90° to 0° to -90° i.e. east-south-west.

From to-date researches, there has no specific solar panel field simulation model dealing with bifacial solar panel scenarios to such complexity.

From simulation tests in Chapter 5, the model simulations show very good stability and reliability, and the annual output for Ottawa agrees well with other people's research and measured data [77]. Further specific validation experimental tests may be conducted in near future.

More conclusions detailed in specific aspects are listed below:

- Contrary to expectations, the posts casting shades of direct beam on rear side dose not significantly impact the panel annual energy yield.
- The bifacial boosts about 13% of annual yield from mono-facial solar panel of the same quality when set south facing, latitude tilt and 1 meter clearance.

- The amount of boost is clearance dependent. This is because self-shading mainly reduces photonic power received on rear side of cells, and reduction of their short circuit currents accordingly, especially the ones near the ground, where the least one becomes the limiting cell. The higher the clearance, the less of such reduction, the greater the bifacial boost.
- Based on this simulation, in Ottawa, optimal tilting angle for a mono-facial solar panel is about 4° smaller than latitude. The optimal tilting angle for a bifacial panel is greater than that of mono-facial. Moreover, bifacial optimal tilting angle converges down to that of mono-facial when self-shading impact reduces by clearance increase.

The simulation model may be also used as a platform, more analysis may be executed in the future, and also more performance and functionalities may be built upon.

6.2 Future work

6.2.1 Further investigation topics based on the existing model

Based on the existing model, further investigation topics may include but not limited to the following:

- A detailed bifacial solar cell model based on its physics working principles;
- Solar cell texture is an important feature in solar cell in-take photons from non-normal incidence;
- Panel and cell internal reflection is an important factor in photon absorption thus increase output;
- Investigation on various racking design, impacts on panel performance and optimization;
- Investigation on racking surface reflection;
- Panel set-up variations, such as comparison between portrait and landscape;
- Various combinations of series and parallel wiring on a panel instead of all cells wired in series;

- The ground in this simulation so far is simply set as flat and seasonal albedo in Ottawa is arbitrarily assigned as 100% grass ground from May 1st to October 31st; 75% grass and 25% snow for March, April and November; and 50% grass, 50% snow for December, January, and February. Introducing real observed/measured data in the future may provide a yield more trustworthy;
- In winter, cumulated snow may reduce the de facto clearance. It may give a more accurate output result if a varying clearance is modeled based on measured snow depth.

6.2.2 Further development on this model

First of all, Gueymard's directional reflection model contains forward and backward anisotropic coefficients. The values of these coefficients for various ground types are assigned with rough estimation. It may increase the software quality if accurately measured such coefficient values are available or will there be better and more suitable reflection model for the simulation.

As this model system can be used as a platform, further development based on it is possible, and directions for development on this model system may be but not limited to adding more panels and rows to simulate solar farm scenarios; and including spectral information of the sources.

6.2.2.1 Add more panels and more rows to simulate solar farm scenario

In solar farms, the real amount of ground reflection, due to inter-shading from bifacial panel arrays, is important in determining the optimal location and distance of these arrays. The other related factors may also include tilting angle, and clearance. Although it is possible to get certain expressions for energy output vs. the geometric parameters, the optimal values may not be determinable only by geometry and physics, instead, it may be determined only when land, panel, racking and electricity par prices are also known.

6.2.2.2 Spectral information of all sources

In photovoltaics, photonic sources' spectrum is an important factor in solar panel optical transmission, solar cell photon absorption, and quantum efficiency. Spectrums of solar beam and sky diffuse irradiances vary all the time, even at the same time, sky diffuse spectrum varies spatially. Reflection from various ground surfaces introduces a spectral bias which can also change solar cell output. Despite the importance, however, introducing spectrum into simulation may enormously increase computation load. A solution may be using a few key wave lengths with weighted photonic power representing different spectral conditions, which as an idea is similar to that used in the referred project conducted by Tatsiankou et al. [83]. This way, the model may deal well with whole spectral analysis with only a few times more of computation load.

Appendix A Perez 1993 model coefficients for irradiance

Table 8 Perez 1993 model coefficients for irradiance

sky	Overcast							Clear
ε bins	1	2	3	4	5	6	7	8
a1	1.3525	-1.2219	-1.1	-0.5484	-0.6	-1.0156	-1	-1.05
a2	-0.2576	-0.773	-0.2515	-0.6654	-0.3566	-0.367	0.0211	0.0289
a3	-0.269	1.4148	0.8952	-0.2672	-2.5	1.0078	0.5025	0.426
a4	-1.4366	1.1016	0.0156	0.7117	2.325	1.4051	-0.5119	0.359
b1	-0.767	-0.2054	0.2782	0.7234	0.2937	0.2875	-0.3	-0.325
b2	0.0007	0.0367	-0.1812	-0.6219	0.0496	-0.5328	0.1922	0.1156
b3	1.2734	-3.9128	-4.5	-5.6812	-5.6812	-3.85	0.7023	0.7781
b4	-0.1233	0.9156	1.1766	2.6297	1.8415	3.375	-1.6317	0.0025
c1	2.8	6.975	24.7219	33.3389	21	14	19	31.0625
c2	0.6004	0.1774	-13.0812	-18.3	-4.7656	-0.9999	-5	-14.5
c3	1.2375	6.4477	-37.7	-62.25	-21.5906	-7.1406	1.2438	-46.1148
c4	1	-0.1239	34.8438	52.0781	7.2492	7.5469	-1.9094	55.375
d1	1.8734	-1.5798	-5	-3.5	-3.5	-3.4	-4	-7.2312
d2	0.6297	-0.5081	1.5218	0.0016	-0.1554	-0.1078	0.025	0.405
d3	0.9738	-1.7812	3.9229	1.1477	1.4062	-1.075	0.3844	13.35
d4	0.2809	0.108	-2.6204	0.1062	0.3988	1.5702	0.2656	0.6234
e1	0.0356	0.2624	-0.0156	0.4659	0.0032	-0.0672	1.0468	1.5
e2	-0.1246	0.0672	0.1597	-0.3296	0.0766	0.4016	-0.3788	-0.6426
e3	-0.5718	-0.219	0.4199	-0.0876	-0.0656	0.3017	-2.4517	1.8564
e4	0.9938	-0.4285	-0.5562	-0.0329	-0.1294	-0.4844	1.4656	0.5636
az	40.86	26.58	19.34	13.25	14.47	19.76	28.39	42.91
bz	26.77	14.73	2.28	-1.39	-5.09	-3.88	-9.67	-19.62
cz	-29.59	58.46	100	124.79	160.09	154.61	151.58	130.8
dz	-45.75	-21.25	0.25	15.66	9.13	-19.21	-69.39	-164.08

Appendix B Detailed description on Gueymard's reflection model

Gueymard et al. defined a few reflectance indices:

ρ : usually reported mean daily albedo;

ρ_d : diffuse reflectance, which is "almost" equal to ρ ;

ρ_n : reflectance to a normal incidence beam, assumed pure isotropic;

ρ_b : reflectance to a beam of any incidence angle.

Since ρ is usually given, and thus the value of ρ_d is known. Therefore, from formula derived through integration, Gueymard provides a way to obtain ρ_n from ρ_d : $\rho_n = \rho_d - 0.023(\mathrm{f}_{ab} + \mathrm{f}_{af})$, and therefore:

$$\rho_b = \rho_n + F(\mathrm{f}_{\mathrm{ab}}, \mathrm{f}_{\mathrm{af}})\,\mathrm{G}(\gamma)\,\mathrm{H}(\beta_S) = \rho_d - 0.023(\mathrm{f}_{ab} + \mathrm{f}_{af}) + F(\mathrm{f}_{\mathrm{ab}}, \mathrm{f}_{\mathrm{af}})\,\mathrm{G}(\gamma)\,\mathrm{H}(\beta_S) \qquad \text{(\#B1)}$$

Where f_{ab} and f_{af} are values for a few most common ground types as tabulated below. And γ is the horizontal angle between incidence and reflection.

$F(\mathrm{f}_{\mathrm{ab}}, \mathrm{f}_{\mathrm{af}}) = \delta_\gamma\, \mathrm{f}_{\mathrm{af}} + (1 - \delta_\gamma)\,\mathrm{f}_{\mathrm{ab}}$, where $\delta_\gamma = 1$ if $\cos\gamma > 0$, and $\delta_\gamma = 0$ otherwise;

$\mathrm{G}(\gamma) = \cos\gamma$;

$\mathrm{G}(\gamma)$ is the azimuth deviation between the sun beam and the receiving direction. Due to the ellipsoidal pattern of the directional reflection, $\mathrm{G}(\gamma) = \cos\gamma$ only when reflection is on horizontal plane. However, when dealing with a reflected ray at the azimuth deviation direction but with an elevation angle β, then $\mathrm{G}(\gamma) = \cos\left\{\arcsin\left[\cos(\beta)\sin(\gamma)\right]\right\}$; and:

$\mathrm{H}(\beta_S) = e^{-1.77-1.53\beta'-3.61(\beta')^2} = e^{-1.77-1.53\times\left(\frac{\beta_S}{100}\right)-3.61\times\left(\frac{\beta_S}{100}\right)^2}$, where $\beta' = 0.01\beta_S$, for β_S is the source elevation angle in *degree*, and it is named as β_S in this project for the sun is the only source for directional albedo. The final expression for general beam reflectance is:

$$\rho_b = [\rho_d - 0.023(\mathrm{f}_{ab} + \mathrm{f}_{af})] + [\delta_\gamma \mathrm{f}_{\mathrm{af}} + (1-\delta_\gamma)\mathrm{f}_{\mathrm{ab}}]\cos\left\{\arcsin\left[\cos(\beta)\sin(\gamma)\right]\right\} \mathrm{e}^{-1.77-1.53(\frac{\beta_S}{100})-3.61(\frac{\beta_S}{100})^2} \quad \text{(\#B2)}$$

The values of ρ or ρ_d for various ground types are shown in below.

Table 9 Values of the anisotropy coefficients for typical reflecting surfaces [34]

Surface	fab	faf
Lawn, green grass	1	1
Fresh snow	0	2
Plowed field	1	0
Pasture land	0.5	0.5
Concrete	0.3	0.3

For in Ottawa, we arbitrarily assume that the ground on a solar farm is lawn for summer and early autumn. i.e. 6 months covering May to October, with albedo assumed to be 0.2, and corresponding f_{ab}=1, f_{af}=1; three months 50% snow covering over December to February, with snow albedo assumed to be 0.6 [69], hence averaged albedo to be 0.4, with corresponding averaged f_{ab}=0.5, f_{af}=1.5; and November, March and April as 25% snow, 75% grass, averaged albedo to be 0.3 with corresponding averaged f_{ab}=0.75, f_{af}=1.25. These modeling data are listed in table below.

Table 10 Albedo forward and backward anisotropy factors for Gueymard model

	Ground types, albedo and		Model albedo	Model f_{ab}	Model f_{af}
Month	Grass (0.2)	Snow (0.6)			
Jan	50%	50%	0.4	0.5	1.5
Feb	50%	50%	0.4	0.5	1.5
Mar	75%	25%	0.3	0.75	1.25
Apr	75%	25%	0.3	0.75	1.25
May	100%	0%	0.2	1	1
June	100%	0%	0.2	1	1
July	100%	0%	0.2	1	1
Aug	100%	0%	0.2	1	1
Sept	100%	0%	0.2	1	1
Oct	100%	0%	0.2	1	1
Nov	75%	25%	0.3	0.75	1.25
Dec	50%	50%	0.4	0.5	1.5

Power-wise analysis for reflection in general and in Gueymard's Model

By albedo definition [47], for a normal incidence of irradiance I(W/m^2) with surface reflection being isotropic, if the reflected radiance is L_n at the surface normal direction, and $L(\mathrm{Z_r}) = L_n \cos\mathrm{Z_r}$ at any reflecting angle $\mathrm{Z_r}$, hence cos(Z_r) is the ***cosine factor*** for a reflected ray off the horizontal plane toward a panel patch direction. The diffuse reflectance is then:

$$\rho_d = \frac{\int_0^{\pi/2} L_n \cos\mathrm{Z_r} \sin\mathrm{Z_r}\, d\,\mathrm{Z_r} \int_0^{2\pi} d\varphi}{I} = \frac{\pi L_n}{I}$$, therefore,

$$L_n = \frac{\rho_d}{\pi} I (\mathrm{W/sr/m^2}) \quad \text{(\#B3)}$$

When incidence coming with an angle, the effective area becomes smaller, therefore less radiance: $L_n = \frac{\rho_d}{\pi} I \cdot \cos(Z)(\mathrm{W/sr/m^2})$, where Z is the zenith angle of the source (If the source is the sun, then the angle should be Z_S, and I should become DNI). The reflection radiance at an angle Z_r to the reflecting plane (ground) normal is:

$$L(\mathrm{Z_r}) = \frac{\rho_d}{\pi} I \cdot \cos(Z_S)\cos(\mathrm{Z_r}) \quad \text{(\#B4)}$$

Where $\cos(Z_S)$ is the cosine factor for a ray incidence on a horizontal plane.

When the incidence is the sun beam and the reflection to beam is considered anisotropic, ρ_d should be replaced by ρ_b , and the reflection at an angle Z_r to the reflecting plane normal is:

$$L(\mathrm{Z_r}) = \frac{[\rho_d - 0.023(\mathrm{f}_{ab} + \mathrm{f}_{af})] + [\delta_\gamma \, \mathrm{f_{af}} + (1-\delta_\gamma)\,\mathrm{f_{ab}}]G(\gamma)\,\mathrm{e}^{-1.77-1.53(\frac{\beta_S}{100})-3.61(\frac{\beta_S}{100})^2}}{\pi} I\cos(Z_S)\cos(\mathrm{Z_r}) \quad (\#B5)$$

Thus the radiant flux from this ground patch and reaches the panel patch may be expressed as:

$$\Phi(\mathrm{Z_r}) = \frac{[\rho_d - 0.023(\mathrm{f}_{ab} + \mathrm{f}_{af})] + [\delta_\gamma \, \mathrm{f_{af}} + (1-\delta_\gamma)\,\mathrm{f_{ab}}]G(\gamma)\,\mathrm{e}^{-1.77-1.53(\frac{\beta_S}{100})-3.61(\frac{\beta_S}{100})^2}}{\pi} DNI \bullet \cos(Z_S) \bullet \Omega_{GpPp}[A_{Pp}\cos(\theta_{GpPp})](\mathrm{W}) \quad (\#B6)$$

Where Ω_{GpPp} is the solid angle for a ground patch seen from center of the panel patch, and $A_{Pp}\cos(\theta_{GpPp})$ is the effective panel patch area facing the field ground patch center.

The solid angle of ground patches seen from panel patch

In this model, as sky radiance receiver and reflector, the ground is also divided into patches by divisions in azimuth and radius with the coordinate origin (x_O, y_O, z_O) where (x_O, y_O) is set at the bottom central point of the panel under investigation, and z_O is simply set on ground (Figure 17).

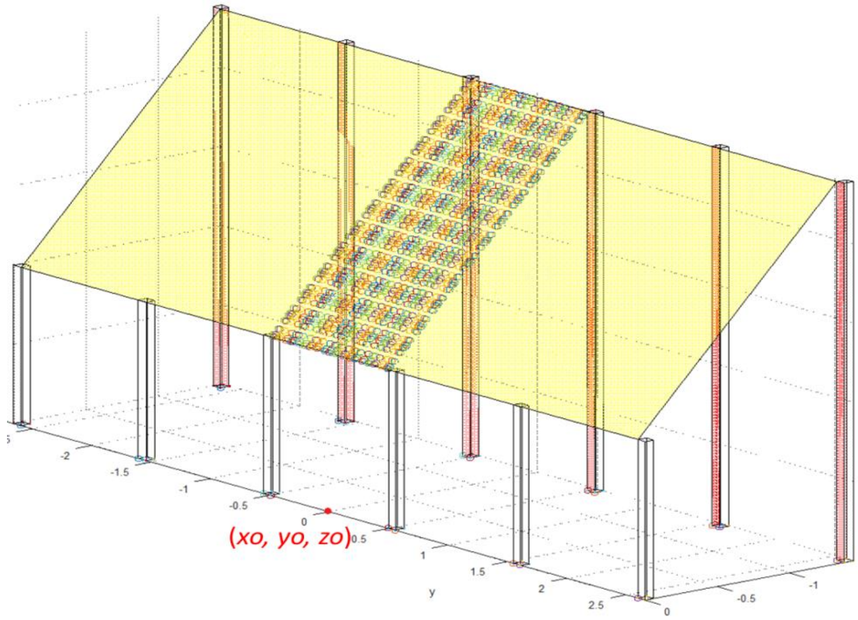

Figure 68 Panels, racking and coordinate origin

The definition of solid angle is: $\Omega = \frac{A}{r^2}(Sr)$, where A is the surface area of the spherical cap, $2\pi rh$; r is the radius of the sphere; h is the height of the cap; and Sr is the unit, steradian.

a. solid angle of far field band

The solid angle of the farthest circular band (far field band as well as far field patches) may be expressed as: $\Omega_{GfBand} = 2\pi \bullet \sin(\beta_{Gfp.in})$. where $\beta_{Gfp.in}$, as shown in Figure 69, is the elevation angle from the far field band inner ring toward a panel patch center:

$\beta_{Gfp.in} = \text{atan}(\frac{h_{Pp}}{d_{Gfp.in}})$ where h_{Pp} is the corresponding panel patch center height above ground, and $d_{Gfp.in}$ is the far field band inner ring radius. The solid angle for one patch on this farthest (outermost) field band may be: $\Omega_{Gfp} = \frac{2\pi \bullet \sin(\beta_{Gfp.in})}{N_{GAzD}}$, where subscript *GAzD* is for ground azimuth division.

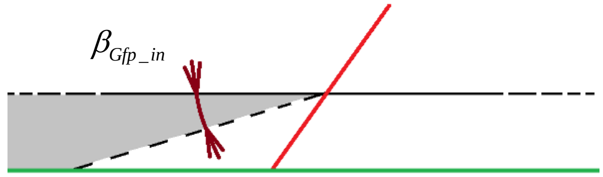

Figure 69 Solid angle of far field band seen from panel

The far field patch center radius may be defined by half value of β_{Gfp_in}. Therefore, the incident angle from such far field patch center toward panel patch center may be calculated as:

$$\theta_{GfpPp} = \arccos\left[\cos(\frac{\beta_{Gfp.in}}{2})\cos(\varphi_{Gfp} - \varphi_{Pp})\sin(\Sigma_P) + \sin(\frac{\beta_{Gfp.in}}{2})\cos(\Sigma_P)\right] \quad \text{(\#B7)}$$

where θ_{GfpPp} is the ray incident angle from far field patch center onto panel patch center, φ_{Gfp} is far field patch center azimuth angle, φ_{Pp} panel azimuth angle and Σ_P is panel tilting angle. Notice that $\beta_{Gfp.in}$ is negative for this calculation.

Regarding the horizontal angle between incidence and reflection, γ is only valid on the horizontal reflection plane, when the reflection ray has an elevation angle β, the effective γ' may then be acquired from: $\gamma' = \arcsin(\cos\beta\sin\gamma)$.

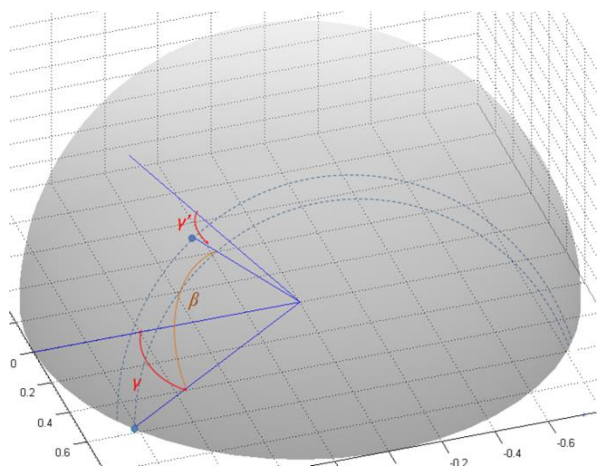

Figure 70 azimuth deviation angle between incidence and reflection, γ, changes to effective γ' when reflecting ray has an elevation angle β

Hence, the radiant flux is from the sun and reflected by a far field patch and then received by a panel patch may be expressed as:

$$\Phi(\mathrm{Z_r}) =$$

$$= \frac{[\rho_d - 0.023(\mathrm{f}_{ab}+\mathrm{f}_{af})]+[\delta_\gamma \mathrm{f_{af}} + (1-\delta_\gamma)\mathrm{f_{ab}}]\cos[\arcsin(\cos\beta\sin\gamma)]\mathrm{e}^{-1.77-1.53(\frac{\beta_S}{100})-3.61(\frac{\beta_S}{100})^2}}{\pi} DNI \bullet \cos(Z_S) \bullet \frac{2\pi \bullet \sin(\beta_{Gfp.in})}{N_{FAzD}} [A_{Pp}\cos(\theta_{GfpPp})]$$

$$= \left\{[\rho_d - 0.023(\mathrm{f}_{ab}+\mathrm{f}_{af})]+[\delta_\gamma \mathrm{f_{af}} + (1-\delta_\gamma)\mathrm{f_{ab}}]\cos[\arcsin(\cos\beta\sin\gamma)]\mathrm{e}^{-1.77-1.53(\frac{\beta_S}{100})-3.61(\frac{\beta_S}{100})^2}\right\} DNI \bullet \cos(Z_S) \bullet \frac{2\sin(\beta_{Gfp.in})}{N_{FAzD}} [A_{Pp}\cos(\theta_{GfpPp})](\mathrm{W})$$

(#B8)

When the radiant flux is from a sky patch, the reflection is considered Lambertian, then the expression is simplified as:

$$\Phi(\mathrm{Z_r}) = \rho_d I_{Sp}\cos(Z_{Sp}) \bullet \frac{2\sin(\beta_{Gfp.in})}{N_{FAzD}}[A_{Pp}\cos(\theta_{GfpPp})](\mathrm{W})$$

The total reflection from one far field ground patch to a panel patch is the summation of all sky patch irradiances:

$$\Phi(\mathrm{Z_r})_{\mathrm{total}} = \rho_d \frac{2\sin(\beta_{Gfp.in})}{N_{FAzD}}[A_{Pp}\cos(\theta_{GfpPp})] \bullet \left\{\sum_{i=1}^{skyPatches}[I_{Sp.i}\cos(Z_{Sp.i})]\right\}(\mathrm{W}) \qquad \text{(\#B9)}$$

b. solid angle of near field patches

As for patches on near field circular field bands, the solid angle for one patch on the near field band may be: $\Omega_{GpPp} = \frac{A_{Gp}\cos(\mathrm{Z_r})}{D_{GpPp}^2}$ where the near field patch area $A_{Gp} = \frac{\pi(\mathrm{d}_2^2 - \mathrm{d}_1^2)}{N_{FAzD}}$, d_1 and d_2 are the inner and outer edge radii of the patch (Figure 71) and D_{Gp-Pp} is the 3-D distance between the near field patch center and the panel patch center, which can be obtained from the coordinated of the patch centers. Therefore, the solid angle is $\Omega_{GpPp} = \frac{\pi(\mathrm{d}_2^2 - \mathrm{d}_1^2)}{N_{FAzD}} \bullet \frac{\cos(\mathrm{Z_r})}{D_{GpPp}^2}$.

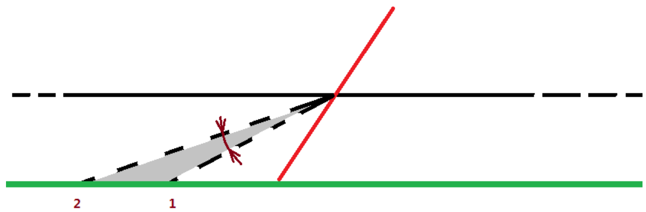

Figure 71 Scheme of near field ground patch approximation

The radiant flux from the sun, and reflected by a near field patch and received by a panel patch may be expressed as:

$$\Phi(\mathrm{Z_r}) =$$

$$= \frac{[\rho_d - 0.023(\mathrm{f}_{ab}+\mathrm{f}_{af})] + [\delta_\gamma \mathrm{f_{af}} + (1-\delta_\gamma)\mathrm{f_{ab}}]\cos[\arcsin(\cos\beta\sin\gamma)]e^{-1.77-1.53(\frac{\beta_S}{100})-3.61(\frac{\beta_S}{100})^2}}{\pi} DNI \bullet \cos(Z_S) \bullet \frac{\pi(\mathrm{d}_2^2-\mathrm{d}_1^2)}{N_{FAzD}} \bullet \frac{\cos(\mathrm{Z_r})}{D_{GpPp}^2}[A_{Pp}\cos(\theta_{GpPp})]$$

$$= \left\{[\rho_d - 0.023(\mathrm{f}_{ab}+\mathrm{f}_{af})] + [\delta_\gamma \mathrm{f_{af}} + (1-\delta_\gamma)\mathrm{f_{ab}}]\cos[\arcsin(\cos\beta\sin\gamma)]e^{-1.77-1.53(\frac{\beta_S}{100})-3.61(\frac{\beta_S}{100})^2}\right\} DNI \bullet \cos(Z_S) \bullet \frac{(\mathrm{d}_2^2-\mathrm{d}_1^2)}{N_{FAzD}} \bullet \frac{\cos(\mathrm{Z_r})}{D_{GpPp}^2}[A_{Pp}\cos(\theta_{GpPp})](\mathrm{W})$$

(#B10)

As for Lambertian reflection to radiant flux from a sky patch, the expression is simplified as:

$$\Phi(\mathrm{Z_r}) = \rho_d I\cos(Z_{Sp}) \bullet \frac{\pi(\mathrm{d}_2^2-\mathrm{d}_1^2)}{N_{FAzD}} \bullet \frac{\cos(\mathrm{Z_r})}{D_{GpPp}^2}[A_{Pp}\cos(\theta_{GpPp})](\mathrm{W}).$$

If there is no blocking between any sky patch to this near field ground patch, the irradiance on the ground patch is the summation of all sky patch radiances, and the total reflection from the near field ground patch to a panel patch is:

$$\Phi(\mathrm{Z_r})_{\mathrm{total}} = \rho_d \frac{(\mathrm{d}_2^2-\mathrm{d}_1^2)}{N_{FAzD}} \bullet \frac{\cos(\mathrm{Z_r})}{D_{Gp-Pp}^2}[A_{Pp}\cos(\theta_{GpPp})]\left\{\sum_{i=1}^{skyPatches}[I_{Sp.i}\cos(Z_{Sp.i})]\right\}(\mathrm{W}).$$

For radiance from a sky patch toward a near field ground patch, if the ray is blocked by any part of the racking, this ray becomes terminated at the racking because of the assumption in this project that the racking does not reflect. If a ray hits the panel on its way from sky toward ground, the ray need to be multiplied by an angular transmission function for two air-glass interfaces, and an area-ratio factor (transparent area/total panel area).

Appendix C Combining Perez 1986 and 1990 models to calculate radiance at any point on sky dome

This appendix is a piece of work done during the project. It attempted to derive and combine the two Perez models (1986 [42] and 1990 [40]) to calculate the radiance at any point over the sky dome. By doing this, the combined model can be used in simulations with sky dome being divided into patches (Figure 15).

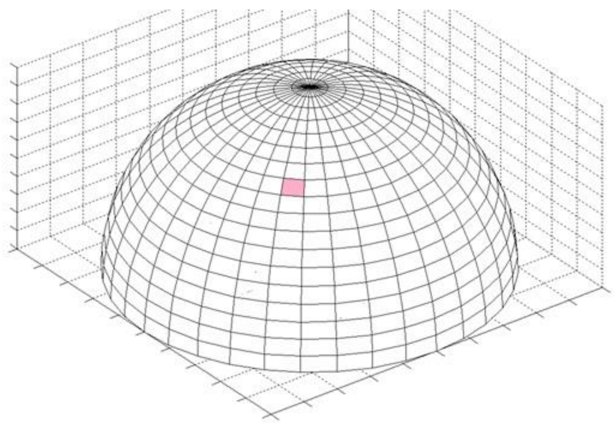

Figure 72 Sky dome division in simulation

This is based on that the sky dome brightness (radiance) is defined as three parts: the isotropic background; a circumsolar brighter region to be further simplified as a point source at the same position as the sun; and a brighter horizon band.

Description of the two Perez models

In papers published in 1986 through 1990, Perez et al. modeled the diffuse light as three parts: the sky dome as an isotropic background, the circumsolar brighter region and the horizon band brighter region [40] [42]. And further they created a way to determine the shares of radiance for the three parts under different types of sky conditions.

The sky conditions are categorized by sky clearness ε which Perez et al. defined it as

$$\varepsilon = \frac{\frac{(DHI + DNI)}{DHI} + \kappa {Z_S}^3}{1 + \kappa {Z_S}^3} \qquad (\#C11)$$

where Z_S is solar zenith angle, and κ (kappa) is a zenith angle constant equals to 1.041for Z_S in radians [40]. The parameter is categorized in 8 bins, with low value for heavier clouds.

Table 11 Sky clearness ε, and the bounds of ε bins

ε bins	Lower bound	Upper bound
1 overcast	1	1.065
2	1.065	1.23
3	1.23	1.5
4	1.5	1.95
5	1.95	2.8
6	2.8	4.5
7	4.5	6.2
8 clear sky	6.2	---

Another parameter is sky brightness Δ:

$$\Delta = \frac{DHI * m}{Io} \qquad \text{(\#C12)}$$

Summary of inputs for the sky models:

For the beam: DNI; solar position (azimuth angle and elevation angle) determined by date, time and location latitude.

For sky diffuse light: DNI; DHI; solar position (azimuth angle and elevation angle); extra-terrestrial radiance I_O; relative air mass m; assumed horizon band angular height (thickness) ξ; circumsolar region half angle α;

Determination of the fractions (shares) for the three parts of sky diffuse irradiance

Perez's 1990 model [40]

From Perez's 1990 model, the diffuse irradiance incident on a tilted plane can be calculated as:

$$I_{DT} = DHI[(\frac{1+\cos\Sigma_P}{2})(1-F_1') + F_1'\frac{\cos\theta_{BPf}}{\cos Z_S} + F_2'\sin\Sigma_P] \qquad \text{(\#C13)}$$

where F_1' and F_2' are circumsolar anisotropy coefficient, and horizon band anisotropy coefficient respectively, and θ the incident angle onto the panel from the direction of the sun.

Firstly, reform the formula into:

$$I_{DT} = DHI[(\frac{1+\cos\Sigma_P}{2})(1-F_1') + F_1'\frac{\cos\theta_{BPf}}{\cos Z_S} + F_2'\sin\Sigma_P] \qquad (\#C14)$$

Let $(1-F_1')DHI$ be a coefficient Ψ, the above is simplifies as:

$$I_{DT} = \Psi[(\frac{1+\cos\Sigma_P}{2}) + \frac{F_1'}{(1-F_1')}\frac{\cos\theta_{BPf}}{\cos Z_S} + \frac{F_2'}{(1-F_1')}\sin\Sigma_P] \qquad (\#C15)$$

Now, let's consider when the panel is vertical and $\Sigma = 90°$, the above formula becomes:

$$I_{DT} = \Psi[\frac{1}{2} + \frac{F_1'}{(1-F_1')}\frac{\cos\theta_{BPf}}{\cos Z_S} + \frac{F_2'}{(1-F_1')}] \qquad (\#C16)$$

In this case, $\frac{F_2'}{(1-F_1')}$ represents a factor for received irradiance from half of the horizon band based on the condition that the sky dome background radiance is normalized to be unit 1. Therefore the received irradiance from the horizon band takes a factor of $\frac{\pi F_2'}{(1-F_1')}$. The contribution to DHI from this band may be: $\frac{\pi F_2'}{(1-F_1')}(\sin\xi)^2$, if the horizon band takes an angular thickness of ξ.

When the panel lies horizontal and $\Sigma_P = 0°$, the above formula becomes:

$$I_{DT} = \Psi[1 + \frac{F_1'}{(1-F_1')}] \qquad (\#C17)$$

In this case, $\frac{F_1'}{(1-F_1')}$ represents a factor of received diffuse irradiance from the circumsolar region. Therefore the received irradiance from the circumsolar region takes a factor of

$\frac{F_1'}{(1-F_1')\cos Z_S}$. The contribution to DHI from this circumsolar region may be: $\frac{F_1'}{(1-F_1')\cos Z_S}\cos Z_S = \frac{F_1'}{1-F_1'}$.

Considering the horizon band with an angular thickness of ξ , and the average sky dome radiance given as L (W/sr/m^2), *DHI* may be expressed as:

$$DHI = \Psi[1+\frac{F_1'}{(1-F_1')}+\frac{\pi F_2'}{(1-F_1')}(\sin\xi)^2] = \pi \mathrm{L}[1+\frac{F_1'}{(1-F_1')}+\frac{\pi F_2'}{(1-F_1')}(\sin\xi)^2] \qquad (\#C18)$$

The value set for F_1', F_2' under various sky conditions can be obtained from:

$$F_1' = F_{11}' + F_{12}' * \Delta + F_{13}' * Z_S \qquad (\#C19)$$

$$F_2' = F_{21}' + F_{22}' * \Delta + F_{23}' * Z_S \qquad (\#C20)$$

The sub-coefficients F_{11}', F_{12}', F_{13}', F_{21}', F_{22}' and F_{23}' are tabulated below corresponding to the sky conditions described by the ε bins.

Table 12 Perez model coefficients for irradiance (from 1990 model)

	For circumsolar region			For horizontal band		
ε bin	F'_{11}	F'_{12}	F'_{13}	F'_{21}	F'_{22}	F'_{23}
1 overcast	-0.008	0.588	-0.062	-0.06	0.072	-0.022
2	0.13	0.683	-0.151	-0.019	0.066	-0.029
3	0.33	0.487	-0.221	0.055	-0.064	-0.026
4	0.568	0.187	-0.295	0.109	-0.152	-0.014
5	0.873	-0.392	-0.362	0.226	-0.462	0.001
6	1.132	-1.237	-0.412	0.288	-0.823	0.056
7	1.06	-1.6	-0.359	0.264	-1.127	0.131
8 clear sky	0.678	-0.327	-0.25	0.156	-1.377	0.251

Perez's 1986 model [42]

From Perez's 1986 model: If the radiance (W*sr^{-1}*m^{-2}) originating from the main portion of the dome, the circumsolar and the horizon band are respectively equal to L (W*sr^{-1}*m^{-2}) , F_1*L, and F_2*L, then the resulted horizontal diffuse irradiance (W*m^{-2}) can be expressed as:

$$DHI = \pi L[1 + 2(1 - \cos\alpha) X(\mathrm{Z})(\mathrm{F}_1 - 1)\cos \mathrm{Z}' + \frac{(1 - \cos(2\xi))(\mathrm{F}_2 - 1)}{2}] \quad \text{(\#C21)}$$

$\mathrm{X(Z)}$ is the fraction of the circumsolar region seen by the horizontal plane, and Z' is its average incident angle if it is partially seen. Since we simplify the circumsolar part to be point sources, therefore, $\mathrm{X(Z)}$ is always 1 as long as the sun is above the horizon, and Z' is always Z_S. Hence, the formula is simplified to be:

$$DHI = \pi L[1 + 2(1 - \cos\alpha)(\mathrm{F}_1 - 1)\cos \mathrm{Z_S} + \sin^2(\xi)(\mathrm{F}_2 - 1)] \quad \text{(\#C22)}$$

Comparing equations (#C18) and (#C22), the extra radiance level of the circumsolar region is:

$$F_1 - 1 = \frac{F_1'}{2(1 - \cos\alpha)\cos \mathrm{Z_S}(1 - F_1')} \quad \text{(\#C23)}$$

Same for the horizon band:

$$F_2 - 1 = \frac{\pi F_2'}{(1 - F_1')} \quad \text{(\#C.24)}$$

Irradiance calculation

The isotropic background

Also from eq.(#C18), $L = \dfrac{DHI}{\pi[1 + \dfrac{F_1'}{(1 - F_1')} + \dfrac{\pi F_2'}{(1 - F_1')}(\sin\xi)^2]} = \dfrac{(1 - F_1')DHI}{\pi[1 + \pi F_2'(\sin\xi)^2]}$, the radiance of the isotropic background can now be calculated as:

$$I_{ISO} = 2\pi L = 2\pi \frac{DHI}{\pi[1+\frac{F_1'}{(1-F_1')}+\frac{\pi F_2'}{(1-F_1')}(\sin\xi)^2]} = 2(1-F_1')\frac{DHI}{1+\pi F_2'(\sin\xi)^2} \quad \text{(\#C.25)}$$

The extra circumsolar diffuse radiance

The extra circumsolar diffuse radiance superposed onto the isotropic sky dome “background” may be obtained:

$$I_{cs} = 2\pi(1-\cos\alpha)(\mathrm{F_1}-1)L = 2\pi(1-\cos\alpha)\frac{F_1'}{2(1-\cos\alpha)\cos\mathrm{Z_S}(1-F_1')}L$$
$$= \frac{F_1'}{\cos\mathrm{Z_S}} \bullet \frac{DHI}{1+\pi F_2'(\sin\xi)^2} = \frac{F_1' \bullet DHI}{\cos\mathrm{Z_S} \bullet [1+\pi F_2'(\sin\xi)^2]} \quad \text{(\#C.26)}$$

Since the circumsolar brighter region is simplified to be a point source, the radiance from it can simply be expressed as I_{cs} given above.

The horizon band

As for the superposed extra of horizontal band:

$I_{hb} = 2\pi\sin(\Delta Z)(\mathrm{F_2}-1)L = 2\sin(\Delta Z)\pi F_2'\frac{DHI}{1+\pi F_2'(\sin\xi)^2}$. The overall irradiance of horizon band is a superposition of the sky dome irradiance and the extra:

$$I_{HB} = I_{ISO} + I_{hb} = 2\left[(1-F_1') + \pi\sin(\Delta Z)F_2'\right]\frac{DHI}{1+\pi F_2'(\sin\xi)^2} \quad \text{(\#C.27)}$$

where ΔZ is the sky dome angular division.

Appendix D List of parameters in Matlab simulation code

** There are parameters not listed in this table of which they are obvious in the code and only exist in one function.*

*** There are empty cells in the column of "Symbols in thesis" since intermediate parameters are widely used in the simulation code but not necessary existing in mathematical model and thesis.*

Parameter names in Matlab code*	***Parameter meaning and unit/dimension***	***Symbol in thesis*****
L	Local latitude (°)	L
Longitude	Local longitude (°)	
Longitude_timeZone	Longitude of the time zone (°)	
Sp_az_div	Sky patching azimuth division	N_{GpAzD}
Sp_elev_div	Sky patching elevation division	
gp_az_div	Ground patching azimuth division	
gp_radial_div	Ground patching radial division	
gp_sect_half_angle	Half azimuthal angle of each ground patch	
phi_P	Panel azimuth angle (°)	φ_{Pf}
Sigma_P	Panel tilting angle (°)	Σ_P
h	Clearance (m)	
P_number	Number of panels set in this model	

Parameter names in Matlab code*	***Parameter meaning and unit/dimension***	***Symbol in thesis*****
Rack_side	Racking post side size (m)	
h_P	Panel height (m)	
w_P	Panel width (m)	
PanelFilterFactor	Panel filtering factor	
A_P	Panel total area (m^2)	A_P
h_Sc	Solar cell height (m)	
w_Sc	Solar cell width (m)	
cutOff	Solar corner cut-off (m)	
A_SC	Solar cell area (m^2)	
EdgeT	Width of panel top edge (m)	
EdgeB	Width of panel bottom edge (m)	
SideEdge	Width of panel side edges (m)	
stripTB	Vertical strip between solar cells (m)	
stripLR	Horizontal strip between solar cells (m)	
ScRow	Number of solar cell rows	
ScColumn	Number of solar cell columns	
n_SC	Number of solar cells on panel	n_{Sc}
SC_Patching_div	Solar cell patching division number	

*Parameter names in Matlab code**	*Parameter meaning and unit/dimension*	*Symbol in thesis***
n_ARC	Average refractive index of ARC layer	N_{ARC}
n_Glass	Average refractive index of glass	n_g
n_EVA	Average refractive index of EVA	n_{EVA}
n_Si_ARC	Average refractive index of ITO	n_{ITO}
n_Si	Average refractive index of silicon	n_{Si}
TransmitFrontNorm	Front side normal incidence transmittances	T_{PfN}
TransmitRearNorm	Rear side normal incidence transmittances	T_{PrN}
uncover_f	Area ratio of front side uncovered by bus bars and fingers	
uncover_r	Area ratio of rear side uncovered by bus bars and fingers	
bifaciality	Bifaciality	
Ratio_PhPToI	Solar cell received photonic power to short circuit current conversion ratio under STC (I/W)	r_{PI}
NOCT	Nominal operation cell temperature (°c)	*NOCT*
Isc_test	Short circuit current of measured I-V curve (A/cell)	I_{SC}
Voc_std	Open circuit voltage of measured I-V curve (V/cell)	V_{OC}
Rs	Regressed series resistance per cell (Ω/cell)	R_S

*Parameter names in Matlab code**	*Parameter meaning and unit/dimension*	*Symbol in thesis***
Rsh	Regressed shunt resistance per cell (Ω/cell)	R_P
m	Regressed ideality factor per cell	m
qOverk	Combined factor of electron charge over Boltzmann constant (C*k/J) (Coulombs*Kelvin/Joule)	q/k
i0_std	Regressed dark current per cell at STC (A/cell)	I_0
C_I_Temp	Short circuit current thermal coefficient (1/k)	c_{CT}
C_V_Temp	Open circuit voltage thermal coefficient (1/k)	c_{VT}
T_stcK	Standard test condition temperature in Kelvin (k)	T
delta	Solar declination (daily based) (°)	δ
H	Hour angle (°)	H
n_day	Day numbers in a year	
Hr	Hour numbers in a day	
Io	Extraterrestrial solar radiance changed daily (W/m^2)	I_O
DNI	Direct normal irradiance (W/m^2)	DNI
DHI	Diffuse horizontal irradiance (W/m^2)	DHI
T_amb	Ambient temperature at test site (°C)	$T_{AmbientAir}$

Parameter names in Matlab code*	***Parameter meaning and unit/dimension***	***Symbol in thesis*****
rho	Diffuse reflectance	ρ (ρ_d is almost equal to ρ)
f_af	Forward anisotropic coefficient	f_{af}
f_ab	Backward anisotropic coefficient	f_{ab}
Beta_Sun	Solar elevation angle (°)	β_S
Zenith_Sun	Solar zenith angle (°)	Z_S
phi_Sun	Solar azimuth angel (°)	φ_S
airMass	Air mass	M
rho_d	(Ground) diffuse reflectance	ρ_d
P93a1, P93a2, P93a3, P93a4, P93b1, P93b2, P93b3, P93b4, P93c1, P93c2, P93c3, P93c4, P93d1, P93d2, P93d3, P93d4, P93e1, P93e2, P93e3, P93e4, P93aZnth, P93bZnth, P93cZnth, P93dZnth	Perez 1993 model adjustable coefficients	
h_CD	Height of panel array higher posts (m)	
x_A,y_A,z_A,x_B,y_B,z_B,x_C,y_C,z_C,x_D,y_D,z_D	3-d coordinates of the panel under investigation (m)	
x_Array_A,y_Array_A,z_Array_A,x_Array_B,y_Array_B,z_Array_B,x_Array_C,y_Array_C,z_Array_C, x_Array_D,y_Array_D,z_Array_D	3-d coordinates of the panel array (m)	

Parameter names in Matlab code*	***Parameter meaning and unit/dimension***	***Symbol in thesis*****
vertPatchLine, horizPatchLine	Arrays of panel patches' vertical and horizontal lines (intermediate parameters for panel patch coordinates calculation) (m)	
PpCentralWidth2D, PpCentralHeight2D	2-d matrices of panel patch centers' on-panel positions (intermediate parameters for panel patch coordinates calculation) (m)	
PpCentralX3D, PpCentralY3D, PpCentralZ3D	2-d matrices of coordinates of panel patch centers (m)	x_{Pp}, y_{Pp}, z_{Pp}
PanelPlotHeight, PanelPlotWidth	2-d matrices of panel patch on-panel positions for plotting (m)	
A_Pp	2-d matrix of panel patch areas (m^2)	A_{Pp}
A_CellInPatch	2-d matrix of solar cell areas in each panel patch (m^2)	
CellPatchAreaRatio	2-d matrix with each element correspondingly as "solar cell areas in each panel patch/panel patch areas"	
n_PatchingColumns	Number of panel patch columns	
n_PatchingRows	Number of panel patch rows	

*Parameter names in Matlab code**	*Parameter meaning and unit/dimension*	*Symbol in thesis***
x_Aabcd,y_Aabcd,x_Babcd,y_Babcd,x_Cabcd,y_Cabcd,x_Dabcd,y_Dabcd, x_L_Aabcd,y_L_Aabcd,x_L_Babcd,y_L_Babcd,x_L_Cabcd,y_L_Cabcd,x_L_Dabcd,y_L_Dabcd, x_L2_Aabcd,y_L2_Aabcd,x_L2_Babcd,y_L2_Babcd,x_L2_Cabcd,y_L2_Cabcd,x_L2_Dabcd,y_L2_Dabcd, x_R_Aabcd,y_R_Aabcd,x_R_Babcd,y_R_Babcd,x_R_Cabcd,y_R_Cabcd,x_R_Dabcd,y_R_Dabcd, x_R2_Aabcd,y_R2_Aabcd,x_R2_Babcd,y_R2_Babcd,x_R2_Cabcd,y_R2_Cabcd,x_R2_Dabcd,y_R2_Dabcd	Panel racking post corner position coordinates (m)	
gpCentralAzm	2-d matrix of ground patch central point azimuth angles (°)	
gpInnerRadii, gpOuterRadii	2-d matrices of ground patch inner and outer edges' radii (m)	R_{Gp} & r_{Gp}
x_gpCenter, y_gpCenter	2-d matrices of ground patch central point Cartesian coordinates (m)	x_{Gp}, y_{Gp}
x_gpMassCenter, y_gpMassCenter	2-d matrices of ground patch center of mass Cartesian coordinates (m)	
gpPlotX, gpPlotY	2-d matrices of ground patch corners' Cartesian coordinates for plotting (m)	
spCentralAzm, spCentralZenith	2-d matrices of sky patch central point azimuth and zenith angles (°)	φ_{Sp}, β_{Sp} i.e. $(90°-Z_{Sp})$

*Parameter names in Matlab code**	*Parameter meaning and unit/dimension*	*Symbol in thesis***
spArea	2-d matrix of normalized sky patch areas is equivalent to sky patch solid angles seen from ground	Ω_{Sp}, A_{Sp}, or $A_{Sp.i}$
theta_Sp_Pf, theta_Sp_Pr	2-d matrices of incidence angles of sky patches toward panel front and rear side (°)	θ_{SpPf}, θ_{SpPr}
cos_theta_Sp_Pf, cos_theta_Sp_Pr	2-d matrices of cosine of incidence angles of sky patches toward panel front and rear side	
illumin_Sp_Pf	4-d matrix of normalized irradiance from isotropic conditioned sky patches toward panel front side	$I_{SpPfNormalized}$
illumin_Sp_Pr	4-d matrix of normalized irradiance from isotropic conditioned sky patches toward panel rear side w/o post blocking	$I_{SpPrNormalized}$
SpPlotX, SpPlotY, SpPlotZ	2-d matrices of sky patch corners' coordinates for plotting (m)	
Sp_Pp_Post_Block	4-d matrix of information on post blocking of rays from sky patches toward panel rear patches	
Sp_Pp_Rear_illumin	4-d matrix of normalized irradiance from isotropic conditioned sky patches toward panel rear side with post blocking	
Sp_Ppr_illumin_SumUp	2-d matrix of total normalized sky diffuse irradiance on panel rear side with post blocking	
Sp_Gp_Post_Block	4-d matrix of information on post blocking of rays from sky patches toward ground patches	

Parameter names in Matlab code*	***Parameter meaning and unit/dimension***	***Symbol in thesis*****
Sp_Gp_Panel_Shade	4-d matrix of information on panel array shading of rays from sky patches toward ground patches	
Sp_Gp_PanelAndPosts_Shade_Check	4-d matrix of information of combination of above two matrices	
Sp_Gp_illumination	4-d matrix of normalized irradiance from isotropic conditioned sky patches toward ground patches with blocking and shading information	
Gp_illuminance_SumUp	2-d matrix of total normalized sky diffuse irradiance on ground patches with blocking and shading information	
Gp_Pp_Rear_Post_Block	4-d matrix of information on post blocking of ground reflecting rays toward panel rear patches	
Gp_Pp_Ray_Horizonal_Angle	4-d matrix of information of ground reflecting rays' azimuth angles toward panel patches (°)	ω_{GpPpH}
beta_G_P	4-d matrix of information of ground reflecting rays' elevation angles toward panel patches (°)	β_r
theta_G_Pf, theta_G_Pr	4-d matrices of ground reflecting rays' incidence angle information onto panel front and rear patches (°)	θ_{GpPf} (& θ_{GpPr}=180°-θ_{GpPf})
for specific G-patch to P-patch	Ground reflecting rays' incidence angle information onto panel front patches (°)	$\theta_{GpPpf.i}$
d_G_P	4-d matrix of horizontal distances between ground patches toward panel patches (m)	

Parameter names in Matlab code*	***Parameter meaning and unit/dimension***	***Symbol in thesis*****
d_G_P_3D	4-d matrix of space distances between ground patches toward panel patches (m)	D_{GpPp}
beta_ffG_P_innerRing	4-d matrix of elevation angles from "far-field" ground patch inner edge centers toward panel patches (°)	$\beta_{Gfp.in}$
Gp_Pp_SolidAngle	4-d matrix of information on solid angle of ground patches viewed from panel patches (Sr.)	Ω_{GpPp}
Gp_Ppf_geo, Gp_Ppr_geo	4-d matrices of all geometric information on ground patches toward panel patches, including viewing factor, solid angle and cosine of incidence angle on panel front and rear patches	f_{GeoGPf} for front side
Gp_Ppf_CompensateFactor, Gp_Ppr_CompensateFactor	4-d matrices of compensating information on ground patches Lambertian reflection toward panel front and rear patches	$f_{GpPpComp}$, $f_{GpPpfComp}$, $f_{GpPprComp}$
Gp_Ppf_geo_Compensated, Gp_Ppr_geo_Compensated	4-d matrices of above "Gp_Ppf_geo" and " Gp_Ppr_geo" with corresponding compensation	
Gp_Ppr_geo_NoBlocking_Compensated	4-d matrix of geometric information on ground patches toward panel rear patches w/o post blocking	
theta_Sun_Pf, theta_Sun_Pr	Incidence angle of sun beam toward panel front and rear sides (°)	θ_{BPf} also θ_S, θ_{BPr}
Sun_Ppf_irradiance, Sun_Ppr_irradiance	2-d matrix of irradiance on panel front and rear patches by sun beam with information of rear side post blocking (W/m^2)	I_{BPf}, I_{BPr}

Parameter names in Matlab code*	***Parameter meaning and unit/dimension***	***Symbol in thesis*****
Sun_Ppf_Power, Sun_Ppr_Power	2-d matrices of information on sunbeam photonic power received at each panel patch in silicon layer from front and rear side (Watts patch-wise)	
Sun_Gp_Post_Block	2-d matrix of information on post blocking of sun beam toward ground patches	
Sun_Gp_Panel_Shade	2-d matrix of information on panel array shading of sun beam toward ground patches	
Sun_Gp_PanelAndPosts_Shade_Check	2-d matrix of information of combination of above two matrices	
Sun_Gp_irradiance_NoShading	2-d matrix of information of sun beam irradiance on ground, i.e. DNI*cos(phi_s) on every ground patch (W/m^2)	I_{BG}
Sun_Gp_irradiance	2-d matrix of sun beam irradiance on ground multiplies shading and blocking information from "Sun_Gp_panelAndPosts_Shade_Check" (W/m^2)	I_{BG}
rho_b	4-d matrix of information on Gueymard's directional reflection from ground patches toward panel patches	ρ_b
Sun_Gp_Ppf_Compensated2, Sun_Gp_Ppr_Compensated2	2-d matrices of information on irradiance received on panel front and rear patches from beam reflected by ground with error reduction (W/m^2)	

*Parameter names in Matlab code**	*Parameter meaning and unit/dimension*	*Symbol in thesis***
BG_Ppf_Power_SumUp, BG_Ppr_Power_SumUp	2-d matrices of information on ground-reflected-beam photonic power received at each panel patch in silicon layer from front and rear side (Watts patch-wise)	
Sun_Gp_Ppf_ErReductCompensator, Sun_Gp_Ppr_ErReductCompensat	2-d matrices of information on sun beam to ground reflecting to panel front and rear side error reduction factor	$C_{ErBGPf.i}$, $C_{ErBGPr.i}$
kp	Perez sky model parameter kappa (= 1.041 when solar zenith angle is in radians)	κ
epsilon	Perez sky model parameter sky clearness	ε
delta_P93, delta_P93adjst	Perez sky model parameter sky brightness, and its adjusted value =0.2 when calculated value is < 0.2	Δ
Sp_Sun_Angle_Dist	2-d matrix of angular distance between sky patch center and the position of the sun (°)	χ
SpLuminancePrep	2-d matrix of preparatory values for radiance at sky patch centers (luminance used in Perez paper)	$f(Z_{SP}, \chi)$
DHI_ContributnPrep	2-d matrix of sky patch contribution to DHI based on their preparatory values of radiance	
DHI_SumUp	The sum up of above contributions	DHI_{Prep}
NormFactor	The ratio of measured DHI over the sum-up DHI, used as a normalization factor	$f_{NormDHI}$

*Parameter names in Matlab code**	*Parameter meaning and unit/dimension*	*Symbol in thesis***
SpLuminanceDistr	2-d matrix of sky patch center radiance values based on Perez 1993 sky model's distribution and summing up to measured DHI (W/Sr./m^2)	$L_{SpActual.j}$
Sp_Ppf_irradiance_SumUp, Sp_Ppr_irradiance_SumUp	2-d matrix of sky diffuse irradiance on panel front and rear patches with blocking information on rear side (W/m^2)	I_{DT}
Sp_Gp_irradiance_SumUp	2-d matrix of sky diffuse irradiance on ground with shading and blocking information (W/m^2)	*DHI*
DiffuseGp_Ppf_irradiance_SumUp, DiffuseGp_Ppr_irradiance_SumUp	2-d matrix of reflected sky diffuse irradiance by ground onto panel front and rear patches with rear side blocking information (W/m^2)	
IAM_Beam_Ppf, IAM_Beam_Ppr, IAM_BG_Ppf, IAM_BG_Ppr etc.	Incidence angle modifiers for panel front and rear side --- same for any incidence, sun beam, sky diffuse or ground reflection	*IAM*
Sp_Ppf_Power_SumUp, Sp_Ppr_Power_SumUp	2-d matrices of information on photonic power from sky diffuse radiance and received at each panel patch in silicon layer from front and rear side (Watts patch-wise)	
DiffuseGp_Ppf_Power_SumUp, DiffuseGp_Ppr_Power_SumUp	2-d matrices of information on ground-reflected-beam power received at each panel patch in silicon layer from front and rear side (Watts patch-wise)	

*Parameter names in Matlab code**	*Parameter meaning and unit/dimension*	*Symbol in thesis***
total_Gp_irradiance	2-d matrix of sum of sun beam and sky diffuse irradiance on ground with shading and blocking information for plotting purpose only (W/m^2)	
Ppf_Power, Ppr_Power	2-d matrices of photonic power received at each panel patch in silicon layer from front and rear (Watts patch-wise)	
Cell_PhotonPowerF, Cell_PhotonPowerR	2-d matrices of photonic power received at each solar cell in silicon layer from front and rear, by combining corresponding patches into cell (Watts cell-wise)	
E_Matrix	2-d matrix of irradiance received by each panel patch front and rear together (W/m^2)	
E	Averaged irradiance on the panel front and rear together (W/m^2)	E
T	Average cell temperature as simplified as identical at a time (k)	T_{module} (also as T in general formula)
Cell_Isc_Std	2-d matrix of short circuit current from photonic-electrical conversion at each solar cell under STC (Ampere/cell)	$I_{SC.STC}$
Cell_Isc, Cell_Isc_Vector, Cell_Isc_Vector_element_number	2-d matrix of real short circuit current based on "cell_Isc_Std" but when solar cells are at field real temperature; the short circuit vector of the cells; and the vector length (Ampere/cell)	$I_{SC}(T)$
Isc_Std_Ave	Average of STC short circuit currents of all solar cells (Ampere/cell)	$I_{SC.STC.AVE}$

Parameter names in Matlab code*	***Parameter meaning and unit/dimension***	***Symbol in thesis*****
Isc_Ave	Average of real short circuit currents at field real temperature (Ampere/cell)	$I_{SC.AVE}(T)$
i0	Simplified average dark current at a time, with temperature and corresponding open circuit voltage in consideration (Ampere/cell)	$I_0(T)$
V1,V2,….V72	*V(i)* is a vector of interpolated voltage on a solar cell's I-V curve when current is linearly spaced, used to sum up to obtain panel total I-V curve as all cells in series (V)	V
Vb	Vector of voltage on total panel I-V curve (V)	
V_max, I_max, p_max	The voltage, current and power values at the total panel maximum power point (V, A, W/panel)	
HourOutput	The hourly energy output from "3600*p_max" (Joule)	
HourlyEnergyOutputJ	Vector with length of time stamp number to collect hourly energy output from each time stamp as its elements (Joule)	
AnnualEnergyJ	The sum up of elements in vector "HourlyEnergyOutputJ " as the annual total (annual) energy output (Joule)	
AnnualEnergy_kWHr	The same amount of total (annual) energy output as "AnnualEnergyJ" but in kWh as the simulation final output	

References

[1] SoftSchools. (2016, july 23). *Fossil Fuel Facts*. Available: http://www.softschools.com/facts/energy/fossil_fuel_facts/407/

[2] W. Zittel, J. Zerhusen, and M. Zerta, "Fossil and Nuclear Fuels – the Supply Outlook," ed, 2013.

[3] G. M. Masters, *Renewable and Efficient Electric Power Systems*. Hoboken: Hoboken John Wiley & Sons, Inc., 2004.

[4] C. Honsberg and S. Bowden. (2015, July 23). *Solar Radiation at the Earth's Surface - PVEducation*. Available: http://www.pveducation.org/pvcdrom/2-properties-sunlight/solar-radiation-earths-surface

[5] C. Honsberg and S. Bowden. (2015, July 23). *Introduction - PVEducation*. Available: http://www.pveducation.org/pvcdrom/introduction/introduction

[6] W. contributors. (24 July 2016). *Solar panel* Available: https://en.wikipedia.org/w/index.php?title=Solar_panel&oldid=731049264

[7] M. Raugei and P. Frankl, "Life cycle impacts and costs of photovoltaic systems: Current state of the art and future outlooks," *Energy,* vol. 34, pp. 392-399, 3// 2009.

[8] H. Wirth, "Recent facts about photovoltaics in Germany," Fraunhofer ISE2016 April 22 2016.

[9] O. M. o. Energy. (2016, July 23). *FIT and microFIT Program*. Available: http://www.energy.gov.on.ca/en/fit-and-microfit-program/

[10] SUNPOWER. 2016-06-28). The Drivers of the Levelized Cost of Electricity for Utility-Scale Photovoltaics. Available: https://us.sunpower.com/sites/sunpower/files/media-library/white-papers/wp-levelized-cost-drivers-electricity-utility-scale-photovoltaics.pdf

[11] L. Kreinin, N. Bordin, A. Karsenty, A. Drori, D. Grobgeld, and N. Eisenberg, "PV module power gain due to bifacial design. Preliminary experimental and simulation data," in *Photovoltaic Specialists Conference (PVSC), 2010 35th IEEE*, 2010, pp. 002171-002175.

[12] L. Yang, Q. H. Ye, A. Ebong, W. T. Song, G. J. Zhang, J. X. Wang, *et al.*, "High efficiency screen printed bifacial solar cells on monocrystalline CZ silicon," *Progress in Photovoltaics: Research and Applications,* vol. 19, pp. 275-279, 2011.

[13] R. K. J. Arumughan, T. Pernau, T. Buck, P. Fath, K. Peter, "Realization of thin mc-Si PERT-type bifacial solar cells in industrial environments," presented at the Photovoltaic Energy Conversion, Conference Record of the 2006 IEEE 4th World Conference 2006, Hawaii, 2006.

[14] Y. Tiantian, L. Hongbo, L. Wennan, G. Wenlin, and C. Mingbo, "Research of Commercial Bifacial Silicon Solar Cells," in *Proceedings of ISES World Congress 2007 (Vol. I – Vol. V): Solar Energy and Human Settlement*, D. Y. Goswami and Y. Zhao, Eds., ed Berlin, Heidelberg: Springer Berlin Heidelberg, 2009, pp. 1520-1523.

[15] S. Sepeai, S. L. Cheow, M. Y. Sulaiman, K. Sopian, and S. H. Zaidi, "Fabrication and characterization of Al-BSF bifacial solar cell," in *2013 IEEE 39th Photovoltaic Specialists Conference (PVSC)*, 2013, pp. 2664-2668.

[16] M. Hiroshi, "Radiation energy transducing device," 1966.

[17] A. Luque, A. Cuevas, and J. M. Ruiz, "Double-sided n +-p-n + solar cell for bifacial concentration," *Solar Cells,* vol. 2, pp. 151-166, 1980.

[18] N. M. Bordina, V. V. Zadde, A. K. Zaitseva, A. P. Landsman, D. S. Strebkov, V. I. Streltsova*, et al.*, "Semiconductor photoelectric generator," ed: Google Patents, 1976.

[19] N. M. G. Bordina, T. M.; Zadde, V. V.; Zaitseva, A. K.; Landsman, A. P.; Streltsova, V. I. , "Operation of a thin silicon photoconverter under illumination on both sides," *Applied Solar Energy,* vol. 11, pp. 81-86, 1975.

[20] A. Cuevas, A. Luque, J. Eguren, and J. del Alamo, "50 Per cent more output power from an albedo-collecting flat panel using bifacial solar cells," *Solar Energy,* vol. 29, pp. 419-420, 1982/01/01 1982.

[21] A. Moehlecke, I. Zanesco, and A. Luque, "Practical high efficiency bifacial solar cells," in *Photovoltaic Energy Conversion, 1994., Conference Record of the Twenty Fourth. IEEE Photovoltaic Specialists Conference - 1994, 1994 IEEE First World Conference on*, 1994, pp. 1663-1666 vol.2.

[22] R. Guerrero-Lemus, R. Vega, T. Kim, A. Kimm, and L. E. Shephard, "Bifacial solar photovoltaics – A technology review," *Renewable and Sustainable Energy Reviews,* vol. 60, pp. 1533-1549, 2016.

[23] Y. Ota, K. Nishioka, T. Notohara, K. Sugibuchi, N. Ishikawa, and S. Goda, "Evaluation of performance in bifacial solar cell," in *Advanced Materials and Engineering Materials III* vol. 893, ed: Trans Tech Publications, 2014, pp. 755-759.

[24] L. Kreinin, N. Bordin, A. Karsenty, A. Drori, D. Grobgeld, and N. Eisenberg, "PV module power gain due to bifacial design. Preliminary experimental and simulation data," ed, 2010, pp. 002171-002175.

[25] U. A. Yusufoglu, T. H. Lee, T. M. Pletzer, A. Halm, L. J. Koduvelikulathu, C. Comparotto*, et al.*, "Proceedings of the 4th International Conference on Crystalline Silicon Photovoltaics (SiliconPV 2014)Simulation of Energy Production by Bifacial Modules with Revision of Ground Reflection," *Energy Procedia,* vol. 55, pp. 389-395, 2014/01/01 2014.

[26] J. Johnson, D. Yoon, and Y. Baghzouz, "Modeling and analysis of a bifacial grid-connected photovoltaic system," in *2012 IEEE Power and Energy Society General Meeting*, 2012, pp. 1-6.

[27] J. E. Castillo-Aguilella and P. S. Hauser, "Multi-Variable Bifacial Photovoltaic Module Test Results and Best-Fit Annual Bifacial Energy Yield Model," *IEEE Access,* vol. 4, pp. 498-506, 2016.

[28] K. Matsukuma, K. Morita, and T. Warabisako, "Performance simulation for bifacial silicon solar cells," *Solar Energy Materials and Solar Cells,* vol. 34, pp. 141-148, 1994/09/01 1994.

[29] H. Ohtsuka, M. Sakamoto, M. Koyama, K. Tsutsui, T. Uematsu, and Y. Yazawa, "Characteristics of bifacial solar cells under bifacial illumination with various intensity levels," *Progress in Photovoltaics: Research and Applications,* vol. 9, pp. 1-13, 2001.

[30] C. Deline, S. MacAlpine, B. Marion, F. Toor, A. Asgharzadeh, and J. S. Stein, "Evaluation and Field Assessment of Bifacial Photovoltaic Module Power Rating Methodologies," 2016.

[31] Celestica.com. (2016, 20 July, 2016). Available: https://www.celestica.com/our-expertise/markets/smart-energy-solutions

[32] Uottawa.ca. (2016). *Sunlab*. Available: http://sunlab.eecs.uottawa.ca/

[33] R. Perez, R. Seals, and J. Michalsky, "All-weather model for sky luminance distribution - preliminary configuration and validation," *Solar Energy,* vol. 50, 1993.

[34] C. Gueymard, "An anisotropic solar irradiance model for tilted surfaces and its comparison with selected engineering algorithms," *Solar Energy,* vol. 38, pp. 367-386, // 1987.

[35] F. kasten, "A new table and approximation formula for the relative optical air mass," *Archive für Meteorologie, Geophysik und Bioklimatologie, Serie B,* vol. 14, pp. 206-223, 1965.

[36] J. E. Hay and J. A. Davies, "Calculations of the solar radiation incident on an inclined surface," *Proc. of First Canadian Solar Radiation Data Workshop,* vol. 59, 1980.

[37] T. M. Klucher, "Evaluation of models to predict insolation on tilted surfaces," *Solar Energy,* vol. 23, pp. 111-114, 1979.

[38] D. T. Reindl, W. A. Beckman, and J. A. Duffie, "Diffuse fraction correlations," *Solar Energy,* vol. 45, pp. 1-7, 1990.

[39] D. T. Reindl, W. A. Beckman, and J. A. Duffie, "Evaluation of hourly tilted surface radiation models," *Solar Energy,* vol. 45, 1990.

[40] R. Perez, P. Ineichen, R. Seals, J. Michalsky, and R. Stewart, "Modeling daylight availability and irradiance components from direct and global irradiance," *Solar Energy,* vol. 44, 1990.

[41] R. Perez, R. Seals, P. Ineichen, R. Stewart, and D. Menicucci, "A new simplified version of the perez diffuse irradiance model for tilted surfaces," *Solar Energy,* vol. 39, pp. 221-231, 1987.

[42] R. Perez, R. Stewart, C. Arbogast, R. Seals, and J. Scott, "An anisotropic hourly diffuse radiation model for sloping surfaces: Description, performance validation, site dependency evaluation," *Solar Energy,* vol. 36, pp. 481-497, 1986.

[43] V. Commission Internationale De L'Eclairage, "CIE Standard S011/E: Spatial Distribution of Daylight-CIE Standard General Sky," ed, 2003.

[44] R. Kittler, S. Darula, and R. Perez. (1998). *A set of standard skies*. Available: http://www.ustarch.sav.sk/ustarch/download/A_set_of_standard_skies.pdf

[45] E. Vezifeh, M. Schuß, and A. Mahdavi, "AN EMPIRICALLY-BASED ASSESSMENT OF COMPUTATIONAL SKY LUMINANCE DISTRIBUTION MODELS."

[46] C. Tsiopoulou, "Calibrated Sky Luminance Maps for Daylight Simulation," Master of Science, Department of Building Physics and Building Ecology, Vienna University of Technology, Vienna, 2006.

[47] B. Pinty, A. Lattanzio, J. V. Martonchik, M. M. Verstraete, N. Gobron, M. Taberner, *et al.*, "Coupling diffuse sky radiation and surface albedo.(Author Abstract)," *Journal of the Atmospheric Sciences*, vol. 62, p. 2580, 2005.

[48] F. E. Nicodemus, "Directional Reflectance and Emissivity of an Opaque Surface," *Applied Optics,* vol. 4, pp. 767-775, 1965/07/01 1965.

[49] X. D. He, K. E. Torrance, Fran, #231, o. X. Sillion, and D. P. Greenberg, "A comprehensive physical model for light reflection," presented at the Proceedings of the 18th annual conference on Computer graphics and interactive techniques, 1991.

[50] K. Plachta, "Algorithm applying a modified BRDF function in Λ-ridge concentrator of solar radiation," 2015, pp. 95160X-95160X-10.

[51] W. L. Wolfe, *Introduction to radiometry*. Bellingham, Wash. (1000 20th St. Bellingham WA 98225-6705 USA): Bellingham, Wash. SPIE, 1998.

[52] P. Ineichen, O. Guisan, and R. Perez, "Ground-reflected radiation and albedo," *Solar Energy,* vol. 44, 1990.

[53] C. Demain, M. Journee, and C. Bertrand, "Evaluation of different models to estimate the global solar radiation on inclined surfaces," *Renewable Energy,* vol. 50, pp. 710-721, 2013.

[54] P. Ineichen, R. Perez, and R. Seals, "The importance of correct albedo determination for adequately modeling energy received by tilted surfaces," *Solar Energy,* vol. 39, pp. 301-305, 1987.

[55] K. Stamnes, B. Hamre, J. J. Stamnes, G. Ryzhikov, M. Biryulina, R. Mahoney, *et al.*, "Modeling of radiation transport in coupled atmosphere-snow-ice-ocean systems," *Journal of Quantitative Spectroscopy and Radiative Transfer,* vol. 112, pp. 714-726, 2011.

[56] H. Larsson, O. Steinvall, T. Chevalier, F. Gustafsson, Å. Persson, and P. Andersson, "Characterizing laser radar snow reflection for the wavelengths 0.9 and 1.5 μm," vol. 5791, ed, 2005, pp. 293-307.

[57] G. Picard, L. Arnaud, F. Domine, and M. Fily, "Determining snow specific surface area from near-infrared reflectance measurements: Numerical study of the influence of grain shape," *Cold Regions Science and Technology,* vol. 56, pp. 10-17, 2009.

[58] J. Veverka, "The photometric properties of natural snow and of snow-covered planets," *Icarus,* vol. 20, pp. 304-310, 1973.

[59] F. D. Eaton and I. Dirmhirn, "Reflected irradiance indicatrices of natural surfaces and their effect on albedo," *Applied optics,* vol. 18, p. 994, 1979.

[60] V. R. Taylor and L. L. Stowe, "Reflectance characteristics of uniform Earth and cloud surfaces derived from NIMBUS-7 ERB," *Journal of Geophysical Research: Atmospheres,* vol. 89, pp. 4987-4996, 1984.

[61] R. E. Dickinson, "Land Surface Processes and Climate—Surface Albedos and Energy Balance," *Advances in Geophysics*, vol. 25, pp. 305-353, 1983.

[62] D. S. Kimes and P. J. Sellers, "Inferring hemispherical reflectance of the earth's surface for global energy budgets from remotely sensed nadir or directional radiance values," *Remote Sensing of Environment*, vol. 18, pp. 205-223, 1985.

[63] C. A. Gueymard, "Direct and indirect uncertainties in the prediction of tilted irradiance for solar engineering applications," *Solar Energy*, vol. 83, pp. 432-444, 2009.

[64] B. Choudhury, "A note on the solar elevation dependence of clear-sky snow albedo," *Cold Regions Science and Technology*, vol. 5, pp. 173-176, 1981.

[65] T. H. Painter and J. Dozier, "The effect of anisotropic reflectance on imaging spectroscopy of snow properties," *Remote Sensing of Environment*, vol. 89, pp. 409-422, 2/29/ 2004.

[66] B. E. Psiloglou and H. D. Kambezidis, "Estimation of the ground albedo for the Athens area, Greece," *Journal of Atmospheric and Solar-Terrestrial Physics*, vol. 71, pp. 943-954, 2009.

[67] T. Muneer, *Solar Radiation and Daylight Models*. Burlington: Burlington Butterworth-Heinemann, 2004.

[68] J. Johnson, D. Yoon, and Y. Baghzouz, "Modeling and analysis of a bifacial grid-connected photovoltaic system," ed, 2012, pp. 1-6.

[69] Wikipedia. (2015, 19 November 2015). *Albedo*. Available: https://en.wikipedia.org/w/index.php?title=Albedo&oldid=690501723

[70] SUNPREME Thin Film HCT Bi-facial PV cells datasheet [Online]. Available: http://www.sunpreme.com/wp-content/uploads/2015/07/Sunpreme-Datasheet-GxB-360W-Bifacial-Module-Rev-1-3.pdf

[71] Sunpreme, "Thin Film HCT Bi-facial PV cells," Sunpreme, Ed., ed.

[72] J. Nelson, *The physics of solar cells*. London: London : Imperial College Press, c2003., 2003.

[73] A. Gabr, "Title," unpublished|.

[74] R. G. Ross, "Flat-Plate Photovoltaic Array Design Optimization," in *14th IEEE Photovoltaic Specialists Conference*, ed. San Diego, CA, 1980.

[75] M. C. Alonso García and J. L. Balenzategui, "Estimation of photovoltaic module yearly temperature and performance based on Nominal Operation Cell Temperature calculations," *Renewable Energy*, vol. 29, pp. 1997-2010, 2004.

[76] O. Breitenstein, "Understanding the current-voltage characteristics of industrial crystalline silicon solar cells by considering inhomogeneous current distributions," *Opto-Electronics Review*, vol. 21, pp. 259-282, 2013.

[77] J. Haysom, "Simple PV and CPV production calculator for using with TMY format data," in *Simple PV and CPV production calculator for using with TMY format data*, ed. Ottawa, Ontario, Canada.: Sunlab solar energy research group, University of Ottawa, 2015.

[78] A. Gharakhani Siraki and P. Pillay, "Study of optimum tilt angles for solar panels in different latitudes for urban applications," *Solar Energy,* vol. 86, pp. 1920-1928, 2012.

[79] H. Darhmaoui and D. Lahjouji, "Latitude Based Model for Tilt Angle Optimization for Solar Collectors in the Mediterranean Region," *Energy Procedia,* vol. 42, pp. 426-435, 2013.

[80] J. P. Singh, T. M. Walsh, and A. G. Aberle, "Performance investigation of bifacial PV modules in the tropics," in *Proceedings of the 27th European Photovoltaic Solar Conference and Exhibition*, 2012, pp. 3263-3266.

[81] H. K. Hajjar, F. A. Dubaikel, and I. M. Ballard, "Bifacial photovoltaic technology for the oil and gas industry," in *2015 Saudi Arabia Smart Grid (SASG)*, 2015, pp. 1-4.

[82] T. Joge, Y. Eguchi, Y. Imazu, I. Araki, T. Uematsu, and K. Matsukuma, "Basic application technologies of bifacial photovoltaic solar modules," *Electrical Engineering in Japan,* vol. 149, pp. 32-42, 2004.

[83] V. Tatsiankou, K. Hinzer, J. Mohammed, A. Muron, M. Wilkins, J. Haysom, *et al.*, "Reconstruction of solar spectral resource using limited spectral sampling for concentrating photovoltaic systems," vol. 891506, pp. 1–11, 2013.